

# Matching of repeat remote sensing images for precise analysis of mass movements

Misganu Debella-Gilo



Dissertation submitted for the degree of  
*Philosophiae Doctor* (PhD)

Department of Geosciences  
Faculty of Mathematics and Natural Sciences

University of Oslo

Oslo, Norway 2011

© Misganu Debella-Gilo, 2011

*Series of dissertations submitted to the  
Faculty of Mathematics and Natural Sciences, University of Oslo  
No. 1152*

ISSN 1501-7710

All rights reserved. No part of this publication may be reproduced or transmitted, in any form or by any means, without permission.

Cover: Inger Sandved Anfinsen.  
Printed in Norway: AIT Oslo AS.

Produced in co-operation with Unipub.  
The thesis is produced by Unipub merely in connection with the thesis defence. Kindly direct all inquiries regarding the thesis to the copyright holder or the unit which grants the doctorate.

# Preface

This thesis is a compilation of research works conducted at the Department of Geosciences of the University of Oslo as a partial fulfillment of the requirements for the degree of Philosophiae Doctor (Ph.D.) during my employment at the Department as a research fellow. The research was conducted with the title “*Matching of repeat remote sensing images for precise analysis of mass movements*” under the umbrella of a larger research project titled “*Precise analysis of mass movements through correlation of repeat images (CORRIA)*”. It is a methodological study which focuses on the commonly used algorithms for matching of repeat remote sensing images in mass movement analysis, namely the normalized cross-correlation and the least squares matching. The study is thus not restricted to any geographic location, but high mountain regions in general. As such, the data used in the research are satellite and airborne images of mass movements from the European Alps with some image data from Svalbard and Asian high mountains. The mass movement types on which the methods and algorithms are tested, evaluated and modified are glacier flow, rockglacier creep and land sliding.

The research is funded by the Research Council of Norway (NFR) through the CORRIA project (no. 185906/V30) and contributes also to the NFR International Centre for Geohazards (SFF-ICG 146035/420) and the European Space Agency (ESA) GlobGlacier and glaciers\_CCI project. The results of the research are communicated through publications in scientific journals, and oral and poster presentations at international scientific conferences.

Misganu Debella-Gilo

December 2011

Oslo, Norway



## List of papers

**Paper I:** *Debella-Gilo, M. and A. Kääb (2011). "Sub-pixel precision image matching for measuring surface displacements on mass movements using normalized cross-correlation." Remote Sensing of Environment **115**(1): 130-142.*

**Paper II:** *Debella-Gilo, M. and A. Kääb (2011). "Locally adaptive template sizes for matching repeat images of Earth surface mass movements." ISPRS Journal of Photogrammetry and Remote Sensing **Revision submitted.***

**Paper III:** *Debella-Gilo, M. and A. Kääb (2011). "Measurement of surface displacement and deformation on mass movements using least squares matching of repeat images." Remote Sensing **Revision submitted.***

**Paper IV (peer-reviewed proceeding paper):** *Debella-Gilo, M. and A. Kääb (2011). Monitoring slow-moving landslides using spatially adaptive least squares image matching. The Second World Landslide Forum, Rome, Italy, Accepted.*



## Acknowledgements

Many people supported and inspired me throughout this thesis work. I am especially very grateful to my supervisor Dr. Andreas Max Kääh without whom I would not have been able to complete this study. Dr. Kääh inspired my interest in Geomatics and supervised me with great enthusiasm throughout the study. His office was always open for me for short and long discussions. Thanks Andi for creating such a lively and comfortable academic milieu. I would like to thank Dr. Bernd Etzelmüller for introducing me to the Department's core research interest and for encouraging me to pursue Ph.D. study when he was my M.Sc. supervisor. I am very grateful to the CORRIA project co-participant Torborg Heid for the frequent discussions we had. Dr. Christopher Nuth and my officemate Dr. Kimberly Ann Casey proofread some of the manuscripts. Thanks Chris and Kimberly for that. I would like to thank all the PhD students and staff of the Department for the inspirations and feedbacks during the remote sensing group seminars and the lunch seminars.

I attended two weeks summer school at the European Space Research Institute of the European Space Agency (ESA-ESRIN) based in Frascati near Rome, Italy. I am very grateful for the advanced lectures I attended. The organization of the summer school by Dr. Pierre Philip Mathieu is appreciated.

My earnest gratitude goes to my mother Tirunesh Cheqesse and my father Debella Gilo for keeping me in school during my early days where and when it was rather an exception than the norm to do so. The principles they instilled in me during those days will always stay with me. I would like to thank my brothers and sisters for their support over the years. I am very grateful to my soulmate Hawi Aba Gisa. The joys and comforts I got since I met you have been the sources of my daily motivation. Thanks for your support and patience.

Last but not least, I would like to thank all my friends who unplugged me from academic stress and made me relax once in a while. Nobody is mentioned, but nobody is forgotten!

Thanks a lot!

Tusen takk!

Galatoomaa!





## Abstract

Photogrammetry, together with radar interferometry, is the most popular of the remote sensing techniques used to monitor stability of high mountain slopes. By using two images of an area taken from different view angles, photogrammetry produces digital terrain models (DTM) and orthorectified images. Repeat digital terrain models (DTM) are differenced to compute elevation changes. Repeat orthoimages are matched to compute the horizontal displacement and deformation of the masses. The success of the photogrammetric approach in the computation of horizontal displacement (and also the generation of DTM through parallax matching, although not covered in this work) greatly relies on the success of image matching techniques.

The area-based image matching technique with the normalized cross-correlation (NCC) as its similarity measure is widely used in mass movement analysis. This method has some limitations that reduce its precision and reliability compared to its theoretical potential. The precision with which the matching position is located is limited to the pixel size unless some sub-pixel precision procedures are applied. The NCC is only reliable in cases where there is no significant deformation except shift in position. Identification of a matching entity that contains optimum signal-to-noise ratio (SNR) and minimum geometric distortion at each location has always been challenging. Deformation parameters such as strains can only be computed from the inter-template displacement gradient in a post-matching process.

To find appropriate solutions for the mentioned limitations, the following investigations were made on three different types of mass movements; namely, glacier flow, rockglacier creep and land sliding. The effects of ground pixel size on the accuracy of the computed mass movement parameters such as displacement were investigated. Different sub-pixel precision algorithms were implemented and evaluated to identify the most precise and reliable algorithm. In one approach images are interpolated to higher spatial resolution *prior* to matching. In another approach the NCC correlation surface is interpolated to higher resolution so that the location of the correlation peak is more precise. In yet another approach the position of the NCC peak is computed by fitting 2D Gaussian and parabolic curves to the correlation peak turn by turn. The results show that the mean error in metric unit increases linearly with the ground pixel size being about half a pixel at each resolution. The proportion of undetected moving masses increases with ground pixel size depending on the displacement magnitudes. Proportion of mismatching templates increases with increasing ground pixel size depending on the noise content, i.e. temporal difference, of the image pairs. Of the sub-pixel precision algorithms, interpolating the image to higher resolution using bi-cubic convolution *prior* to matching performs best. For example, by increasing the spatial resolution (i.e. reducing the ground pixel size) of the matched images by 2 to 16 times using intensity interpolation, 40% to 80% of the performances of the same resolution original image can be achieved.

A new spatially adaptive algorithm that defines the template sizes by optimizing the SNR, minimizing the geometric distortion and optimizing the similarity measure was also devised, implemented and evaluated on aerial and satellite images of mass movements. The algorithm can also exclude ambiguous and occluded entities from the matching. The evaluation of the algorithm was conducted on simulated deformation images and in relation to the image-wide fixed template sizes ranging from 11 to 101 pixels. The evaluation of the algorithm on the real mass movements is conducted by a novel technique of reconstructing the reference image from the deformed image and computing the global correlation coefficient and the corresponding SNR between the reference and the reconstructed image. The results show that the algorithm could reduce the error of displacement estimation by up to over 90% (in the simulated case) and improve the SNR of the matching by up to over 4 times compared to the globally fixed template sizes. The algorithm pushes terrain displacement measurement from repeat images one step forward towards full automation.

The least squares image matching (LSM) matches images precisely by modeling both the geometric and radiometric deformation. The potential of the LSM is not fully utilized for mass movement analysis. Here, the procedures with which horizontal surface displacement, rotation and strain rates of glacier flow, rockglacier creep and land sliding are computed from the spatial transformation parameters of LSM automatically during the matching are implemented and evaluated. The results show that the approach computes longitudinal strain rates, transverse strain rates and shear strain rates reliably with mean absolute deviation in the order of  $10^{-4}$  as evaluated on stable grounds. The LSM also improves the accuracy of displacement estimation of the NCC by about 90% in ideal (simulated) case and the SNR of the matching by about 25% in real multi-temporal images of mass movements.

Additionally, advanced spatial transformation models such as projective and second degree polynomial are used for the first time for mass movement analysis in addition to the affine. They are also adapted spatially based on the minimization of the sum of square deviation between the matching templates. The spatially adaptive approach produces the best matching, closely followed by the second-order polynomial. Affine and projective models show similar results closely following the two approaches. In the case of the spatially adaptive approach, over 60% of the entities matched for the rockglacier and the landslide are best fit by the second-order polynomial model.

In general, the NCC alone may be sufficient for low resolution images of moving masses with limited or no deformation. To gain better precision and reliability in such cases, the template sizes can be adapted spatially and the images can be interpolated to higher resolution (preferably not more detail than  $1/16^{\text{th}}$  of a pixel) *prior* to the matching. For highly deformed masses where higher resolution images are used, the LSM is recommended as it results in more accurate matching and deformation parameters. Improved accuracy and precision are obtained by selecting matchable areas using the spatially adaptive algorithm, identifying approximate matches using the NCC and optimizing the matches and measuring the deformation parameters using the LSM algorithm.

# Contents

PREFACE.....	III
LIST OF PAPERS .....	V
ACKNOWLEDGEMENTS.....	VII
ABSTRACT.....	IX
CONTENTS.....	XI
PART I OVERVIEW.....	XV
1. INTRODUCTION.....	1
1.1. MOTIVATION.....	1
1.2. OBJECTIVES.....	2
1.3. OUTLINE.....	4
2. MASS MOVEMENT ANALYSIS AND MONITORING .....	5
2.1. MASS MOVEMENTS IN HIGH MOUNTAIN REGIONS .....	5
2.2. METHODS OF MASS MOVEMENT ANALYSIS AND MONITORING.....	8
3. REMOTE SENSING METHODS OF MASS MOVEMENT ANALYSIS .....	11
3.1. PHOTOGRAMMETRY .....	11
3.2. INTERFEROMETRIC SYNTHETIC APERTURE RADAR (INSAR).....	13
3.3. LASER ALTIMETRY .....	15
3.4. COMPARISON OF THE DIFFERENT REMOTE SENSING TECHNIQUES.....	15
4. IMAGE MATCHING IN MASS MOVEMENT ANALYSIS .....	17
4.1. IMAGE MATCHING DEFINITION AND PURPOSES .....	17
4.2. IMAGE MATCHING ELEMENTS AND METHODS .....	17
4.3. STATE-OF-THE-ART AREA-BASED IMAGE MATCHING FOR MASS MOVEMENT ANALYSIS.....	19
4.3.1. Imagery.....	21
4.3.2. Preprocessing .....	23
4.3.3. Identification of matching entities .....	24
4.3.4. Defining search area .....	25
4.3.5. Similarity measures .....	25
4.3.6. Optimization and post-processing .....	27
4.3.7. Computation of mass movement parameters.....	28
4.3.8. Uncertainties .....	29
4.3.9. Evaluation techniques.....	31
5. CONCEPTUAL FRAMEWORK.....	33

<b>6. SUMMARY OF PAPERS AND OTHER INNOVATIONS .....</b>	<b>35</b>
<b>6.1. GROUND PIXEL SIZE EFFECTS AND SUB-PIXEL ALGORITHMS IN NCC (PAPER I).....</b>	<b>35</b>
<b>6.2. LOCALLY ADAPTIVE OPTIMUM TEMPLATE SIZES FOR THE NCC ALGORITHM (PAPER II) .....</b>	<b>36</b>
<b>6.3. LSM FOR DISPLACEMENT AND DEFORMATION MEASUREMENT (PAPER III).....</b>	<b>37</b>
<b>6.4. SPATIALLY ADAPTIVE AND HIGHER-ORDER TRANSFORMATION MODELS IN LSM (PAPER IV) .....</b>	<b>38</b>
<b>6.5. OTHER INNOVATIONS OF THE THESIS .....</b>	<b>39</b>
<b>7. CONCLUSIONS AND OUTLOOK .....</b>	<b>45</b>
<b>8. REFERENCES.....</b>	<b>49</b>
<b>PART II JOURNAL PUBLICATIONS .....</b>	<b>57</b>
<b>I. SUB-PIXEL PRECISION IMAGE MATCHING FOR MEASURING SURFACE DISPLACEMENTS ON MASS MOVEMENTS USING NORMALIZED CROSS-CORRELATION .....</b>	<b>59</b>
<b>I.1. INTRODUCTION.....</b>	<b>60</b>
<b>I.2. METHODS .....</b>	<b>62</b>
1.2.1. <i>Image data and resolution pyramid .....</i>	<i>62</i>
1.2.2. <i>Normalized cross-correlation.....</i>	<i>64</i>
1.2.3. <i>Matching and displacement measurement at different pixel sizes.....</i>	<i>66</i>
1.2.3. <i>The sub-pixel precision approaches.....</i>	<i>68</i>
1.2.4. <i>Evaluation of different levels of sub-pixel detail.....</i>	<i>70</i>
<b>I.3. TEST SITES.....</b>	<b>72</b>
<b>I.4. RESULTS .....</b>	<b>73</b>
1.4.1. <i>Displacement vectors of the three different mass movements .....</i>	<i>73</i>
1.4.2. <i>Pixel resolution and matching accuracy.....</i>	<i>75</i>
1.4.4. <i>Accuracies of the sub-pixel precision algorithms.....</i>	<i>78</i>
1.4.5. <i>Relative performance of the algorithms at different sub-pixel details.....</i>	<i>81</i>
<b>I.5. DISCUSSION .....</b>	<b>84</b>
1.5.1. <i>Image resolution issues .....</i>	<i>84</i>
1.5.2. <i>Performance of the sub-pixel algorithms and levels of detail .....</i>	<i>85</i>
1.5.3. <i>Velocity fields.....</i>	<i>87</i>
<b>I.6. CONCLUSIONS AND OUTLOOK.....</b>	<b>89</b>
<b>I.7. REFERENCES .....</b>	<b>90</b>
<b>II. LOCALLY ADAPTIVE TEMPLATE SIZES FOR MATCHING REPEAT IMAGES OF EARTH SURFACE MASS MOVEMENTS .....</b>	<b>97</b>
<b>II.1. INTRODUCTION.....</b>	<b>97</b>
<b>II.2. TEMPLATE SIZE IN IMAGE MATCHING.....</b>	<b>100</b>
II.2.1. <i>Template size and signal-to-noise ratio .....</i>	<i>101</i>
II.2.2. <i>Template size and cross-correlation coefficient.....</i>	<i>107</i>
II.2.3. <i>Signal-to-noise ratio and cross-correlation coefficient.....</i>	<i>110</i>
<b>II.3. METHODS .....</b>	<b>111</b>
II.3.1. <i>Algorithm for locally adaptive template sizes .....</i>	<i>111</i>
II.3.2. <i>Test and implementation of the algorithm.....</i>	<i>114</i>
II.3.3. <i>Performance evaluation of the algorithm.....</i>	<i>118</i>
<b>II.4. RESULTS .....</b>	<b>120</b>
II.4.1. <i>Performance of the algorithm on the test images.....</i>	<i>120</i>
II.4.3. <i>Performance of the algorithms on the multi-temporal images.....</i>	<i>126</i>
II.4.4. <i>Relative advantage of the adaptive algorithm over globally fixed template sizes .....</i>	<i>132</i>
<b>II.5. GENERAL DISCUSSION.....</b>	<b>133</b>
<b>II.6. CONCLUSIONS AND OUTLOOK.....</b>	<b>136</b>
<b>II.7. REFERENCES .....</b>	<b>137</b>

<b>III. MEASUREMENT OF SURFACE DISPLACEMENT AND DEFORMATION ON MASS MOVEMENTS USING LEAST SQUARES MATCHING OF REPEAT IMAGES .....</b>	<b>141</b>
<b>III.1. INTRODUCTION.....</b>	<b>141</b>
<b>III.2. THE LEAST SQUARES MATCHING ALGORITHM AND ITS SIGNIFICANCE IN MASS MOVEMENT ANALYSIS.....</b>	<b>143</b>
<i>III.2.1. The least squares matching algorithm.....</i>	<i>143</i>
<i>III.2.2. The least squares matching in mass movement analysis .....</i>	<i>144</i>
<b>III.3. METHODS .....</b>	<b>147</b>
<i>III.3.1. Image datasets .....</i>	<i>147</i>
<i>III.3.2. Image matching .....</i>	<i>149</i>
<i>III.3.3. Computation of displacement and deformation.....</i>	<i>149</i>
<i>III.3.3.1. Horizontal surface displacement .....</i>	<i>149</i>
<i>III.3.4. Performance evaluation .....</i>	<i>150</i>
<b>III.4. RESULTS .....</b>	<b>151</b>
<i>III.4.1. Horizontal surface displacements .....</i>	<i>151</i>
<i>III.4.2. Precision and validity of the displacement data.....</i>	<i>153</i>
<i>III.4.3. Surface strain and rotation rates.....</i>	<i>155</i>
<i>III.4.4. Precision and validity of the deformation data .....</i>	<i>160</i>
<b>III.5. DISCUSSION .....</b>	<b>161</b>
<i>III.5.1. Computed displacements and deformations .....</i>	<i>161</i>
<i>III.5.2. On the precision of the algorithm and sources of error .....</i>	<i>162</i>
<b>III.6. CONCLUSIONS AND OUTLOOK.....</b>	<b>163</b>
<b>III.7. REFERENCES .....</b>	<b>165</b>
<b>IV. MONITORING SLOW-MOVING LANDSLIDES USING SPATIALLY ADAPTIVE LEAST SQUARES IMAGE MATCHING .....</b>	<b>169</b>
<b>IV.1. INTRODUCTION.....</b>	<b>169</b>
<b>IV.2. THE LEAST SQUARES MATCHING IN MASS MOVEMENT ANALYSIS .....</b>	<b>171</b>
<b>IV.3. METHODS .....</b>	<b>173</b>
<i>IV.3.1. Image datasets .....</i>	<i>173</i>
<i>IV.3.2. Image matching .....</i>	<i>174</i>
<i>IV.3.3. Computation of displacement .....</i>	<i>175</i>
<i>IV.3.4. Evaluation .....</i>	<i>176</i>
<b>IV.4. RESULTS .....</b>	<b>176</b>
<i>IV.4.1. Rockglacier creep.....</i>	<i>176</i>
<i>IV.4.2. Landslide .....</i>	<i>177</i>
<b>IV.5. DISCUSSION .....</b>	<b>178</b>
<b>IV.6. CONCLUSIONS AND OUTLOOK.....</b>	<b>179</b>
<b>IV.7. REFERENCES .....</b>	<b>180</b>
<b>APPENDIX.....</b>	<b>183</b>
<b>PUBLICATIONS OF M. DEBELLA-GILO .....</b>	<b>183</b>



# **PART I OVERVIEW**





# 1. Introduction

## 1.1. Motivation

Geohazards related to mass movements cause human casualties, infrastructure destructions, environmental degradation and changes to the landscape. Hazardous events such as landslides, rock avalanches, ice avalanches, rockfalls, etc can provoke other hazardous chain-reactions such as damming of rivers, outbursting of lakes, and tsunamis, all resulting in great economic, humanitarian and environmental consequences (Evans and Clague, 1994; Kääb et al., 2005a; Kääb et al., 2005b). Glacier and permafrost related hazards alone can take hundreds, even thousands, of human lives at once and can cause a global economic damage on the order of hundreds of millions of Euros (Kääb et al., 2005b). The risk is even increasing due to the expansion of human activities to hazard-prone areas driven by economic and population growth. Mass movements often occur in high mountain regions which are particularly sensitive to climate change and thus represent unique areas for the detection of climatic change impacts (Beniston, 2003; Kääb et al., 2005b). Therefore, monitoring high mountain terrain is an important step for understanding climate change impacts and improving hazard management.

High mountain regions are difficult to access physically due to remoteness and relatively hazardous terrains. The analysis and monitoring of mass movements in these regions therefore greatly benefit from remote sensing methods that provide spatially continuous and temporally frequent data from a distance (Kääb et al., 2005a). The available collection of remote sensing data over more than six decades in many countries coupled with the advances in the technologies of image acquisition indicate a largely untapped potential of using bi- and multi-temporal images for understanding past histories, monitoring current processes and predicting future trends of high mountain slopes. However, the advancement in the technologies of image acquisition and the speed with which image data are accumulated has not been fully complemented with advanced techniques of processing and analysis.

A remote sensing technique that has become increasingly popular in analyzing and monitoring Earth surface mass movements is matching of repeat images. Two and three dimensional displacements of glacier flow, rockglacier creep, landslides, etc can be computed by matching repeat remotely sensed optical images (Bindschadler and Scambos, 1991;

Copland et al., 2009; Delacourt et al., 2004; Haug et al., 2010; Janke, 2005; Kaufmann and Ladstädter, 2003; Kääb, 2002; Kääb and Vollmer, 2000; Maas et al., 2010; Wangenstein et al., 2006; Yamaguchi et al., 2003). Change in elevation can be measured using a technique of differencing elevations measured at different times (Abdalati et al., 2001; Dewitte et al., 2008; Kääb, 2005b; Kääb et al., 1997; Kääb et al., 2005a; Moholdt et al., 2010; Nuth and Kääb, 2011; Wangenstein et al., 2006). Both the photogrammetric computation of the horizontal displacements and the generation of the DEM, if done through stereo parallax measurements, are highly dependent on image matching techniques, especially image correlation.

Many of the image matching algorithms are developed in other fields and for other purposes than mass movement analysis where the temporal baselines and the geometric characteristics are different from that of mass movement images. Limitations of precision, reliability and automation issues hamper the method in mass movement applications calling for further researches aimed at:

- (1) Evaluation and identification of the factors limiting precision and reliability in the most commonly used image matching algorithms,
- (2) Modification (where necessary) of the image matching algorithms for improving the precision and reliability of the derived mass movement parameters,
- (3) Test and evaluation of the algorithms on different mass movement types for robustness,
- (4) Increasing the number of mass movement parameters to be computed directly by the image matching algorithms,
- (5) Adaptation of the algorithms to the local mass movement and image characteristics, and
- (6) More automation with reduced manual interference of the image matching task.

## **1.2. Objectives**

Image correlation techniques, especially the normalized cross-correlation (NCC) algorithm, are widely used in matching of multi-temporal mass movement images. The precision of the NCC is limited to a pixel, which translates to large ground size particularly in low resolution images. The effects of the pixel-precision on the accuracy of the computed mass movement parameters have not been well quantified. Besides, the sub-pixel precision algorithms used have not been systematically evaluated in mass movement images. Some of the objectives of the thesis are therefore to:

- *investigate the influence of pixel size on the detectability and precision of horizontal displacement of mass movements*
- *identify the most precise and reliable sub-pixel image matching algorithms when using the NCC*

The NCC and other area-based image matching algorithms require that the entities to be matched have adequate texture with minimum noise and geometric distortion (Schenk, 1999). Small matching entities lack the demanded texture for the matching while large matching entities may involve significant deformation. Compromising between the two gets more challenging in matching repeat mass movement images as they have high noise level and deformation, which varies spatially, due to temporal differences. Another specific aim of the thesis was thus to:

- *develop a spatially adaptive technique for identifying matchable entities, optimizing their sizes and excluding ambiguous and occluded entities*

The least squares image matching (LSM) algorithm is designed to deal with the limitations of the NCC such as precision and the influence of geometric and radiometric distortions (Förstner, 1982). LSM operates in such a way that the geometric and radiometric distortions between the matching entities are adjusted so that the sum of squares of their intensity differences is minimized. There is very limited application and evaluation of the algorithm in mass movement analysis. Besides, further advantage of the capability of the algorithm to model the geometric distortion is not taken. Only the affine transformation model has been used in the few applications of LSM for mass movement analysis (Kaufmann and Ladstädter, 2003; Maas et al., 2010; Whillans and Tseng, 1995). The deformation may however involve convergence/divergence, tilting and curving of the masses demanding more advanced transformation models such as the full projective and the second-order polynomial (quadratic) models. The mode of the deformation may even vary spatially. Some of the specific objectives of this thesis were therefore to:

- *implement and evaluate the LSM for computation of horizontal surface displacement in glacier flow, rockglacier creep and land sliding*
- *develop, implement and test the procedures with which the mass movement deformation parameters, such as rotation and strain rates, are computed from the geometric transformation parameters of the LSM model used simultaneous with the image matching task*

- *implement and evaluate advanced spatial transformation models such as the projective and second-order polynomial in displacement measurement of mass movements*
- *spatially adapt the geometric transformation models of the LSM to the local deformation of the mass movements*

### **1.3. Outline**

The thesis is divided into two major parts. Part I presents an overview of the research theme. This part is divided into six chapters. Chapter one formulates the motivation behind the research followed by the objectives. Chapter two defines and explains types of mass movements common in high mountain regions. Available methods of mass movement analysis and monitoring, remote sensing included, are discussed. Chapter three briefly discusses the different remote sensing technologies used in mass movement analysis and monitoring. Chapter four then provides state-of-the-art area-based spatial-domain image matching for mass movement analysis and monitoring, starting from image acquisition to accuracy evaluation. The conceptual framework of the research is explored in chapter five specifying the research theme, image data, processing tools and outputs of the research. Chapter six briefly summarizes each of the papers published or submitted for publication followed by other key innovations of the research that played, however, not central part in the publications. Part II of the thesis presents four research papers: three journal articles and one peer-reviewed proceeding paper. The papers are numbered I to IV and are referred to in the thesis using those numbers.

## **2. Mass movement analysis and monitoring**

### **2.1. Mass movements in high mountain regions**

Mass movement, in the context of this thesis, refers to the down slope movement of Earth materials (Ritter, 2006), including rocks, glacier ice and debris. Such movements can lead to sudden or gradual failure of the slope. Slope masses move when the stress exerted on them is greater than their strengths. The major source of the stress is gravitational force occasionally aided by tectonic forces. The strength of the materials is weakened by agents such as heat, water, anthropogenic activities and tectonic actions.

High mountain areas have high gravity-based potential energy of which hazard potential is enhanced by steep slopes. These areas are often characterized by low temperature and large accumulations of frozen water. Warming of cold environments increases therefore the potential for mass movements in two ways. First, warming increases wetness from melting surface or subsurface ice leading to increased pore water pressure. Second, the cohesive force that cements the materials in glaciers and rockglaciers, and also in joints of rock faces and slopes, is highly reduced due to the melting of ice and the freeze/thaw cycles. There is thus a great potential for mass movements in high mountain regions as compared to other parts of the globe. The hazard potentials can be enhanced by climate change as the temperature of surface and subsurface ice may increase (Beniston, 2003; Dehn et al., 2000; Gruber and Haeberli, 2007; Haeberli and Beniston, 1998).

Mass movement redistributes both material and energy controlling the effects of the dynamic factors such as climate change and its consequences such as the mass balance (Hooke, 2005; Kääb, 2005b; Kääb et al., 2005a). Typical mountain glaciers have accumulation zones at high altitude areas where snow accumulates, is buried and eventually crystallizes into solid ice after undergoing metamorphism (Hooke, 2005). The glacier then moves down slope towards lower elevation (ablation area) where the ice gets heated and melted ending up in a lake, river or sea. Under equilibrium condition, the ice lost in the ablation zone equals the ice deposited in the accumulation zone. Change in velocity of glaciers lead to changes in this equilibrium. Or, vice versa, changes in mass balance will lead to an adjustment of ice fluxes. Horizontal flow is thus one of the major components of glacier mass loss in addition to bottom melting, calving, sublimation, etc (Hooke, 2005; Sommerkorn and Hamilton, 2008).

The velocity differences over space (strain rates) are results of deviatoric stresses, which are differences in stress with space (Hooke, 2005). Glaciers deform down slope in response to gravitational stress, internal deformation of the ice crystals and basal slip due to heating of the base of the glacier, approximately obeying plastic mechanics (Hooke, 2005; Nye, 1952). Glacier velocity varies spatially, most notably decreasing horizontally from the glacier centre towards the glacier margins and vertically downwards to the glacier bottom. Fig. 2-1 presents the spatial variation of the horizontal surface velocity of Nigardsbreen glacier as a typical example. Difference in velocity with time (i.e. acceleration/deceleration) may be an impact of seasonal weather changes, climatic changes over longer period (Rignot and Kanagaratnam, 2006) and dynamic instabilities. These influence the temperature and hydraulic regime of the base changing the basal motion rather than the internal deformation of the ice crystals. Studies show that the spring/summer velocities are greater than the autumn/winter velocities (Willis, 1995).

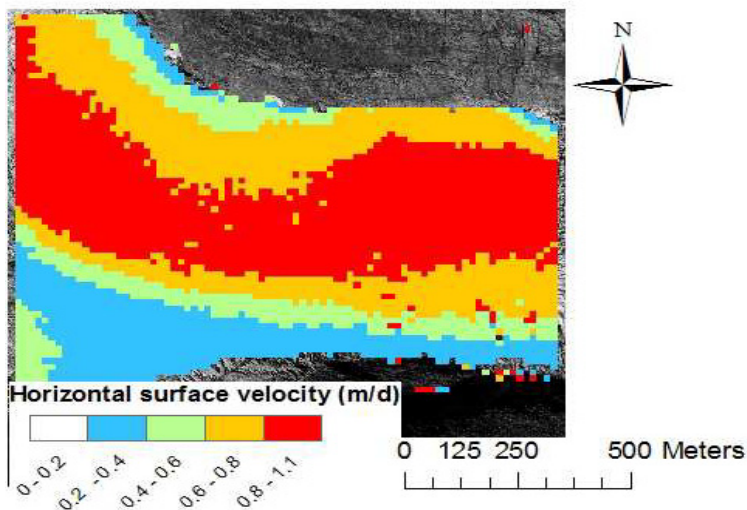


Fig. 2-1. Typical spatial variation of the horizontal surface velocity of glacier, an example from Nigardsbreen glacier, Southern Norway

When strain and basal sliding are large, the glacier may collapse, crevasse, debuttresse and calve, sometimes also creating glacial hazards. Such events may endanger life, economy, environment, and trigger chain-reactions such as lake outbursting and damming of rivers, resulting in far more disastrous consequences (Kääb et al., 2005a). Therefore, monitoring the velocity (strain rates and acceleration/deceleration) of glacier will help understand the impacts of the driving forces such as climate change and to foresee upcoming changes.

Rockglaciers are permanently frozen debris supersaturated with ice and ice lenses that slowly deform down slope under gravity (Barsch, 1992). Rockglaciers typically move slowly with speeds ranging from centimeters to decimeters per year forming a continuous and internally coherent flow field (Barsch, 1992; Haeberli et al., 2006; Kääb et al., 2003; Kääb and Reichmuth, 2005). Slope and material accumulation affect the spatial distribution of the velocity (Haeberli et al., 2006). The average velocity is typically high in the centre decreasing towards the margins. The velocities of tongue-like rockglaciers often depict velocity contours that emulate the shape of the rockglacier as shown by the example of the Muragl rockglacier (Fig. 2-2). Notice the high velocity region in the centre of the rockglacier. Little is known about the temporal variation of rockglacier creep. It is generally understood that causes of velocity variation varies depending on the temporal scale (Kääb, 2005b). The temporal variation of velocity is generally attributed to internal conditions of the rockglacier, weather and climate conditions, material supply, thermal regime and terrain topography (Kääb, 2005b; Kääb et al., 2003; Roer et al., 2005). Monitoring of surface deformation integrated with other subsurface techniques will help understand the three-dimensional deformation of rockglaciers. Understanding both spatial and temporal variation of the deformation is important for monitoring climate change impacts, geomorphologic processes and hazard potentials. The typically slow speed calls for very accurate measurements or longer time span between measurements.

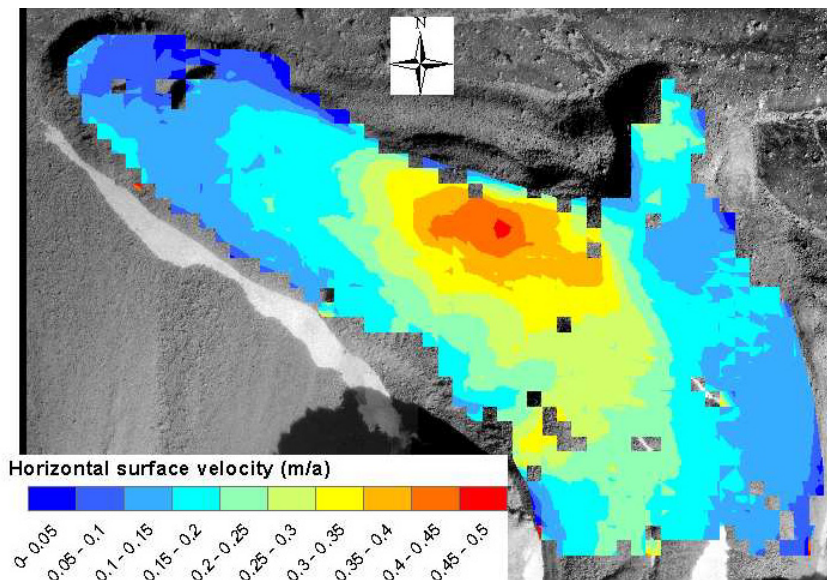


Fig. 2-2. Spatial variation of the horizontal surface velocity of rockglacier, an example from the Muragl rockglacier, Upper Engadine, Swiss Alps

Gravity, melting ice, tectonic activities, and loss of support due to, for example, glacier retreat generates land sliding, rockslides, rock falls, etc. These are common in high mountain environments. The loss of support due to the melting of valley glacier is found to be triggering rockslides in some parts of the European Alps (Kääb et al., 2000). Their velocity varies from a few centimeters per year to free fall of rock masses. In areas close to infrastructures and other human activities, they create risk and need thorough monitoring.

## **2.2. Methods of mass movement analysis and monitoring**

To understand climate change impacts and to foresee potential geohazards, mass movements have to be detected, analyzed and monitored. *Detection* is the observation that the slope mass is moving. *Analysis* in this case is the computation of different components of the movement. Slope masses, just like any other physical object, are characterized by their position and geometry in addition to their thematic properties. The changes in geometry and position are known as kinetics. Kinematics is then the quantification of the kinetic properties of the masses (Kääb, 2005b). Changes in position lead to displacement. Changes in displacement with space create deformation, i.e. changes in geometry (shape, size and orientation). Velocity is the displacement per unit time, and strain rate is change in velocity with space. The periodic computation of these parameters to observe the temporal behavior is known as *monitoring*.

The detection, analysis and monitoring can be carried out qualitatively, quantitatively, using numerical models, or in combination. As a rule, the more quantitative the method, the more communicable and valuable the information is. However, qualitative observation is also important especially in the detection of mass movements so that monitoring actions are taken. Qualitative methods include visual observation in the field using geomorphodynamic indicators, observation on photographs of different times, observation of indirect indicators such as tree trunks, etc (Kääb, 2005b; Shroder, 1978).

Numerical methods model the mass movements partly using data from the quantitative methods to understand mass movement process and forecast its future trends. The quantitative methods are basically involved in the detection, analysis and monitoring to measure the position, geometry and/or the kinetics of the slope masses. The approaches commonly used can be characterized into four groups. Each group has strengths and weakness when used for a given type of mass movement. They are in many cases complementary to each other rather than alternative. The four groups of quantitative methods are:



- **Geotechnical methods:** involve techniques of measuring relative displacement and deformation of masses without geo-referencing using instruments such as tiltometer (inclinometer), piezometer, extensometer, etc. Although they are known for measuring small magnitude displacement and deformation, they provide only point based data with limited spatial coverage. They have been used for monitoring deformation, for example, in glacial beds (Hart and Rose, 2001), rockglacier (Arenson et al., 2002) and landslides (Caris and Van Asch, 1991)

- **Geodetic methods:** involve the use of leveling instruments to quantify geo-referenced displacements of slope masses. Instruments such as levels, laser ranging, global navigation satellite system receivers, total stations, etc are used to regularly register the one, two and three dimensional positions of masses or points on masses. These result in very limited data density as they require point based measurements with instruments installed or placed at the measuring stations. They are used to monitor landslides, glacier flow and rockglacier creep (Andreassen et al., 2002; Kaufmann, 1996).

- **Geophysical methods:** involve the measurement of soil and debris parameters through systems such as ground penetrating radar (GPR), seismic survey and electrical resistivity measurement. They have been used for example in investigating landslides (Caris and Van Asch, 1991), glacier flow (Hart and Rose, 2001) and rockglacier deformations (Maurer and Hauck, 2007; Musil et al., 2002).

- **Remote sensing methods:** Remote sensing is the acquisition of information about an object or phenomenon, without making physical contact with the object (Lillesand et al., 2008). Basically the technique measures electromagnetic (EM) radiation emitted by the sun or by the measurement system itself that is reflected, scattered, diffracted or emitted by the object standing somewhere from meters to thousands of kilometers away. The remote sensing system does not need direct contact with the objects which is an indispensable characteristic for applications in remote and hazardous areas. It provides data usually in one, two or three dimensions regularly or on-demand covering large geographic area. The continuous improvements in the data quality and processing technique have made this method increasingly popular.



### **3. Remote sensing methods of mass movement analysis**

A remote sensing approach to mass movement analysis involves the thematic properties of objects such as reflection and scattering of EM radiation, together with the position and geometry of the platform (sensor) to unravel the position and geometric properties of the observed masses. The kinetics can then be computed directly or from repeat computation of the position and geometry. By using the kinetic properties together with models and/or auxiliary data, the dynamics of the slope masses can be understood. These are the bases for the use of remote sensing in monitoring and analysis of mass movements. As remote sensing is restricted mainly to the surface, the parameters measured are also restricted to the surface unless some inference techniques are used.

Depending on the type and the source of the EM radiation and the processing system used, the remote sensing technologies commonly used for mass movement analysis can be grouped into three: namely, photogrammetry, interferometric synthetic aperture radar (InSAR) and laser scanning. Brief explanation of each is given below followed by summary of their comparison.

#### **3.1. Photogrammetry**

Photogrammetry is the technique of measuring the position, orientation, shape and size of objects from images (Kraus, 2007). The images can be the conventional film-based photographs or, more recently, digital images acquired from the ground (terrestrial), air or space (satellite). Three branches of photogrammetry are known depending on the image type and processing technique. When the images are conventional (film-based) and the processing is optical-mechanical it is called analogue. When the images are conventional but the processing is based on computers, it is called analytical. When the images are digital (or digitized from analogue) and the processing is carried out by use of computers it is called digital photogrammetry, towards which modern photogrammetry is evolving.

The line of sight from the camera (sensor) location to any object on the ground can be constructed provided that the internal and external sensor parameters are known. The intersection of two homologous lines of sight in two images taken from different viewpoints (stereo images), as depicted in Fig. 3-1, can be used to determine the 3D location of objects

(Kraus, 2007; Kääb, 2005b; Mikhail et al., 2001; Schenk, 1999). By taking more points from the overlapping areas of the stereo images, a digital surface model (DSM) and orthoimages can be extracted. The identification of the homologous lines of sight can be conducted manually or digitally. In the digital approach the homologous points are identified through image matching techniques.

Photogrammetry provides the capability to monitor deformation in two major ways (Kaufmann and Ladstaedter, 2000; Kaufmann and Ladstädter, 2003; Kääb, 2005b). First, vertical changes can be monitored by subtracting the digital terrain models (DTM) of different times. Horizontal displacement can be computed from multi-temporal orthoimages through matching of features or image subsets and computing the change in position and geometry. Second, by using image pairs of different times, given accurate camera internal and external parameters, rough DTMs and ‘quasi-orthophotos’ can be generated and matched (Kaufmann and Ladstaedter, 2000). Positions of a feature in all orthophotos of the different times can be identified by matching. Once the positions are known lines of sight can be projected back from the positions to the images. The spatial intersection of the projection rays of the photographs of the same time gives the 3D position of the feature at the time. From the 3D positions of different times, the 3D displacement of the masses can be computed in the same process. The setup of the two approaches is depicted in Fig. 3-1 (Kääb, 2005b)

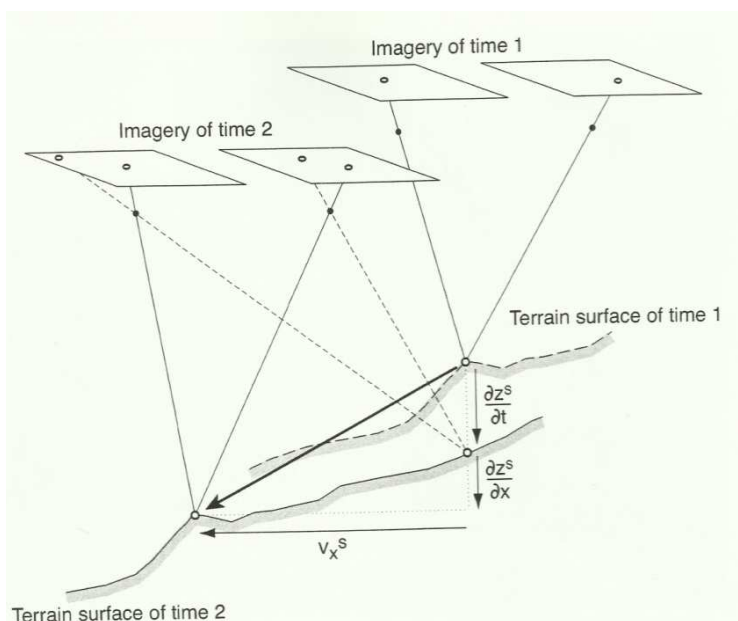


Fig. 3-1 The two basic approaches for the digital measurement of three-dimensional displacements from repeat optical images using photogrammetry, from (Kääb, 2005b), with

permission).  $v_x^s$  is the horizontal surface displacement;  $\delta z^s/\delta t$  is the elevation differences: whereas,  $\delta z^s/\delta x$  is the terrain slope component of the particle movement.

Image matching plays a double role in computer-based digital photogrammetry. First, image matching is used to create the DTM and the orthoimages of the different times, i.e. the geometry. Second, image matching is used to track the slope masses on the multi-temporal orthoimages, i.e. the kinematics. The success of digital photogrammetry in mass movement analysis is therefore heavily dependent upon the success of the image matching technique used.

Digital photogrammetry has widely been used to monitor two and three dimensional displacements of glaciers, rockglaciers and landslides (Casson et al., 2005; Casson et al., 2003; Delacourt et al., 2007; Kääb, 2002, 2005b; Kääb et al., 2005a; Strozzi et al., 2004; Yamaguchi et al., 2003). The change in elevation is measured by differencing digital elevation models measured at different times (Dewitte et al., 2008; Kääb, 2005b; Kääb et al., 1997; Kääb et al., 2005a). 3D surface flow vectors are also directly computed using the 'quasi-orthoimages' as stated above (Kaufmann and Ladstädter, 2003). Precision, reliability and robustness related to the image matching techniques partly limit photogrammetric applications in mass movement analysis.

### **3.2. Interferometric Synthetic Aperture Radar (InSAR)**

Interferometric analysis is based on the principle that the phase difference of the signals of two synthetic aperture radar (SAR) images acquired from slightly different orbit configurations (the same pass or different passes) can be exploited for the computation of terrain topography (Bamler and Hartl, 1998; Goldstein et al., 1988). The spatial variation of the phase difference of two coherent waves (interferogram) is proportional to the height difference and slant-range displacement. By removing the slant-range displacement due to horizontal interferometric baseline, i.e. interferogram flattening, the height dependent phase difference can be unwrapped to produce digital elevation model (DEM) of the area covered. If a temporal baseline is involved and there is coherence between the images of the two times, the flattened interferogram is proportional to both elevation and slant-range displacement. Subtraction of the height dependent phase difference, i.e. differential interferometry (DInSAR), results in the phase difference due to slant-range horizontal displacement alone.

Two approaches can then be used for mass movement analysis. First, by computing multi-temporal DTMs, elevation changes can be computed. The technique has been used on glacier, rockglacier and land subsidence in different cases (Catani et al., 2005b; Kääb, 2005a; Kääb et al., 2005a; Strozzi et al., 2004). Second, if there is horizontal ground displacement in the slant range direction, the multi-temporal interferogram contains both the altitude differences and horizontal displacement related components. The phase differences due to topography can be removed in different ways. (1) A synthetic interferogram based on the digital elevation model of the scene, if available, can be subtracted to produce the interferogram related to slant range displacement alone. (2) Interferograms of different times can be subtracted. This requires a pair of interferogram (at least three SAR images). (3) SAR images of no interferometric baseline but with temporal baseline will result in phase differences related only to slant range displacement (Klees and Massonnet, 1998). Provided coherence is maintained, as in non-vegetated areas, surface deformation of a few centimeters over the acquisition period can be measured. DInSAR measures displacement only in slant-range direction. Displacements in other directions are computed from DInSAR with slant ranges oriented in those directions. Nonetheless, DInSAR is a powerful technique for mapping land surface deformations (Bamler and Hartl, 1998; Catani et al., 2005a; Catani et al., 2005b; Hsing-Chung et al., 2004; Kenyi and Kaufman, 2003; Luckman et al., 2003; Strozzi et al., 2004; Strozzi et al., 2002).

An InSAR technology for mass movement analysis that can significantly reduce the problem of temporal decorrelation is the permanent scatterer InSAR (PSInSAR). PSInSAR overcomes the decorrelation problem by identifying resolution elements whose echo is dominated by a single scatterer in a series of interferograms (Ferretti et al., 2001; Hooper et al., 2007). Increased coherence over large horizontal and temporal baseline improves spatial resolution and precision. In its use of series of multi-temporal and multi-source SAR coherence data of a permanent scatterer, PSInSAR can monitor fine objects with very high precision as long as the coherence is established (Hilley et al., 2004; Lesniak and Porzycka, 2008; Meisina et al., 2006).

Yet another system of interferometry is the polarimetric interferometry which utilizes the polarimetric dependence of coherence to optimize the coherence between multi-temporal SAR images (Cloude and Papathanassiou, 1998). The optimization of the coherence contributes to the improvement of the precision of the computed deformation.

### **3.3. Laser altimetry**

Laser scanning, also known as LiDAR (Light Detection and Ranging), is a technique where laser light is sent to the ground in the form of pulses and the elapsed time between transmission and reception of the pulse is recorded (Wehr and Lohr, 1999). The record is then used to compute the distance between the sensor and the ground as the speed of light is constant and atmospheric influences are accounted for through modeling. Aided with global positioning system (GPS) and inertial navigation system (INS), it produces high accuracy 3D position of objects. The system is especially known for its high accuracy height measurement although its horizontal errors are known to be higher than that of the vertical. Terrestrial laser ranging has long been used in many forms. However, airborne laser scanning made the system more popular for terrain modeling. The launch of the ICESat satellite took the technique to space.

By taking multi-temporal measurements, the changes in elevation can be accurately measured if the errors in horizontal position are reduced. This is the major role of laser altimetry in mass movement analysis. In fact the ICESat satellite was launched to monitor the elevation changes of polar ice (Schutz et al., 2005). Laser altimetry methods have been used to monitor the elevation changes of rockglaciers, glaciers, rockslides, etc (Bauer et al., 2006; Bauer et al., 2003; Hofton and Blair, 2002; Krabill et al., 2002; Nuth and Kääb, 2011).

DTMs created using, especially airborne, laser scanning are usually very dense and accurate. Multi-temporal DTMs can then be treated just like multi-temporal orthoimages and image matching can be applied to track terrain features. Conventionally, signals of reflected or emitted EM radiation or their transforms are used in matching. DTM matching methods use another data domain, i.e. the elevation data. The approach has been used, for example, to measure velocities of ice (Abdalati and Krabill, 1999), rockglaciers (Bauer et al., 2003) and landslide deformation (Jones, 2006).

### **3.4. Comparison of the different remote sensing techniques**

The three remote sensing systems used in mass movement analysis and discussed above have a number of strengths and shortcomings. In most cases, they are complementary to each other; meaning, the weaknesses of one is covered by the others and vice versa. Summary of the strengths and limitations of each of the techniques is given in Table 3-1 (Baltsavias, 1999; Colesanti et al., 2003; Hsing-Chung et al., 2004; Lingua et al., 2008; Strozzi et al., 2004).

Photogrammetry has a long history in mass movement analysis starting from its early visual tracking of changes on photographs up to the current semi-automated computer processing. Due to this and its well-established implementation scheme, large volumes of application experience exist in mass movement analysis. It is indispensable in historical mass movement analysis as optical aerial and satellite images date back many decades, in contrast to SAR and laser scanning. Therefore, photogrammetry still remains central in deformation measurement, with still a lot of improvements required in the image matching algorithms used as they are critical in both geometric measurements and kinematics of the masses.

Table 3-1. Strengths and limitations of the three remote sensing techniques used in kinematic monitoring of mass movements

Technique	Strengths	Limitations
Photogrammetry	<ul style="list-style-type: none"> <li>• Well established technique and accumulated experience</li> <li>• Long records available for historic image data</li> <li>• Can be very accurate in both horizontal and vertical</li> <li>• Wide swath width covering large area</li> <li>• Includes optical information for interpretation of the object</li> </ul>	<ul style="list-style-type: none"> <li>• Dependent on illumination and atmospheric condition</li> <li>• Fails where there is no adequate signal contrast (texture)</li> </ul>
SAR interferometry	<ul style="list-style-type: none"> <li>• Independent of the presence of clouds and light</li> <li>• Good for areas lacking good texture for photogrammetry</li> <li>• Very accurate displacement measurement</li> </ul>	<ul style="list-style-type: none"> <li>• Displacement is only detected along the line of sight</li> <li>• Suffers from baseline decorrelation, volume decorrelation and temporal decorrelation in addition to the internal instrument-based noise</li> <li>• Poor spatial resolution</li> <li>• Hampered by layover and foreshortening effects in steep slope areas</li> <li>• Very high noise level due to radar speckle</li> </ul>
Laser altimetry	<ul style="list-style-type: none"> <li>• Very accurate in vertical direction</li> <li>• Can collect data in poor illumination (night) and light clouds</li> <li>• Good for areas lacking good texture in photogrammetry</li> <li>• Very dense data points can be obtained</li> </ul>	<ul style="list-style-type: none"> <li>• Horizontal displacement measurement requires very dense DSM</li> <li>• Lack of historical data</li> <li>• Still lack well-established processing schemes</li> </ul>



## 4. Image matching in mass movement analysis

### 4.1. Image matching definition and purposes

Image matching is a task of finding correspondence between two or more images taken at different times, from different viewpoints or by different sensors over the same area (Brown, 1992; Zitová and Flusser, 2003). Terms such as image registration, image fusion, image integration, image correlation, and feature tracking are often used for image matching inappropriately as they mix tasks and purposes. Image matching is a task carried out for purposes such as image registration (geometric alignment), fusion (thematic or spectral combination), tracking (change in position or geometry of a feature), etc. Image matching is used for one or more of these purposes in remote sensing, medical imaging, computer vision, robotics and mechanics among others. The analysis scheme can be grouped into four (Zitová and Flusser, 2003):

- **Multi-view analysis.** Images are taken from two or more directions so that larger 2D or 3D observations are made of a scene. This is common in remote sensing for image mosaicing or in computer vision and photogrammetric stereo vision. DTMs are basically generated using this scheme.
- **Multi-temporal analysis.** Images of the same scene are acquired at different times. The goal here is to find and evaluate the changes that have taken place within the temporal baseline of the images acquisitions. The task is part of change detection
- **Multi-modal analysis.** Images of the same scene are acquired by different sensors. The aim is to get more complex and detailed information about a scene by integrating or fusing data from different sensors.
- **Image-to-scene analysis.** Scene images are sometimes registered to models of the scene. Typical examples in remote sensing are registering DEM to image, map to image, etc.

### 4.2. Image matching elements and methods

A number of important elements are common to all image matching tasks independent of the application. Fig. 4-1 is a schematic depiction of an area-based image matching scheme with

most of its elements. For each application, the specifics of the elements may vary. While their explanation in the light of mass movement analysis comes in the upcoming section, general explanations of the elements are given briefly as follows.

**The images:** Image matching requires two or more *images* that, at least partly, overlap each other. The images should not be unrecognizably distorted in relation to each other. Distortion in this case refers to both geometric and radiometric distortions; and, “*unrecognizably*” is to stress that if the images are highly distorted one way or another in relation to each other, the computer may not be able to successfully match them.

**The matching entities:** For efficiency purposes, the images are not matched as a whole or pixel by pixel. Therefore, a *matching entity* sometimes referred to as a *primitive* has to be identified (Schenk, 1999; Zitová and Flusser, 2003). The different methods of image matching are differentiated based on this fundamental unit of matching.

- (i) When the intensities or intensity transforms of image subsets, usually of square shape and certain size (referred to as templates in this thesis), are used for the matching, the method is called *area-based* matching. If the intensity values are directly used for the matching, the processing is said to be in the *spatial-domain*. If the intensity values are transformed to other domain such as the frequency domain before matching, the processing is said to be in the *transform-domain*.
- (ii) When distinct features with defined attributes are used as matching entities, the method is called *feature-based* matching. The distinct features can be points, lines, edges, regions or global structures. Feature-based method requires existence and *prior* identification of distinct features with accurate computation of their attributes. Accurate computation of the location of the feature attributes is a matter of ongoing research. Its accuracy is thus dependent on the accuracy of feature extraction.
- (iii) A least known matching method called *relational matching* also exists. Structural image descriptions, both features and their relationships, are used in relational matching (Schenk, 1999).

**The search area:** The *search area* is a subset of the search image and requires definition in order to avoid searching in the entire image. It is defined systematically based upon *prior* information regarding the imagery and the surface it represents.

**The similarity measure:** The entities are matched based on certain quantitative parameter, i.e. *similarity measure*, which measures either similarity or dissimilarity between

the matching entities. Examples include the computation of correlation coefficient, sum of squared differences, etc.

**The optimization algorithms:** The geometric precision and radiometric similarity of the matches needs to be optimized using, an *optimization algorithm*. In addition to the optimization, *post-matching filtering* may be conducted to take out wrong matches, due to ambiguity and occlusion. Image matching is generally known as an ill-posed problem because no match (occlusion) or no unique match (ambiguity) may exist (Schenk, 1999).

### 4.3. State-of-the-art area-based image matching for mass movement

#### analysis

Image matching application to mass movement analysis is basically a multi-temporal analysis although multi-view and multi-modal analyses may also be involved. The procedures outlined here focus on area-based spatial-domain image matching method, as it is the most widely used. The discussion starts by mathematical formulation of image matching in 2D space.

Suppose an image of a slope mass is taken at a certain time (for e.g. the left image in Fig. 4-1). The image is then orthoprojected so that its position is fixed on the 2D global coordinate system and the topographic distortion is corrected for. The intensity values of a piece of the slope mass (represented by image template here) is given as  $f(x, y)$ . If image of the same area is taken sometime later (could be days or years depending on the mass movement type), the template will now be moved to a new location with  $dx$  and  $dy$  displacements from its original location. Its new intensity value will be  $t(x-dx, y-dy)$ . The new intensity value will not be equal to  $f(x, y)$  as random noise ( $e$ ) may exist (Eq. 4-1). Due to surface changes, illumination changes or changes in imaging conditions, the intensity values may be changed by systematic gain ( $\lambda$ ) and offset ( $\eta$ ) as given in Eq. 4-2. During movement the template may be deformed, i.e. rotated, compressed/extended, sheared, tilted, or curved as simplified by the dashed quadrilateral of Fig. 4-1. The two geometries are now related by geometric transformation functions ( $g_x$  and  $g_y$ ) that are characterized by parameters ( $p_{1...n}$ ) as shown in Eq. 4-3.

$$f(x, y) = t(x - dx, y - dy) + e \quad 4-1$$

$$f(x, y) = t(x - dx, y - dy)\lambda + \eta + e \quad 4-2$$

$$f(x, y) = t \left( g_x(p_1, \dots, p_n, x, y), g_y(p_1, \dots, p_n, x, y) \right) \lambda + \eta + e \quad 4-3$$

The fundamental problem of image matching is to determine the displacements ( $dx$  and  $dy$ ) so that the residual ( $e$ ) equals or close to zero. As displacement is the unknown, the matching searches for the matching entity which produces the minimum residual ( $e$ ). Due to the likely systematic radiometric changes, the problem is reformulated as finding the right radiometric transformation parameters ( $\lambda$  and  $\eta$ ) so that  $e$  is minimized. In the presence of significant displacement gradient, the functions  $g_x$  and  $g_y$ , characterized by the model parameters  $p_{1...n}$  will be included. The problem is thus finding the exact  $p_{1...n}$  ( $\lambda$  and  $\eta$  included) that minimize  $e$ . In mass movement analysis, radiometric changes and geometric deformation are inevitable. The choice of the correct algorithm that is invariant to the radiometric and at least slight geometric changes (or capable of modeling them) is needed for successful image matching. Furthermore, the success of image matching is dependent on the characteristics of the imagery, matching entity, similarity measure and the search area.

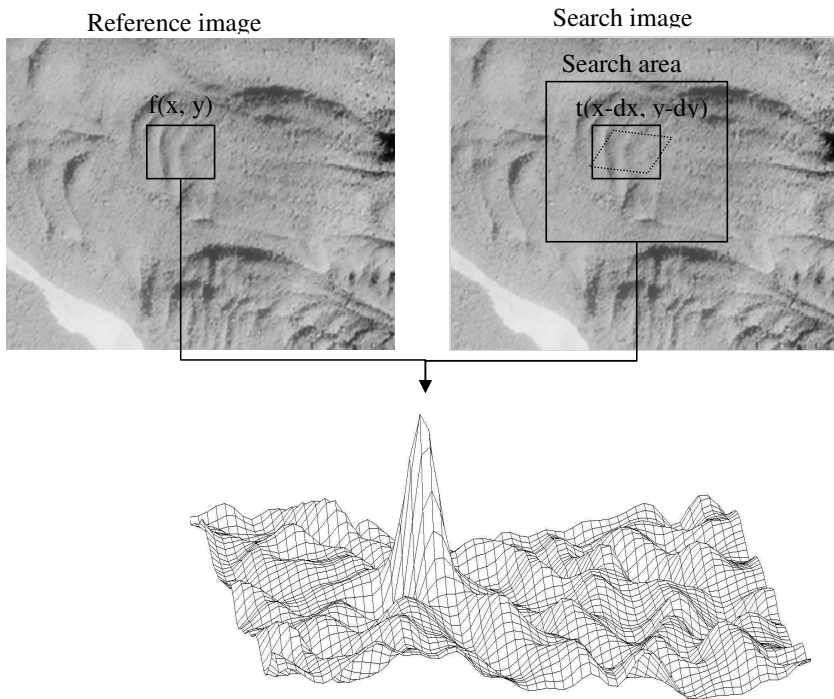


Fig. 4-1 Framework of an area-based image matching task where two images are matched using a similarity maximizing measure such as the NCC

### 4.3.1. Imagery

Multi-temporal images used in image matching for mass movement analysis can be acquired directly for that purpose or selected from the available image archives. Images may be acquired in digital format or digitized from analogue images. A number of imaging characteristics are important in image matching for mass movement analysis: namely, *platform, sensor, spatial, spectral, radiometric and temporal characteristics*.

**Platform and sensor:** Remote sensing images can be acquired from the ground (terrestrial), air and space (satellite). Spatial coverage of the images increases from terrestrial to satellite. When viewing from a long distance, a small field of view can cover a large area. Due to the distance between the sensor and the surface that determines atmospheric influences on the amount of photons detected at the sensor, the smallest ground size detected (scale of observation) will change depending on the platform. Therefore, the choice of image platform for mass movement analysis depends on the level of detail of the investigation. Stability of the platform is also important for geometric precision of the data collected. Highly unstable platforms such as helicopters and balloons are not attractive. The type of lenses may also be important for SNR and geometric precision. Pushbroom sensors as used in many satellites are slightly advantageous in terms of SNR and geometric stability (McCloy, 2006).

**Spatial characteristics:** The spatial characteristics of images include the spatial coverage and resolution. Spatial coverage is the ground area covered by an image scene. Spatial coverage is a factor of the swath width (field of view in angles) of the sensor and the flight height. The choice of the coverage is dependent on the size of the mass movement to be investigated. Spatial resolution is the ground size an image pixel represents, technically referred to as the Ground-projected Sample Interval (GSI). This is also dependent on the sensor and platform characteristics combined with the flight height. A pixel is a discretized unit of the 2D continuous space. The smaller the GSI, the better is the representation of the continuous space. This has a number of implications. (1) When the GSI changes, the scale at which the observation is carried out, and hence the features being observed, change. Investigations show that images over a certain feature attain high signal variance when the ground pixel size is just less than the average size of the surface features (Woodcock and Strahler, 1987). (2) The geometric precision of the observed feature depends on the size of the pixel. Due to the integration of the signal over the pixel, the location of a feature can only be resolved to  $\pm 0.5$  pixel (Schowengerdt, 2007). The implications for image matching are that

the precision of the matching is as good as the GSI unless the matching is conducted with sub-pixel precision. In pixel-precision matching, the displacement in mass movements can be detected only as long as the ground pixel size is less than the displacement magnitude.

Therefore, the choice of the spatial resolution depends on the displacement of the mass movement and the precision required for the mass movement parameters to be computed. High spatial resolution is suited for slow-moving masses. Fast-moving masses can be monitored using lower spatial resolution images as long as the demanded precision is obtained. The effects of pixel size on mass movement parameters and the performances of the different sub-pixel precision algorithms have not been quantified in mass movement analysis. Paper I of this thesis investigated these issues on images of glacier flow, rockglacier creep and land sliding (Debella-Gilo and Kääb, 2011).

**Spectral characteristics:** Spectral characteristics include the EM wavelength region, the width and the number of the spectral channels used for the imaging. Visible and near infrared EM wavelengths are commonly used in photogrammetric applications. Spectral resolution refers to the bandwidth used in the acquisition of the images. The EM wavelength region and bandwidth are important factors for the SNR of the images as the quantity of the photon arriving at the sensor passing through the atmosphere is partially depending on the EM wave region and width. Although single band, panchromatic, is very often used for image matching in mass movement analysis, it is in principle possible to use multiple channels as well (Fookes et al., 2004).

**Radiometric characteristics:** Analogous with the discretization of continuous ground area into the discrete finite pixels, the continuous real radiometric records of a pixel are quantized into discrete (integer) values. For an n-bit image, the dynamic range is  $2^n$  different intensity values. In image matching for mass movement analysis, panchromatic 8-bit images are commonly used. Generally, the higher the dynamic range, the more detail and more resolved the images are although not necessarily increasing the amount of information obtained. For example, higher dynamic range images may increase the contrast of low texture surfaces. However, such contrast may not correlate over long temporal baseline. Further research is needed to investigate the issue, e.g. a cost-benefit analysis.

**Temporal characteristics:** The temporal characteristics include the temporal gap, the season and the time of the day of the images acquisitions. The temporal gap needed is dependent on the velocity of the mass movements. For fast moving masses, short temporal baseline is needed as it is already possible to measure the displacement within the short time and as longer temporal baseline may lead to deformation and destruction of the surface. The

temporal resolution should be long enough and/or the spatial resolution of the images should be high enough for the displacements of the masses to be detected. For measuring glacier flow, temporal gaps ranging from a day to a few years are used. Surface and geometric changes related to melting, crevassing, dirt accumulation and high velocity increase temporal decorrelation. Images with temporal gaps up to decades can be used on rockglaciers and high mountain rockslides as they are not much vegetated and move at slow speeds. Some mass movements occur in areas which change seasonally due to snow, vegetation and cloud cover. To increase the correlation between the images, they have to be acquired during the same season of the year. The possibility of getting no vegetation or snow cover should be utilized so that the relatively permanent surfaces are observed. The time of the day is important too as it affects the illumination. Satellites are commonly constellated to pass over a place at the same time of the day during every pass. Aerial and terrestrial images need such synchronization for optimized correlation.

#### **4.3.2. Preprocessing**

Once appropriate images over a certain mass movement are acquired, there are a number of preprocessing steps to be performed before the actual matching is conducted. These are independent orthorectification and /or co-registration of the images, noise filtering, interest point selections and transformation (where needed).

**Orthorectification and co-registration:** Accurate analysis of mass movement from repeat remotely-sensed images requires precise co-registration of the images. Co-registration errors directly affect the accuracy of the computed movement parameters. As the movements can be very small at places, the co-registration error needs to be well below a pixel so that the displacement magnitudes computed are outside the error margin. If the images are georeferenced with relief distortion corrected, there is no need of subsequent co-registration unless systematic shift is observed. During co-registration, the ground control points to be used should be outside the moving areas as otherwise the co-registration model will contain movement.

**Noise filtering:** Presence of noise in one or both images decreases the matching correlation. Noise in this case is defined as the randomly distributed additive noise (the  $e$  in Eqs. 4-1 to 4-3) originating from the sensor, atmospheric conditions, the viewing angle, surface changes, resampling during orthorectification, etc. Low pass or high pass filters maybe used to reduce noise. Other forms of noise may also exist. Salt-and-pepper noises and

radar speckles can be reduced using geometric filters which can smooth the speckle but preserve features of interest such as edges (Crimmins, 1985). For example, the NCC normalizes scale and offset illumination changes (Lewis, 1995). Orientation correlation is also invariant to scale and offset illumination changes (Fitch et al., 2002), while LSM models the radiometric changes (Förstner, 1982).

**Interest point operators:** Image matching is usually performed on pre-defined points which are selected systematically based on certain criteria. This preprocessing step is particularly crucial in feature-based matching to detect features that will be characterized and matched. Geometrically stable interest points with high information content need to be identified for successful feature-based matching (Schmid et al., 1998). Also in area-based methods, matchable points can be detected. Points that are located in image sections with high SNR are selected excluding textureless areas.

**Transformation:** If the matching is to be performed in the transform domain, the image intensities have to be transformed in to another domain, for e.g. the Fast Fourier Transform, gradient computation.

#### 4.3.3. Identification of matching entities

Image subsets (templates hereafter) are used as matching entities in area-based matching. The size and quality of the template affect the reliability of image matching. A template should contain low noise level and high signal variance (texture). Noise and signal are hardly distinguished in small templates creating an ambiguity problem. In principle, increasing the size of the template makes the template more unique increasing variability and suppressing noise (Okutomi and Kanade, 1990; Schenk, 1999). Unfortunately, increasing the template size increases the geometric distortion within the template. The cause of geometric distortion in mass movement images is displacement gradient (strain). Increasing the template size also increases the computation time exponentially. Finding the matchable template that contains adequate SNR with minimum geometric distortion at each location is not easy. As both SNR and geometric distortion vary spatially, template sizes need to be locally adapted (Kanade and Okutomi, 1994; Okutomi and Kanade, 1990; Okutomi and Kanade, 1992). The local adaptability becomes even more important in Earth surface mass movements due to the often non-rigid motion of these masses leading to displacement gradients and the often necessary long temporal baseline increasing the noise level.



In paper II of this thesis, an algorithm that locally optimizes template sizes based on the SNR and the similarity measure is developed, implemented and evaluated. Candidate templates for matching are identified based on the maximization of SNR, excluding textureless templates. Identification of a candidate template does not guarantee a match. That can be guaranteed by optimizing the similarity measure and excluding occluded templates.

#### **4.3.4. Defining search area**

Searching in an entire image through a “brute force” is not efficient. First, the computational cost is explosively high. Second, there is high chance of getting entity duplicates which create an ambiguity problem. In mass movement images, *prior* information on the maximum displacement together with slope direction (if available) can be used to limit the search distance and direction respectively.

#### **4.3.5. Similarity measures**

The similarity measure quantifies the similarity or dissimilarity between the matching entities. A number of similarity measures exist each with strengths and limitations (Brown, 1992; Zitová and Flusser, 2003). Typical similarity measures are the sum of absolute differences (SAD), sum of squares of differences (SSD), normalized cross-correlation (NCC), least squares (LSM), mutual information, and Fourier invariance properties (Fitch et al., 2002; Foroosh et al., 2002) such as phase correlation, orientation correlation, etc. For mass movement analysis, the choices need to be based on some pre-requisites such as robustness against noise, invariance to some level of deformation, invariance to at least systematic radiometric distortions, precision of the matching location, etc.

The SAD and SSD compute the absolute values and the squares, respectively, of the difference between the intensity values of the corresponding pixels of the reference and the search templates and add their total sum (Eqs. 4-4 and 4-5). In both cases, as dissimilarity is quantified, the template that produces the lowest value is considered the most likely match. They operate in the domain of Eq. 4-1 above as they assume no systematic radiometric and geometric differences. Although they are fast and simple to implement, they are not attractive in mass movement analysis where multi-temporal images with likely high level of noise and geometric deformation are involved.

$$SAD(x, y) = \sum_{x,y}^{r,t} abs[f(x, y) - t(x - dx, y - dy)] \quad 4-4$$

$$SSD(x, y) = \sum_{x,y}^{r,t} [f(x, y) - t(x - dx, y - dy)]^2 \quad 4-5$$

The normalized cross-correlation (NCC) function is developed to overcome the drawbacks of the SAD and SSD (Eq. 4-6). It results in a clear range between -1 and 1, respectively showing complete opposite and exact replica. Thus after computation for all templates in the search area, the one that has the highest NCC coefficient is considered the most likely match. NCC operates in the domain of Eq. 4-2 above as it normalizes systematic radiometric differences but assumes no geometric differences (Nillius and Eklundh, 2002; Lewis, 1995).

The NCC is widely used for matching mass movement images. There are however some limitations related to accuracy and computation. The correlation peak may sometimes be flat lacking sharpness due to possible spatial autocorrelation of the intensity values. Even if sharp, the location of the peak cannot be resolved more precisely than a pixel which can be large for low spatial resolution images. Rigid translation is assumed between the matching templates ignoring the possible change in size, shape and orientation. Although, it is invariant to radiometric offset and gain, a high noise level can still affect the matching. NCC is computationally costly especially when the template and the search area are large as it involves convolution. If an acceleration of the computational speed is needed, Eq. 4-6 can be solved using the Fast Fourier Transform (Lewis, 1995; Haug et al., 2010). NCC in the frequency domain simply replaces the convolution of the NCC in the spatial domain with multiplication.

$$\rho(x, y) = \frac{\sum_{x,y} (f(x,y) - \bar{f})(t(x-dx, y-dy) - \bar{t})}{(\sum_{x,y} (f(x,y) - \bar{f})^2 \sum_{x,y} (t(x-dx, y-dy) - \bar{t})^2)^{1/2}} \quad 4-6$$

The least squares matching (LSM) is a cost minimization function that works based on the L2-norm theorem. The best matching position is sought for by adjusting the geometry and radiometry of the matching template so that the sum of squares of the gray-value deviation between the two templates is minimized (Förstner, 1982; Gruen, 1996). Instead of assuming exact shape and size of the matching templates, the LSM models both the geometric and radiometric distortions. The model parameters are determined iteratively using least squares adjustment. LSM has thus no limitation of precision as the location of the matches can, at least in theory, be determined at any sub-pixel precision. It operates in the domain of Eq. 4-3

above accounting for systematic radiometric changes and geometric deformations. Most commonly affine model is used for both geometric and radiometric changes. However, full projective and second-order polynomial models (Bethmann and Luhmann, 2010) can also be used to fit more advanced geometric deformations. The LSM solves only within a few pixels distance after the approximate matching location is estimated by other simpler and faster method. It is therefore more of an optimization algorithm than a similarity measure.

LSM is a very powerful algorithm that has not been utilized to its full potential in mass movement analysis. In addition to matching images at very high precision, the spatial transformation models can be used to estimate the parameters of deformation such as strain and rotation rates of the mass movements. Only few examples exist for LSM application in mass movement analysis (Kaufmann and Ladstädter, 2003; Maas et al., 2010; Whillans and Tseng, 1995). Paper III of this thesis implemented LSM to images of glacier flow, rockglacier creep and land sliding to compute horizontal surface displacement. Besides, the procedures of computing the deformation parameters from the parameters of the spatial transformation model are also presented. Paper IV of this thesis presents the procedures of implementing advanced spatial transformation models on rockglacier creep and land sliding in a spatially adaptive way.

Other similarity measures that are used either in the transform domain or in other application areas are not considered further in this thesis. For example, mutual information is often used in medical image registration especially for multi-modal image analysis (Pluim et al., 2003). The potentials of phase and orientation correlations of the Fourier domain are investigated in mass movement analysis such as glacier flow (Haug et al., 2010; Michel and Rignot, 1999).

#### **4.3.6. Optimization and post-processing**

If the images are coarse spatial resolution and the similarity measure operates at pixel precision, slow mass movements may not be detected or they may be under or over estimated. A number of sub-pixel algorithms are known to improve the precision, especially in computer vision and mechanics, which use fundamentally different approaches. (1) The images can be interpolated to higher resolution *prior* to matching or on the fly. (2) The correlation surface around the peak of the NCC coefficients can be interpolated to higher resolution. (3) A 2D parabolic or Gaussian curve can be fit to the peak of the NCC surface. These methods simply

attempt to improve the positional precision of the matching without adjusting the radiometry and geometry of the matching entities. Other methods such as LSM attempt to optimize the positional precision of the matching by adjusting the radiometry and geometry of the templates.

Post-matching filtering is conducted to remove false matches due to ambiguity and occlusion. The filtering can be done by thresholding the similarity measure (e.g. the maximum cross-correlation coefficient), the maximum displacement, the displacement direction, coherence of the displacement, etc. Manual filtering or manual setting of filter parameters may have heuristic effects. Thus, if available, systematic and automated approaches are preferred.

#### **4.3.7. Computation of mass movement parameters**

After the matching positions are fixed, what remains is the computation of the mass movement parameters. 2D horizontal surface displacement is computed as the Euclidean distance between the old and the new positions. The horizontal surface velocity is then the displacement divided by the temporal gap between the images' acquisitions.

Strain is basically a derivative of displacement with respect to distance. Strain rate is the derivative of velocity with respect to distance. Strain rates can thus be computed from the velocities obtained using *prior* image matching (Kääb, 2005b). In 2D computations, the horizontal longitudinal and transverse strain rates and shear strain rate can be computed. LSM can be used to compute the rotation and strain rates automatically from the spatial transformation parameters during the matching. The procedures and implantation results are presented in paper III of this thesis. In 3D computation, there are three velocity vectors. Their derivation with respect to distance in the three orthogonal directions gives the nine components of strain rate tensor, i.e. the three normal strain rates and the six shear strain rate components. Stress-strain relationship for the specific material can be used to understand the dynamics of the mass movements.

### **4.3.8. Uncertainties**

#### **4.3.8.1. Sources of error**

There are many sources of error that affect the accuracies of mass movement measurements computed from repeat images. Three sources of error can be characterized: radiometric, geometric and propagated.

The radiometric sources are those that introduce noise and systematic changes to the signal. Sensor noises, atmospheric conditions, illumination and temporal surface changes are the major factors that contribute to the radiometric sources of error. Such sources lead to mismatching and imprecise estimation of the parameters. In multi-temporal images the chances of atmospheric, illumination and surface changes are high even if the sensor noises are kept to minimum.

Geometric sources are those affecting the positional precision and geometric similarity of the matching entities. Pixel size, displacement gradient (deformation), crevassing (in glacier and rockglacier), formation of cracks and gullies, rotation, etc are the major geometric sources. Pixel size affects the precision of the geolocation of the matching entities. Large ground pixel sizes lead to the use of large ground template size which contains large intra-template displacement gradient. Pixel size can be, at least partially, dealt with by using sub-pixel algorithms such as intensity interpolation (paper I) or LSM (paper III). Deformation, formation of crevasses, cracks and rotation make templates different from each other in size, shape and orientation. Inter-template geometric deformation can be reduced by either using optimum template sizes or modeling as in LSM (papers II and III respectively).

Propagated errors are those passed over from the preprocessing steps. Typical preprocessing steps include orthorectification, co-registration, noise filtering, selecting interest points, etc. Any error in one or more of these Preprocessing steps will propagate to the matching and the computed mass movement parameters introducing both radiometric and geometric errors. Orthoprojection errors dominate due to internal and external imaging system errors, errors in the DTM used for the orthoprojection, errors in the projection model parameters and resampling noise. Noise filters generally smooth images reducing the texture.

#### 4.3.8.2. **Total error budget**

The cumulative effects of all sources of error may not be known exactly. Some errors cancel each other while others combine. Quantification of the total error budget and the components of each error source is a deep research topic by itself and therefore will not be addressed here except discussion of the components. The total error budget in area-based image matching for mass movement analysis can be divided into three major components: namely, algorithm-related, image-related and mass movement-related. Each of these has components which contribute to its own error budget.

- (1) *Algorithm error* involves precision, robustness and reliability of the similarity measure. Mismatching (blunders) and misrepresentation due to poor parameterization of the matching algorithm such as non-optimum template size, inappropriate search area size and inefficient or no use of optimization (e.g. sub-pixel) algorithm are typical sources of algorithm error. Algorithm error can be very large determining the success and failure of repeat image matching for mass movement analysis. Matching errors can be reduced by using the correct algorithm and its parameters or making necessary improvements to the algorithm used. Once algorithm errors are corrected or reduced, the other components of the error budget can be dealt with.
- (2) *Orthorectification error* is a major error in image matching for mass movement analysis following the algorithm-related errors. Precise movement measurement is possible only if the images are more precisely orthorectified and co-registered. Displacements to be detected have to be greater than the orthorectification error. Among the different sources of orthorectification errors, DTM errors dominate the total error budget of orthorectification (Lutes, 2002). Unfortunately, relatively high DTM errors are common in steep and rugged terrains where mass movements are prevalent. For frame images, for example, DTM-related orthoprojection error increases from the centre of the scene to the peripheries (Kääb, 2005b). Systematic sensor-related orthorectification errors can be corrected for pushbroom sensors through advanced sensor modeling as used, for example, in the COSI-Corr software (Leprince et al., 2007a; Leprince et al., 2007b).
- (3) The third component of the total error budget is the *temporal decorrelation* of the mass movement images. However precise the matching algorithm and the orthorectification might be, there may still be decorrelation due to significant temporal change of the surface and deformation. Temporal decorrelation leads to mismatching (blunders) and/or misfitting of the matching templates, i.e. misrepresentation. This error component

increases with the temporal baseline between the images. The main solution is therefore using image pairs with appropriate temporal baseline for the movement expected. Another solution may be using preprocessing procedures such as noise filtering, interest operators (e.g. paper II), etc. The matching algorithm needs to be as robust as possible to some levels of these errors.

#### 4.3.9. Evaluation techniques

An ideal method of evaluation is to compare the computed mass movement parameters with their actual values as measured using ground-based methods such as geodetic techniques. When available, these are considered very accurate and provide true comparison to that of matching (Kääb et al., 1997; Kääb and Vollmer, 2000). Such ground-based data seldom exist for many of the high mountain mass movements. Due to seasonal or even shorter-term velocity variations, ground-based validation would require ground measurements synchronous with the image acquisitions which, in practice, are hardly available. Commonly, the algorithms' performances are evaluated based on synthetic images and stable grounds around the moving masses. The following approaches are found to be useful.

**Simulated deformation:** When the displacements and the matching positions in the real multi-temporal images are not known, simulation can be used. The images of the mass movement can be simulated by taking one of the images of the mass movements and applying an analytic deformation and adding random Gaussian noise, offset and gain to the intensity values. In such simulated deformed images, the matching position of every pixel is known together with the geometric transformation parameters. Although this does not exactly represent the real image, it can evaluate the performance of the algorithm under similar and controlled conditions.

**Stable ground around the moving mass:** If the images are accurately orthorectified and co-registered, stable ground on the scene should not show any movement. The displacements and the deformation parameters are expected to be zero on the stable ground. The accuracy of the estimated parameters can then be computed as the deviation from the zero value, assuming that the stable ground well represents the moving masses. This may not always be the case, though. It can however help determine the orthoprojection error.

**Reconstruction of the moving surface:** The assumption behind image matching in mass movements is that although the position and geometry of the masses change their spectral signals remain similar. Therefore, by reconstructing the reference image from the

displaced image, the effectiveness of the matching can be measured using the correlation coefficient between the reference and the reconstructed images. This can be used for comparing different algorithms although it does not provide absolute accuracy. However, it is the only method that evaluates the performance of the algorithm used on the actually moving masses except when true ground data exists. Further detail of this novel approach is given in section 6.5.

Whatever approach is used, the statistics to be used for the evaluation of accuracy is also important. Standard deviation, standard error and root mean square error (RMSE) are sometimes used (Kääb, 2005b). Mean deviation may also be used. Mean deviation measures only the systematic bias of the estimation. Standard deviation measures the blunders. The RMSE is too sensitive to extreme values such as mismatches due to the squaring (Willmott and Matsuura, 2005). Mean absolute error is the mean of the absolute values of the difference between the estimated values and the actual values. Both blunders and biases are included. Every deviation is accounted with its magnitude at the scale of the measurement. The best estimate is, therefore, the one with mean absolute error equal to or close to zero. This statistic is found to be appropriate for evaluating the accuracy of algorithms and methods.



## 5. Conceptual framework

In this thesis the task of analyzing mass movements from repeat remotely-sensed images is viewed as a processing chain which has four major components as shown in Fig. 5-1 multi-temporal images of mass movements are acquired then processed and analyzed using computer-based tools to produce geometric and kinematic properties of the mass movements. The kinematic properties aided by auxiliary data and/or models enable to understand the dynamism of the mass movements.

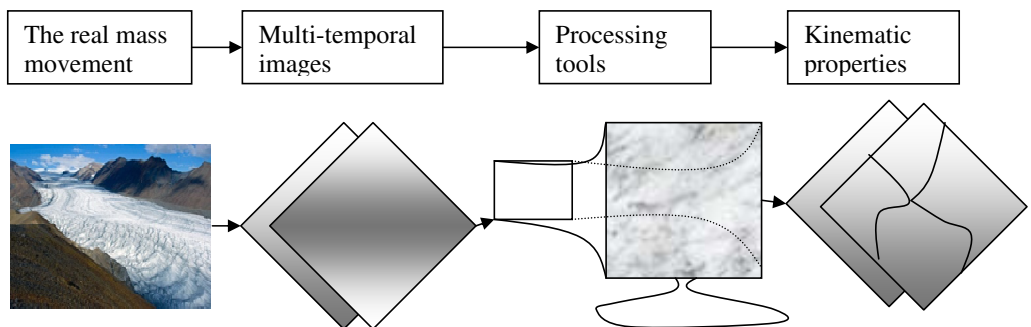


Fig. 5-1 Framework of image matching task for mass movement analysis

(1) **The mass movements.** Three mass movement types are involved in this research: namely, glacier flow, rockglacier creep, and land sliding (Table 5-1). They are very common in high mountains and cold regions and have practical implications, such as geohazards. The regions where they are prevalent are also sensitive to changes in climatic variables such as temperature and the mass movements are good indicators for climate change impacts. The examples used here are mainly from European Alps with some glacier flows in Asia and the Arctic (Svalbard).

(2) **The images.** The images of the masses used in the study are from different platforms, sensors and spatial and temporal resolutions. Table 2 gives summary of the image characteristics used for the specific mass movement type. Pairs of simulated deformation images are also used for evaluation purposes.

(3) **The image processing and analysis tools.** Images are only visual models of reality until they are processed and analyzed after which they produce information about the

reality they represent. The goal of this research work is to push image matching in mass movement analysis towards more accurate (truthiness), more precise (level of detail of measurement), more automated (less required *prior* information and manual interference) and get more thematic output. The NCC and LSM algorithms are used with some algorithm modifications. An image matching tool called Image Matching for Movement Analysis (IMMA) with both the NCC and LSM as similarity measures is scripted and used in MATLAB.

(4) **The thematic outputs.** The outputs per se are not the essential goal of this research, rather the methods are. Nonetheless, displacement (velocity), longitudinal strain rate, transverse strain rate, and rotation rate of the masses are computed. These parameters can be used in other geoscientific applications together with auxiliary data and/or models.

Table 5-1. Main characteristics of mass movements and imagery used in the research

Mass movement		Image pair characteristics			
Type	Location	Platform	Sensor	Spatial resolution	Temporal resolution
<b>Glacier flow</b>	Nigardsbreen, Norwegian mountains	Aerial	Optical	30 cm	10 days
	Kronebreen, Svalbard (Norway)	Satellite (Radarsat)	Microwave	~3 m	25 days
	Ghiacciaio del Belvedere, Italian Alps	Aerial	Optical	50 cm	1 month
	Baltoro, Pakistani Himalaya region	Satellite (Landsat)	Optical	15 m	1 year
<b>Rockglacier creep</b>	Muragl, Swiss Alps	Aerial	Optical	20 cm	13 years
<b>Land sliding</b>	La Clapière, French Alps	Satellite (QuickBird)	Optical	60 cm	7 years
	Aletsch, Swiss Alps	Aerial	Optical	30 cm	30 years

## 6. Summary of papers and other innovations

### 6.1. Ground pixel size effects and sub-pixel algorithms in NCC (paper I)

*Debella-Gilo, M. and A. Kääb (2011). "Sub-pixel precision image matching for measuring surface displacements on mass movements using normalized cross-correlation." Remote Sensing of Environment 115(1): 130-142.*

The NCC is the most widely used similarity measure in image matching for mass movement analysis. However, the fact that its precision is limited to a pixel reduces its accuracy compared to its theoretical potential. The effects of ground pixel size on the accuracy of horizontal displacement of mass movements have not been well investigated. Displacements less than half the ground pixel size cannot be detected. This has implications in particular for low spatial resolution images when applied to slow-moving masses. In most high mountain regions medium and low spatial resolution satellite images are the only available image data. Such images can be utilized optimally if appropriate techniques are used. A number of sub-pixel algorithms are available. They are mainly adapted from other application areas, such as computer vision, and applied in mass movements without thorough evaluation and comparison. The algorithms basically use two major approaches. (1) Interpolating the images to higher resolution *prior* to matching. (2) Computing the location of the NCC peak from the correlation surface with higher precision using different techniques.

Paper I presents a study conducted to investigate the effects of ground pixel size on the accuracy of horizontal surface displacement and to evaluate and compare the two different approaches of sub-pixel precision algorithms. The NCC-based image matching is conducted on image pairs of different resolution created through resampling to evaluate the effects of the change in the spatial resolution. The two sub-pixel approaches are also implemented and evaluated. In one of the two sub-pixel precision approaches, image intensities are interpolated to a desired sub-pixel resolution using a bi-cubic interpolation scheme *prior* to the actual displacement matching. In the second approach, the image pairs are correlated at the original image resolution and the peaks of the correlation coefficient surface are then located at sub-pixel resolution using three techniques, namely bi-cubic interpolation, parabola-fitting and Gaussian-fitting. Both principal approaches are applied to three typical mass movement types

from European Alps: rockglacier creep, glacier flow and land sliding. The results show that bi-cubic interpolation of image intensity performs best followed by bi-cubic interpolation of the correlation surface. By increasing the spatial resolution (i.e. reducing the ground pixel size) of the matched images by 2 to 16 times using intensity interpolation, 40% to 80% reduction in mean error in reference to the same resolution original image could be achieved. Both Gaussian and parabolic peak locating turn out less accurate. The study also quantifies how the mean error, the random error, the proportion of mismatches and the proportion of undetected movements increase with increasing pixel size (i.e. decreasing spatial resolution) for all of the three mass movement examples investigated. By using image interpolation *prior* to matching, available low resolution images can be utilized for precise analysis of slow-moving masses.

## **6.2. Locally adaptive optimum template sizes for the NCC algorithm (paper**

### **II)**

*Debella-Gilo, M. and A. Kääh (2011). "Locally adaptive template sizes for matching repeat images of Earth surface mass movements." ISPRS Journal of Photogrammetry and Remote Sensing Revision submitted.*

The main requirements of a matching entity in area-based matching are the presence of adequate image texture (signal variance) and the absence of noise. Templates that lack texture and small templates that are not unique enough result in ambiguous matching. In principle, increasing the size of the template makes the template more unique (Okutomi and Kanade, 1990; Schenk, 1999). However, increasing template size poses two challenges. First, it increases the computation time exponentially. Second, it increases geometric distortion within the template. The challenge in deciding template size is therefore finding the optimum size that contains high signal variation in relation to noise variation (i.e. adequate signal-to-noise ratio) with minimum geometric distortion. As these parameters vary spatially, template sizes need to be locally adapted (Kanade and Okutomi, 1994; Okutomi and Kanade, 1990; Okutomi and Kanade, 1992). The local adaptability becomes even more important in Earth surface mass movements due to the often non-rigid motion of these masses and the often necessary large temporal baseline.

Paper II presents an algorithm for locally adaptive template sizes in NCC-based image matching. The algorithm relies on two important facts. Firstly, the SNR of an image subset

attains peak when the noise is minimized and the signal variance is maximized. Such peak is attained due to edge crossing (object boundaries) or when the signal gets saturated due to lack of new source of signal variation. Textureless regions lack this SNR peak. Secondly, when the peak of NCC coefficient is computed together with the matching position for increasing template sizes, the value of the peak decreases first due to noise and then increases again, attaining a peak at the size where the noise is maximally suppressed and geometric distortion is still low. The matching position of the template gets fixed just before attaining the peak. Ambiguous and occluded templates either lack the peak or their matching positions do not get fixed. Therefore, the spatially adaptive algorithm for template sizes identifies candidate templates based on the SNR peak and then iteratively looks for the size at which the cross-correlation coefficient attains a local peak and the matching position gets fixed. The algorithm is tested on simulated deformation images and applied to real bi-temporal images of different Earth surface mass movements. The evaluation of the algorithm was conducted on simulated deformation images and in relation to the image-wide fixed template sizes ranging from 11 to 101 pixels. The evaluation of the algorithm on the real mass movements is conducted by a novel technique of reconstructing the reference image from the deformed image and computing the global correlation coefficient and the corresponding SNR between the reference and the reconstructed image. The results show that the algorithm could reduce the error of displacement estimation by up to over 90% (in the simulated case) and improve the SNR of the matching by up to over 4 times compared to the globally fixed template sizes. The algorithm highly reduces the effects of geometric distortion and noise. Besides, it effectively excludes most of the templates that lack adequate SNR from the analysis through its candidate selection step and excludes occluded templates in the second step. The algorithm pushes terrain displacement measurement from repeat images one step forward towards full automation as it overcomes the choice of template sizes by an operator, which is subjective and not spatially adaptive and requires experience.

### **6.3. LSM for displacement and deformation measurement (paper III)**

*Debella-Gilo, M. and A. Kääh (2011). "Surface displacement and deformation on mass movements using least squares matching of repeat images." Remote Sensing Revision submitted.*

In response to the shortcomings of correlation-based and other similarity measures, the Least Squares Matching (LSM) was developed (Förstner, 1982). Instead of assuming exact shape

and size of the matching templates, the LSM models both the geometric and radiometric distortions. The model parameters are determined iteratively using least squares adjustment by changing the shape and size of the matching entities. In so doing the LSM matches images accurately at sub-pixel precision. Although the algorithm is popular in photogrammetric stereo vision, there are very few applications in mass movement analysis (Bethmann and Luhmann, 2010; Kaufmann and Ladstädter, 2003; Whillans and Tseng, 1995). There is a lack of wider application and evaluation of the algorithm on different mass movement types. Besides, the capability of the algorithm to model deformation is not utilized further except precisely locating the matching positions for displacement estimation. Strain rates are usually computed in a post-processing step from the velocity gradients (Kääb, 2005b).

Paper III presents the procedures of exploring the potential of automatically computing displacement, rotation and strain rates of Earth surface mass movements directly and simultaneously from the matching positions and from the parameters of the geometric transformation models of the LSM. The procedures are exemplified for aerial and satellite images of glacier flow, rockglacier creep and land sliding. The performance of the algorithm is evaluated on the stable grounds, simulated deformed image pairs and on the mass movement itself. The results show that the approach computes longitudinal strain rates, transverse strain rates and shear strain rates reliably with mean absolute deviation in the order of  $10^{-4}$  as evaluated on stable grounds. The LSM also improves the accuracy of displacement estimation of the NCC by over 90% in the ideal (simulated) case and by about 25% in real multi-temporal images of mass movements. The performances are higher on glacier flow and rockglacier creep images with their coherent flow fields, limited surface changes and accurate co-registration (in the present study) as opposed to the land sliding images analyzed.

## **6.4. Spatially adaptive and higher-order transformation models in LSM**

### **(paper IV)**

*Debella-Gilo, M. and A. Kääb (2011). Monitoring slow-moving landslides using spatially adaptive least squares image matching. The Second World Landslide Forum. Rome, Italy.*

*Accepted*

In the few applications of the LSM algorithm in mass movement analysis, only the affine geometric model is used for the entire scene (Bethmann and Luhmann, 2010; Kaufmann and Ladstädter, 2003; Whillans and Tseng, 1995). The affine model incorporates movements that

involve change in position, linear and constant changes in size in each direction (i.e. scaling), and shearing. However, Earth surface masses can also be tilted, diverged/converged and deformed non-linearly depending on the form, process and material of the slope. The problem gets more complicated as in reality the pattern of deformation can vary spatially on a slope. One geometric model may thus not fit to all deformation types on a slope. LSM with higher-order spatial transformation models such as the projective and second-order polynomial (Bethmann and Luhmann, 2010) have not been used in mass movement analysis.

Paper IV presents and evaluates an algorithm which uses the LSM with spatially adaptive and high-order geometric models to estimate horizontal surface displacements of slow-moving landslides from repeat optical aerial and satellite images. Affine, projective and second-degree polynomial geometric models are included. Pairs of high resolution optical images over a rockglacier creep and a slow-moving landslide are orthorectified and co-registered. Image matching is applied first using the conventional NCC, then using the LSM algorithm with image-wide single geometric models, and finally using the LSM with spatially adaptive geometric models. The spatially adaptive algorithm operates in such a way that for each template the model that produces the lowest sum of square of intensity difference is considered the best fitting model. The approaches are evaluated in reference to the NCC algorithm based on the SNR of reconstructing the reference image from the search image. In general, over 25% improvement in the SNR gain is obtained when the LSM algorithms are used compared to the NCC algorithm. In both cases, the spatially adaptive algorithm performs the best closely followed by the image-wide second-order polynomial model. The image-wide affine and projective models perform alike. The performance of the spatially adaptive approach is a clear indication of the spatial variation of the mode of deformation of the masses. In the spatially adaptive case, majority of the image templates matched (over 60%) are found to fit the second-order polynomial model as it can model first-order deformations as well.

## **6.5. Other innovations of the thesis**

Apart from the articles presented, the research has come up with some other novel techniques that are explained as follows.

### **The use of SNR of image reconstruction for evaluation**

The use of simulated deformation in the evaluation of an image matching task may not give the real accuracy. Simulated deformations lack the complexity of real mass movements. The representation of temporal radiometric changes with Gaussian noise and the geometric deformations with single spatial transformation model cannot fully represent real mass movements. They can however evaluate the reliability of the algorithm under a control condition.

The use of stable ground for accuracy evaluation is closer to the real mass movements. Although it shares the temporal differences between the images, stable ground lack the deformation that the mass movements undergo. The deformation can create radiometric changes. In addition, the stable ground may not adequately represent further conditions on the mass movement, such as texture, topography, etc. The level of accuracy on the stable ground may thus not necessarily represent that on the moving ground.

Image matching is used in mass movement analysis based on the assumption that although the masses are displaced and deformed, the radiometry of the masses remain generally similar. This has the implication that if every deformed pixel is accurately identified and moved back to its original position, the two matching images will correlate image-wide. The better the matching algorithm, the higher is the image-wide correlation ( $\rho$ ) between the reference and the reconstructed image. The *SNR* is then computed as given in Eq. 6-1. The *SNR* before the matching ( $SNR_{rd}$ ) and after the reconstruction ( $SNR_{rr}$ ) can then be computed to see the gain in the *SNR* by the specific matching algorithm used (Eq. 6-2 and Fig. 6-1).

$$SNR = \frac{\rho}{1-\rho} \tag{6-1}$$

$$SNR(gain) = SNR_{rr} - SNR_{rd} \tag{6-2}$$



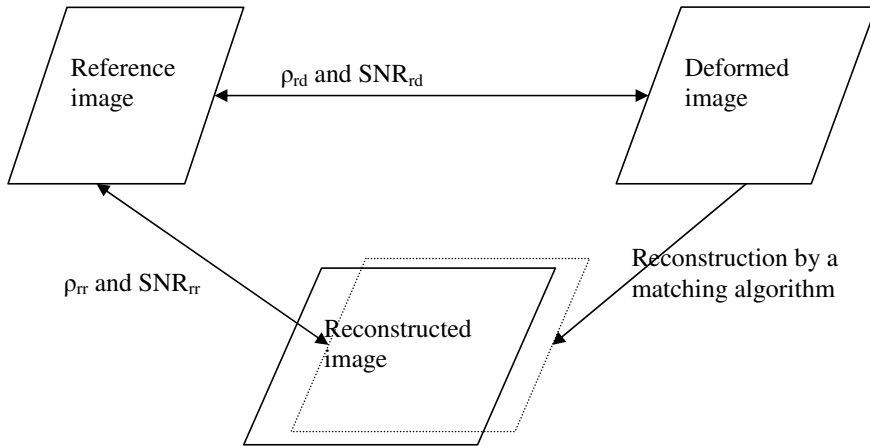


Fig. 6-1. Image reconstruction and computation of the SNR gain.  $\rho_{rd}$  and  $SNR_{rd}$  are the global correlation coefficient and the corresponding SNR (respectively) between the reference (older) and the deformed (recent) images, while the  $\rho_{rr}$  and  $SNR_{rr}$  are the global correlation coefficient and the corresponding SNR (respectively) between the reference and the reconstructed images.

This approach has some limitations. Firstly, it does not give absolute quantity of the errors in terms of mass movement parameters such as displacement or strain rate. It is, however, useful for comparing different methods and algorithms. Empirical tests show that the relative gain in the SNR is comparable to relative gain in the accuracy of the computed displacement. Secondly, the approach fails in low texture areas as the SNR appears to be high already before the matching. This problem is not specific to this approach but common to area-based image matching. Textureless areas are not reliably matched in area-based method anyway.

### Spatially adaptive interest operator

The study has found out that if a pixel is taken and the SNR of windows around the pixel are computed consecutively every time increasing the window size, for regions with good texture there will be a size at which the SNR attains a certain peak(s). This peak shows the size at which the noise variance is minimized and the signal variance is maximized within the defined maximum size. It is the size at which the information content per image (not ground) size is optimized. Besides, the peak is found to be coinciding with edges as shown for the rockglacier image subset of Fig. 6-2. Such image subsets with maximized SNR are good candidates for area-based matching. Image regions lacking signal variability lack the SNR

peak and can easily be excluded from the matching (e.g. shadow image subset of Fig. 6-2). This operator can be used to exclude areas lacking adequate SNR from the matching.

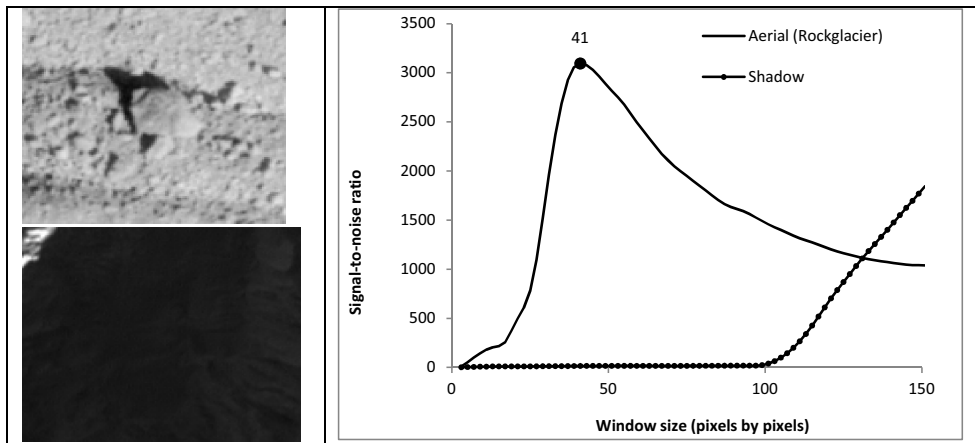


Fig. 6-2. Signal-to-noise ratio together with the first local maximum (right) as plotted against the window size for an aerial image of real rockglacier section (upper left) shadow area (lower left). The smooth line is for the rockglacier and the dotted line is for the shadow area.

### Spatially adaptive matching optimizer

Even if we have a good matching candidate, there is no guarantee that it will have one (not occluded) and only one (unambiguous) match. A good way to ensure that is by using the cross-correlation coefficient. For a given template size, the peak of cross-correlation values in the search image shows the most likely match. With the same token, if we compute this peak and the accompanying matching position for different template sizes increasing from small size, the first peak of the peaks, if accompanied by fixed matching position, shows the optimum size of the template (**Fig. 6-3**). At this size the noises are maximally suppressed and the displacement gradient is still under a pixel. The matching position of the templates is fixed around this size. Occluded templates lack such peak, while ambiguous templates lack stable matching position together with the peak (paper II). This operator can be used together with the above operator to exclude occluded and ambiguous matches and to find the optimum size of the template. If there is no geometric and radiometric difference between the two images, the peak of SNR overlaps the peak of the peaks of NCC. For a given template, if the template is deformed during the movement, the NCC optimizes at smaller template size; where as if there is great radiometric difference (noise) the NCC optimizes at larger templates. In reality there is a combination of the two. As a result, the SNR peak and the peak of the NCC peaks will not often overlap but will be close to each other.

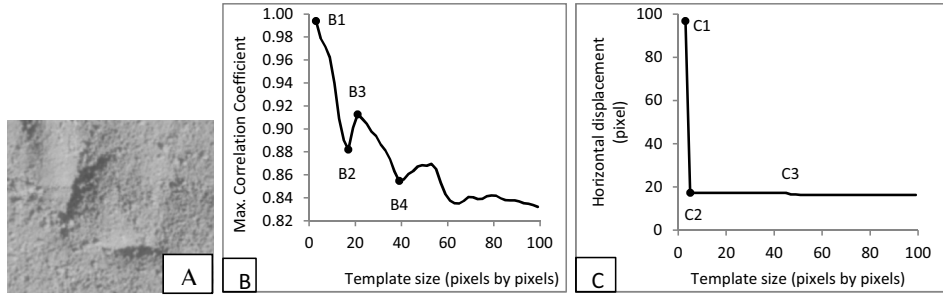


Fig. 6-3. The relationship between template size and the maximum NCC coefficient (B) and the displacement estimates (C) for an image subset (A) that contains good signal variance.

Fig. 6-3 shows that the NCC peak is high at point B1 due to random duplicates. The matching position is random and changes with the next template size (C1). When the size increases further, the NCC peak then decreases due to the increased noise with addition of more pixels until point B2. With further increase of template size, the noises get suppressed and the signal starts to dominate. The matching position may already be fixed before the NCC maximum attains a peak (C2). As a result the NCC peak increases until the noise is maximally suppressed. The NCC maximum attains a peak (B3) where the noise is maximally suppressed and the geometric difference between the matching templates is still low. The peak starts to decrease again due to the geometric distortion within the now large template. The NCC peak attains a new low (B4) when the displacement gradient is close to full pixel. When the gradient attains full pixel, the matching position shifts by a pixel (C3) showing the influence of large template sizes on the accuracy of matching positions. B3 thus shows the optimum NCC peak with optimum template size as the matching position is also stable before and after that size (from C2 to C3).



## 7. Conclusions and outlook

Review of the application of image matching in mass movement analysis shows that the correlation-based algorithms, especially the NCC, are the most widely used algorithms. The major limitations of the correlation-based algorithms in the spatial-domain are addressed in this research.

The precision of the NCC is limited to a pixel. The implication of the pixel size on the computed mass movement parameters such as the accuracy of the horizontal displacement is investigated. Not surprisingly, the investigations show that the detectability of mass movements and accuracy of the computed parameters such as displacement decrease with increasing ground pixel size. Therefore, the need for additional algorithms for refining the matching positions at sub-pixel precision increases with increasing ground pixel size of the images used. Of the available sub-pixel algorithms, interpolating the images to higher resolution *prior* to the matching results in better accuracy of the matching. This is followed by the interpolation of the NCC correlation surface to higher resolution. Computation of the position of the NCC peak using models such as Gaussian and parabolic do not necessary result in accurate peak localization due to the deviation of the correlation surface of low resolution images from these models. These functions perform better than interpolating the image to one-half a pixel only. However, interpolating to more detailed spatial resolution than  $1/16^{\text{th}}$  of the original resolution is highly affected by interpolation noise.

The challenge of spatially adapting template sizes for the NCC algorithm is addressed in this research. The following facts, learnt during the investigation, helped in developing an algorithm that spatially adapts the template sizes. (1) When the size of an image subset increases, the SNR also increases. If a certain edge or feature boundary is encountered, the SNR attains a peak at that boundary. Even if there is no feature boundary but the image subset contains texture, the SNR gets a certain peak at certain sizes due to saturation of information. Such SNR peak identifies (the size of) a unique entity. Monotonous image regions such as shadow, water surface, snow, cloud, etc lack such SNR peak and can therefore be excluded as textureless. (2) Analogous with the fact that the peak of NCC in a search window shows the most likely match, the peak of the NCC peaks, when computed for increasing window sizes, accompanied with fixed matching position indicates the size at which noise is maximally suppressed and signal is maximally matched due to the still limited intra-template deformation. If such peak does not exist or is not accompanied by a fixed matching position,

then the template is either ambiguous (as in textureless areas) or occluded (as in matchless templates) avoiding the heuristic manual post-matching filtering. Therefore, the spatially adaptive algorithm can exclude textureless regions and occluded (permanently changed areas) from the matching and optimize the size of the matchable templates. In so doing it improves the reliability and accuracy of the matching and the computed movement parameters. The image matching task is then more automated as template sizes are determined computationally.

The NCC is appropriate only where the deformation within the template is not significant. LSM is found to be very suitable in highly deformed mass movements both for accurate matching and for the estimation of the deformation parameters. The LSM improves the accuracy of displacement estimation of the NCC significantly (at least by 25% in the present study). It is also able to compute rotation and strain rates automatically during the matching with high spatial resolution and very high accuracy, i.e. with mean absolute error in the order of  $10^{-4}$ . LSM searches only in a couple of pixels distance, requiring that approximate position of the match is located first using other methods such as the NCC.

The deformation of the masses is spatially variable and can not be optimally modeled using single spatial transformation model such as the affine. Deformations of the mass movements investigated are more accurately modeled by second-order polynomial function. Spatially adapting the transformation models using affine, projective or second-order polynomial improves the accuracy further as the most fitting model is used for each image subset improving the accuracy of the matching and the derived mass movement parameters.

The general conclusion is that the NCC is useful in all mass movement analyses as long as there is adequate signal variance. NCC alone may be sufficient for low resolution images of moving masses with limited or no deformation. To gain better precision in such cases, the images need to be interpolated to higher resolution (better not finer than  $1/16^{\text{th}}$  of a pixel) *prior* to the matching. For highly deformed masses where higher resolution images are used, the LSM is recommended as it results in much more accurate matching. Longitudinal, transverse and shear strain rates can be computed reliably and at higher precision using the transformation parameters of the LSM. Such strain rates show detailed spatial variation which could be used for other geoscientific applications. Improved accuracy and precision can be obtained by selecting matchable areas using the first part of the spatially adaptive algorithm and optimizing the matches and measuring the deformation parameters using the LSM algorithm.

The algorithms devised and used in this research are computationally costly. Computational issues can be addressed through faster programming and faster computers that are becoming more available. Attention should, therefore, be paid to the precision, accuracy, robustness and automation of the algorithms. Although the algorithms can get precise, the accuracy of the matching and the computed mass movement parameters can be challenged by the other sources of error. The other components of the total error budget need to be addressed through further research.

This study focused on two similarity measures used in the spatial-domain area-based optical image matching, namely NCC and LSM. There needs to be more application of LSM in mass movement analysis under different conditions as it is promising especially for precise computation of displacement and strain rates.

Other similarity measures used in other fields such as medical image matching and computer vision may also have potential in some types of mass movement images. For example, the mutual information is a similarity measure used in medical image matching for registering multimodal images. The potential of using multimodal images in mass movements also exists. The potential of the mutual information in mass movement analysis needs to be investigated in relation to the NCC, LSM and the other algorithms through further researches.

Repeat images are also successfully matched in the transform-domain for mass movement analysis (Haug, 2010). For example the Fourier domain algorithms such as Fourier Phase correlation, orientation correlation, etc are used for displacement measurement on glacier flow (Haug et al., 2010; Michel and Rignot, 1999). The relative strengths and limitations of these transform-domain methods and the aforementioned spatial-domain methods when used for mass movement analysis need to be investigated through further researches.

Although area-based image matching methods are widely used for mass movement analysis, the potential of feature-based matching also exists, especially for high spatial and temporal resolution images of high texture areas. The challenges in feature-based matching are accurate identification and characterization of distinct features which can be even more difficult in mass movement images. The potentials of combining area-based and feature-based image matching methods for mass movement analysis need to be explored through further researches.

Further research needs to be geared towards integrating the different techniques of remote sensing, i.e. photogrammetry, laser scanning and InSAR. The weaknesses of one can be addressed by the others so that 3D deformation with good spatial extent could be obtained. When 3D deformation is reliably computed it can be used together with auxiliary data and/or

models to understand the dynamism of mass movements. The deformation data can also be used for other geo-scientific purposes in multi-disciplinary studies of a wider scope.



## 8. References

- Abdalati, W., Krabill, W., Frederick, E., Manizade, S., Martin, C., Sonntag, J., Swift, R., Thomas, R., Wright, W., and Yungel, J., 2001, Outlet glacier and margin elevation changes: Near-coastal thinning of the Greenland ice sheet: *J. Geophys. Res.*, v. 106, no. D24, p. 33729-33741.
- Abdalati, W., and Krabill, W. B., 1999, Calculation of Ice Velocities in the Jakobshavn Isbrae Area Using Airborne Laser Altimetry: *Remote Sensing of Environment*, v. 67, no. 2, p. 194-204.
- Andreassen, L. M., Elvehøy, H., Kjølmoen, B., 2002, Using aerial photography to study glacier changes in Norway: *Annals of Glaciology*, v. 34, no. 1, p. 343-348.
- Arenson, L., Hoelzle, M., and Springman, S., 2002, Borehole deformation measurements and internal structure of some rock glaciers in Switzerland: *Permafrost and Periglacial Processes*, v. 13, no. 2, p. 117-135.
- Baltsavias, E. P., 1999, A comparison between photogrammetry and laser scanning: *ISPRS Journal of Photogrammetry and Remote Sensing*, v. 54, no. 2-3, p. 83-94.
- Bamler, R., and Hartl, P., 1998, Synthetic aperture radar interferometry: *Inverse Problems*, v. 14, no. 4, p. R1.
- Barsch, D., 1992, Permafrost creep and rockglaciers: *Permafrost and Periglacial Processes*, v. 3, no. 3, p. 175-188.
- Bauer, A., Paar, G., and Kaltenböck, A., 2006, Mass movement monitoring using terrestrial laser scanner for rockfall management, *in* van Oosterom, P., Zlatanova, S., and Fendel, E. M., eds., *Geo-information for Disaster Management: Berlin Heidelberg*, Springer, p. 393-406.
- Bauer, A., Paar, G., and Kaufmann, V., Terrestrial laser scanning for rock glacier monitoring, *in* *Proceedings Eighth International Conference on Permafrost*, Zurich, Balkema, 2003, Volume 1, Swets & Zeitlinger, Lisse, p. 55-60.
- Beniston, M., 2003, Climatic Change in Mountain Regions: A Review of Possible Impacts: *Climatic Change*, v. 59, no. 1, p. 5-31.
- Bethmann, F., and Luhmann, T., Least-squares matching with advanced geometric transformation models, *in* *Proceedings International Archives of Photogrammetry, Remote Sensing and Spatial Information Sciences Commission V Symposium*, Newcastle upon Tyne, UK, 2010, Volume XXXVIII, Commission V, WG V/4, p. 86-91.
- Bindschadler, R. A., and Scambos, T. A., 1991, Satellite-Image-Derived Velocity Field of an Antarctic Ice Stream: *Science*, v. 252, no. 5003, p. 242-246.
- Brown, L. G., 1992, A survey of image registration techniques: *ACM Comput. Surv.*, v. 24, no. 4, p. 325-376.
- Caris, J. P. T., and Van Asch, T. W. J., 1991, Geophysical, geotechnical and hydrological investigations of a small landslide in the French Alps: *Engineering Geology*, v. 31, no. 3-4, p. 249-276.
- Casson, B., Delacourt, C., and Allemand, P., 2005, Contribution of multi-temporal remote sensing images to characterize landslide slip surface - Application to the La Clapière landslide (France): *Natural Hazards and Earth System Sciences*, v. 5, no. 3, p. 425-437.

- Casson, B., Delacourt, C., Baratoux, D., and Allemand, P., 2003, Seventeen years of the "La Clapière" landslide evolution analysed from ortho-rectified aerial photographs: *Engineering Geology*, v. 68, no. 1-2, p. 123-139.
- Catani, F., Casagli, N., Ermini, L., Righini, G., and Menduni, G., 2005a, Landslide hazard and risk mapping at catchment scale in the Arno River basin: *Landslides*, v. 2, no. 4, p. 329-342.
- Catani, F., Farina, P., Moretti, S., Nico, G., and Strozzi, T., 2005b, On the application of SAR interferometry to geomorphological studies: estimation of landform attributes and mass movements: *Geomorphology*, v. 66, no. 1-4, p. 119-131.
- Cloude, S. R., and Papathanassiou, K. P., 1998, Polarimetric SAR interferometry: *Geoscience and Remote Sensing, IEEE Transactions on*, v. 36, no. 5, p. 1551-1565.
- Colesanti, C., Ferretti, A., Prati, C., and Rocca, F., 2003, Monitoring landslides and tectonic motions with the Permanent Scatterers Technique: *Engineering Geology*, v. 68, no. 1-2, p. 3-14.
- Copland, L., Pope, S., Bishop, M. P., Shroder, J. F., Clendon, P., Bush, A., Kamp, U., Seong, Y. B., and Owen, L. A., 2009, Glacier velocities across the central Karakoram: *Annals of Glaciology*, v. 50, no. 52, p. 41-49.
- Crimmins, T. R., 1985, Geometric filter for speckle reduction: *Applied Optics*, v. 24, no. 10, p. 1438-1443
- Debella-Gilo, M., and Käab, A., 2011, Sub-pixel precision image matching for measuring surface displacements on mass movements using normalized cross-correlation: *Remote Sensing of Environment*, v. 115, no. 1, p. 130-142.
- Dehn, M., Bürger, G., Buma, J., and Gasparetto, P., 2000, Impact of climate change on slope stability using expanded downscaling: *Engineering Geology*, v. 55, no. 3, p. 193-204.
- Delacourt, C., Allemand, P., Berthier, E., Raucoules, D., Casson, B., Grandjean, P., Pambrun, C., and Varel, E., 2007, Remote-sensing techniques for analysing landslide kinematics: a review: *Bulletin De La Societe Geologique De France*, v. 178, no. 2, p. 89-100.
- Delacourt, C., Allemand, P., Casson, B., and Vadon, H., 2004, Velocity field of the "La Clapière" landslide measured by the correlation of aerial and QuickBird satellite images: *Geophys. Res. Lett.*, v. 31, no. 15, p. 15-19.
- Dewitte, O., Jasselette, J. C., Cornet, Y., Van Den Eeckhaut, M., Collignon, A., Poesen, J., and Demoulin, A., 2008, Tracking landslide displacements by multi-temporal DTMs: A combined aerial stereophotogrammetric and LIDAR approach in western Belgium: *Engineering Geology*, v. 99, no. 1-2, p. 11-22.
- Evans, S. G., and Clague, J. J., 1994, Recent climatic change and catastrophic geomorphic processes in mountain environments: *Geomorphology*, v. 10, no. 1-4, p. 107-128.
- Ferretti, A., Prati, C., and Rocca, F., 2001, Permanent scatterers in SAR interferometry: *Geoscience and Remote Sensing, IEEE Transactions on*, v. 39, no. 1, p. 8-20.
- Fitch, A. J., Kadyrov, A., Christmas, W. J., and Kittler, J., Orientation Correlation, *in Proceedings Proc. British Machine Vision Conference 2002*, Volume 1, p. 133-142.
- Fookes, C., Maeder, A., Sridharan, S., and Cook, J., Multi-spectral stereo image matching using mutual information, *in Proceedings 3D Data Processing, Visualization and Transmission, 2004. 3DPVT 2004. Proceedings. 2nd International Symposium on 6-9 Sept. 2004*, p. 961-968.
- Foroosh, H., Zerubia, J. B., and Berthod, M., 2002, Extension of phase correlation to subpixel registration: *Image Processing, IEEE Transactions on*, v. 11, no. 3, p. 188-200.
- Förstner, W., On the geometric precision of digital image correlation, *in Proceedings Proceedings of the ISPRS Symposium Mathematical Models, Accuracy Aspects and*

- Quality Control, Finland, 1982, Volume 24, International Archives of Photogrammetry, p. 176-189.
- Goldstein, R. M., Zebker, H. A., and Werner, C. L., 1988, Satellite radar interferometry: Two-dimensional phase unwrapping: *Radio Sci.*, v. 23, no. 4, p. 713-720.
- Gruber, S., and Haeberli, W., 2007, Permafrost in steep bedrock slopes and its temperature-related destabilization following climate change: *J. Geophys. Res.*, v. 112, no. F2, p. F02S18.
- Gruen, A., 1996, Least squares matching: a fundamental measurement algorithm, *in* Atkinson, K. B., ed., *Close range photogrammetry and machine vision*: Caithness, Scotland, Whittles Publ., p. 217-255.
- Haeberli, W., and Beniston, M., 1998, Climate Change and Its Impacts on Glaciers and Permafrost in the Alps: *Ambio*, v. 27, no. 4, p. 258-265.
- Haeberli, W., Hallet, B., Arenson, L., Elconin, R., Humlum, O., Kääb, A., Kaufmann, V., Ladanyi, B., Matsuoka, N., Springman, S., and Mühl, D. V., 2006, Permafrost creep and rock glacier dynamics: *Permafrost and Periglacial Processes*, v. 17, no. 3, p. 189-214.
- Hart, J., and Rose, J., 2001, Approaches to the study of glacier bed deformation: *Quaternary International*, v. 86, no. 1, p. 45-58.
- Haug, T., Kääb, A., and Skvarca, P., 2010, Monitoring ice shelf velocities from repeat MODIS and Landsat data - a method study on the Larsen C ice shelf, antarctic Peninsula, and 10 other ice shelves around Antarctica: *The Cryosphere*, v. 4, no. 1, p. 161-178.
- Hilley, G. E., Bürgmann, R., Ferretti, A., Novali, F., and Rocca, F., 2004, Dynamics of Slow-Moving Landslides from Permanent Scatterer Analysis: *Science*, v. 304, no. 5679, p. 1952-1955.
- Hofton, M. A., and Blair, J. B., 2002, Laser altimeter return pulse correlation: a method for detecting surface topographic change: *Journal of Geodynamics*, v. 34, no. 3-4, p. 477-489.
- Hooke, R. L., 2005, *Principles of glacier mechanics*, Cambridge, Cambridge University Press, XVII, 429 s. p.:
- Hooper, A., Segall, P., and Zebker, H., 2007, Persistent scatterer interferometric synthetic aperture radar for crustal deformation analysis, with application to Volcán Alcedo, Galápagos: *J. Geophys. Res.*, v. 112, no. B7, p. B07407.
- Hsing-Chung, C., Linlin, G., Rizos, C., and Milne, T., Validation of DEMs derived from radar interferometry, airborne laser scanning and photogrammetry by using GPS-RTK, *in* *Proceedings Geoscience and Remote Sensing Symposium, 2004. IGARSS '04. Proceedings. 2004 IEEE International20-24 Sept. 2004 2004*, Volume 5, p. 2815-2818 vol.2815.
- Janke, J. R., 2005, Photogrammetric Analysis of Front Range Rock Glacier Flow Rates: *Geografiska Annaler: Series A, Physical Geography*, v. 87, no. 4, p. 515-526.
- Jones, L. D., 2006, Monitoring landslides in hazardous terrain using terrestrial LiDAR: an example from Montserrat: *Quarterly Journal of Engineering Geology and Hydrogeology*, v. 39, no. 4, p. 371-373.
- Kanade, T., and Okutomi, M., 1994, A stereo matching algorithm with an adaptive window: theory and experiment: *IEEE Transactions on Pattern Analysis and Machine Intelligence*, v. 16, no. 9, p. 920-932.
- Kaufmann, V., 1996, Geomorphometric monitoring of active rock glaciers in the Austrian Alps, the 4th International Symposium on High Mountain Remote Sensing Cartography: Karlstad - Kiruna - Tromsø, p. 97-113.

- Kaufmann, V., and Ladstaedter, R., 2000, Spatio-temporal analysis of the dynamic behaviour of The hochebenkar rock glaciers (oetztal alps, Austria) By means of digital photogrammetric methods, 6th International Symposium on High Mountain Remote Sensing Cartography, Volume 37, Grazer Schriften der Geographie und Raumforschung, p. 119-139.
- Kaufmann, V., and Ladstädter, R., Quantitative analysis of rock glacier creep by means of digital photogrammetry using multi-temporal aerial photographs: two case studies in the Austrian Alps, *in* Proceedings Eighth international conference on permafrost, Zurich, Switzerland, 2003, Taylor & Francis p. 525-530.
- Kenyi, L. W., and Kaufman, V., Measuring rock glacier surface deformation using SAR interferometry, *in* Proceedings Eighth International Conference on Permafrost, Zurich, Balkema, 2003, Volume 1, p. 537– 541.
- Klees, R., and Massonnet, D., 1998, Deformation measurements using SAR interferometry: potential and limitations: *Geologie en Mijnbouw*, v. 77, no. 2, p. 161-176.
- Krabill, W. B., Abdalati, W., Frederick, E. B., Manizade, S. S., Martin, C. F., Sonntag, J. G., Swift, R. N., Thomas, R. H., and Yungel, J. G., 2002, Aircraft laser altimetry measurement of elevation changes of the Greenland ice sheet: technique and accuracy assessment: *Journal of Geodynamics*, v. 34, no. 3-4, p. 357-376.
- Kraus, K., 2007, *Photogrammetry: geometry from images and laser scans*, Berlin, Walter de Gruyter, XV, 459 s. p.:
- Kääb, A., 2002, Monitoring high-mountain terrain deformation from repeated air- and spaceborne optical data: examples using digital aerial imagery and ASTER data: *ISPRS Journal of Photogrammetry and Remote Sensing*, v. 57, no. 1-2, p. 39-52.
- , 2005a, Combination of SRTM3 and repeat ASTER data for deriving alpine glacier flow velocities in the Bhutan Himalaya: *Remote Sensing of Environment*, v. 94, no. 4, p. 463-474.
- , 2005b, Remote sensing of mountain glaciers and permafrost creep, Zürich, Geographisches Institut der Universität Zürich, 264 p.:
- Kääb, A., Haerberli, W., and Gudmundsson, G. H., 1997, Analysing the creep of mountain permafrost using high precision aerial photogrammetry: 25 years of monitoring Gruben Rock Glacier, *Swiss Alps: Permafrost and Periglacial Processes*, v. 8, no. 4, p. 409-426.
- Kääb, A., Haerberli, W., Huggel, C., and Paul, F., 2000, Glacier- and permafrost-related hazards in high mountains: integrative assessment in the Swiss Alps based on remote sensing and geo-information systems, *Proceedings of X Congresso Peruano de Geologia: Lima*.
- Kääb, A., Huggel, C., Fischer, L., Guex, S., Paul, F., Roer, I., Salzmann, N., Schlaefli, S., Schmutz, K., Schneider, D., Strozzi, T., and Weidmann, Y., 2005a, Remote sensing of glacier- and permafrost-related hazards in high mountains: an overview: *Nat. Hazards Earth Syst. Sci.*, v. 5, no. 4, p. 527-554.
- Kääb, A., Kaufmann, V., Ladstadter, R., and Eiken, T., 2003, Rock glacier dynamics: implications from high-resolution measurements of surface velocity fields: *Permafrost, Vols 1 and 2*, p. 501-506.
- Kääb, A., and Reichmuth, T., 2005, Advance mechanisms of rock glaciers: *Permafrost and Periglacial Processes*, v. 16, no. 2, p. 187-193.
- Kääb, A., Reynolds, J., and Haerberli, W., 2005b, Glacier and Permafrost Hazards in High Mountains, *in* Huber, U. M., Bugmann, H. K. M., and Reasoner, M. A., eds., *Global Change and Mountain Regions, Volume 23: the Netherlands*, Springer Netherlands, p. 225-234.

- Kääb, A., and Vollmer, M., 2000, Surface geometry, thickness changes and flow fields on creeping mountain permafrost: automatic extraction by digital image analysis: *Permafrost and Periglacial Processes*, v. 11, no. 4, p. 315-326.
- Leprince, S., Ayoub, F., Klingert, Y., and Avouac, J. P., Co-Registration of Optically Sensed Images and Correlation (COSI-Corr): an operational methodology for ground deformation measurements, *in Proceedings Geoscience and Remote Sensing Symposium, 2007. IGARSS 2007. IEEE International23-28 July 2007 2007a*, p. 1943-1946.
- Leprince, S., Barbot, S., Ayoub, F., and Avouac, J. P., 2007b, Automatic and Precise Orthorectification, Co-registration, and Subpixel Correlation of Satellite Images, Application to Ground Deformation Measurements: *Geoscience and Remote Sensing, IEEE Transactions on*, v. 45, no. 6, p. 1529-1558.
- Lesniak, A., and Porzycka, S., 2008, Environment monitoring using satellite radar interferometry technique (PSInSAR): *Polish Journal of Environmental Studies*, v. 17, no. 3A, p. 382-387.
- Lewis, J. P., 1995, Fast Normalized Cross-Correlation: *Vision Interface*, p. 120-123.
- Lillesand, T. M., Kiefer, R. W., and Chipman, J. W., 2008, *Remote sensing and image interpretation*, Hoboken, N.J., Wiley, XII, 756 s. p.:
- Lingua, A., Piatti, D., and Rinaudo, F., 2008, Geomorphometric monitoring of active rock glaciers in the Austrian Alps: *The International Archives of the Photogrammetry, Remote Sensing and Spatial Information Sciences*, v. XXXVII, no. B1, p. 361-366.
- Luckman, A., Murray, T., Jiskoot, H., Pritchard, H., and Strozzi, T., 2003, ERS SAR feature-tracking measurement of outlet glacier velocities on a regional scale in East Greenland: *Annals of Glaciology, Vol 36*, v. 36, p. 129-134.
- Lutes, J., DAIS: a digital airborne imaging system, *in Proceedings Pecora 15/Land Satellite Information IV/ISPRS Commission I/FIEOS2002*.
- Maurer, H., and Hauck, C., 2007, Geophysical imaging of alpine rock glaciers: *Journal of Glaciology*, v. 53, no. 180, p. 110-120.
- McCloy, K. R., 2006, *Resource management information systems: remote sensing, GIS and modelling*, Boca Raton, Fla., CRC/Taylor & Francis, 575 s. p.:
- Meisina, C., Zucca, F., Fossati, D., Ceriani, M., and Allievi, J., 2006, Ground deformation monitoring by using the Permanent Scatterers Technique: The example of the Oltrepo Pavese (Lombardia, Italy): *Engineering Geology*, v. 88, no. 3-4, p. 240-259.
- Michel, R., and Rignot, E., 1999, Flow of Glaciar Moreno, Argentina, from repeat-pass Shuttle Imaging Radar images: comparison of the phase correlation method with radar interferometry: *Journal of Glaciology*, v. 45, no. 149, p. 93-100.
- Mikhail, E. M., Bethel, J. S., and McGlone, J. C., 2001, *Introduction to modern photogrammetry*, New York, Wiley, IX, 479 s. p.:
- Moholdt, G., Hagen, J. O., Eiken, T., and Schuler, T. V., 2010, Geometric changes and mass balance of the Austfonna ice cap, Svalbard: *The Cryosphere*, v. 4, p. 21-34.
- Musil, M., Maurer, H., Green, A. G., Horstmeyer, H., Nitsche, F. O., Muhill, D. V., and Springman, S., 2002, Shallow seismic surveying of an Alpine rock glacier: *Geophysics*, v. 67, no. 6, p. 1701-1710.
- Maas, H. G., Casassa, G., Schneider, D., Schwalbe, E., and Wendt, A., 2010, Photogrammetric determination of spatio-temporal velocity fields at Glaciar San Rafael in the Northern Patagonian Icefield: *The Cryosphere Discuss.*, v. 4, no. 4, p. 2415-2432.
- Nuth, C., and Kääb, A., 2011, Co-registration and bias corrections of satellite elevation data sets for quantifying glacier thickness change: *The Cryosphere*, v. 5, no. 1, p. 271-290.
- Nye, J. F., 1952, The mechanics of glacier flow: *Journal of Glaciology*, v. 2, no. 11.

- Okutomi, M., and Kanade, T., 1990, A Locally Adaptive Window for Signal Matching: Third International Conference on Computer Vision, p. 190-199.
- Okutomi, M., and Kanade, T., 1992, A locally adaptive window for signal matching: International Journal of Computer Vision, v. 7, no. 2, p. 143-162.
- Pluim, J. P. W., Maintz, J. B. A., and Viergever, M. A., 2003, Mutual-information-based registration of medical images: a survey: Medical Imaging, IEEE Transactions on, v. 22, no. 8, p. 986-1004.
- Rignot, E., and Kanagaratnam, P., 2006, Changes in the Velocity Structure of the Greenland Ice Sheet: Science, v. 311, no. 5763, p. 986-990.
- Ritter, M., 2006, The physical environment: an introduction to physical geography, Volume 2010: 14.09.2011, <http://www4.uwsp.edu/geo/faculty/ritter/geog101/textbook/>.
- Roer, I., b, A., and Dikau, R., 2005, Rockglacier acceleration in the Turtmann valley (Swiss Alps): Probable controls: Norwegian Journal of Geography, v. 59, no. 2, p. 157-163.
- Schenk, T., 1999, Digital photogrammetry, Laurelville, Ohio, TerraScience, b. p.:
- Schmid, C., Mohr, R., and Bauckhage, C., Comparing and evaluating interest points, in Proceedings Computer Vision, 1998. Sixth International Conference on 4-7 Jan 1998 1998, p. 230-235.
- Schowengerdt, R. A., 2007, Remote sensing: models and methods for image processing, Amsterdam, Elsevier, XLI, 515 s. p.:
- Schutz, B. E., Zwally, H. J., Shuman, C. A., Hancock, D., and DiMarzio, J. P., 2005, Overview of the ICESat Mission: Geophys. Res. Lett., v. 32, no. 21, p. L21S01.
- Shroder, J. F., 1978, Dendrogeomorphological analysis of mass movement on Table Cliffs Plateau, Utah: Quaternary Research, v. 9, no. 2, p. 168-185.
- Sommerkorn, M., and Hamilton, N., 2008, Arctic Climate Impact Science— an update since ACIA: Oslo, WWF International Arctic Programme, p. 124.
- Strozzi, T., Kääb, A., and Frauenfelder, R., 2004, Detecting and quantifying mountain permafrost creep from in situ inventory, space-borne radar interferometry and airborne digital photogrammetry: International Journal of Remote Sensing, v. 25, no. 15, p. 2919-2931.
- Strozzi, T., Luckman, A., Murray, T., Wegmuller, U., and Werner, C. L., 2002, Glacier motion estimation using SAR offset-tracking procedures: IEEE Transactions on Geoscience and Remote Sensing, v. 40, no. 11, p. 2384-2391.
- Wangensteen, B., Tønsberg, O. M., Kääb, A., Eiken, T., and Hagen, J. O., 2006, Surface Elevation Change and High Resolution Surface Velocities for Advancing Outlets of Jostedalbreen: Geografiska Annaler: Series A, Physical Geography, v. 88, no. 1, p. 55-74.
- Wehr, A., and Lohr, U., 1999, Airborne laser scanning--an introduction and overview: ISPRS Journal of Photogrammetry and Remote Sensing, v. 54, no. 2-3, p. 68-82.
- Whillans, I. M., and Tseng, Y. H., 1995, Automatic tracking of crevasses on satellite images: Cold Regions Science and Technology, v. 23, no. 2, p. 201-214.
- Willis, I. C., 1995, Intra-annual variations in glacier motion: a review: Progress in Physical Geography, v. 19, no. 1, p. 61-106.
- Willmott, C. J., and Matsuura, K., 2005, Advantages of the mean absolute error (MAE) over the root mean square error (RMSE) in assessing average model performance: Climate Research, v. 30, no. 1, p. 79-82.
- Woodcock, C. E., and Strahler, A. H., 1987, The Factor of Scale in Remote Sensing: Remote Sensing of Environment, v. 21, no. 3, p. 311-332.
- Yamaguchi, Y., Tanaka, S., Odajima, T., Kamai, T., and Tsuchida, S., 2003, Detection of a landslide movement as geometric misregistration in image matching of SPOT HRV

data of two different dates: *International Journal of Remote Sensing*, v. 24, no. 18, p. 3523 - 3534.

Zhao, F., Huang, Q. M., and Gao, W., Image matching by normalized cross-correlation, *in* Proceedings 31st IEEE International Conference on Acoustics, Speech and Signal Processing, Toulouse, FRANCE, May 14-19 2006, p. 1977-1980.

Zitová, B., and Flusser, J., 2003, Image registration methods: a survey: *Image and Vision Computing*, v. 21, no. 11, p. 977-1000.





# **Part II Journal Publications**



# I. Sub-pixel precision image matching for measuring surface displacements on mass movements using normalized cross-correlation<sup>1</sup>

Misganu DEBELLA-GILO<sup>a</sup> and Andreas KÄÄB<sup>b</sup>

<sup>a,b</sup>Institute of Geosciences, University of Oslo, P. O. Box 1047, Oslo, Norway

<sup>a</sup>[m.d.gilo@geo.uio.no](mailto:m.d.gilo@geo.uio.no) (corresponding author)

**ABSTRACT.** This study evaluates the performance of two fundamentally different approaches to achieve sub-pixel precision of normalized cross-correlation when measuring surface displacements on mass movements from repeat optical images. In the first approach, image intensities are interpolated to a desired sub-pixel resolution using a bi-cubic interpolation scheme *prior* to the actual displacement matching. In the second approach, the image pairs are correlated at the original image resolution and the peaks of the correlation coefficient surface are then located at the desired sub-pixel resolution using three techniques, namely bi-cubic interpolation, parabola-fitting and Gaussian-fitting. Both principal approaches are applied to three typical mass movement types: rockglacier creep, glacier flow and land sliding. In addition, the influence of pixel resolution on the accuracies of displacement measurement using image matching is evaluated using repeat images resampled to different spatial resolutions. Our results show that bi-cubic interpolation of image intensity performs best followed by bi-cubic interpolation of the correlation surface. Both Gaussian and parabolic peak locating turn out less accurate. By increasing the spatial resolution (i.e. reducing the ground pixel size) of the matched images by 2 to 16 times using intensity interpolation, 40% to 80% reduction in mean error in reference to the same resolution original image could be achieved. The study also quantifies how the mean error, the random error, the proportion of mismatches and the proportion of undetected movements increase with increasing ground pixel size (i.e. decreasing spatial resolution) for all of the three mass movement examples investigated.

**Keywords:** Normalized cross-correlation, Sub-pixel precision, Image matching, Displacement measurement, Rockglacier, Glacier, Rock slide

---

<sup>1</sup> *Remote Sensing of Environment* 115(1): 130-142

## I.1. Introduction

Present climatic change shifts geomorphodynamic equilibriums and intensifies related mass movement processes such as landslides and permafrost creep (Haeberli and Beniston 1998; Rebetz et al. 1997). Extension and intensification of human activities in areas affected by such mass movements increase the probability of connected adverse impacts like natural hazards or building stability problems. A growing number of remote sensing opportunities exist to monitor such mass movements. The increasing number of available collections of multi-temporal space-borne, air-borne and terrestrial images, and the improvements in remote sensing and image processing in general significantly enhance the potential for applying matching techniques to detect and quantify Earth surface mass movements from repeat remotely sensed data. These needs and developments call for continued efforts to improve terrain displacement matching methods based on repeat images for a large number of applications in Earth sciences.

Image matching is a group of techniques of finding corresponding features or image patches in two or more images taken of the same scene from different viewing positions, at different times and/or using different sensors. Image matching is used for a large variety of applications such as image (co-) registration, stereo parallax matching for generation of digital elevation models, particle image velocimetry (PIV), or displacement measurements (Brown 1992; Westerweel 1993; Zitová and Flusser 2003).

The group of area-based matching techniques is the most widely used method due to its relative simplicity (Zitová and Flusser 2003). Cross-correlation, particularly its normalized form which accounts for brightness and contrast in image sequences, is the most widely used similarity measure of this method due to its reliability and simplicity (Lewis 1995). The normalized cross-correlation (NCC) algorithm has been used to investigate Earth mass movements such as glacier flow, rockglacier (used here as one word after Barsch (1996)) creep and land sliding in many empirical studies (e.g. Haug et al. 2010; Kaufmann and Ladstädter 2003; Käab 2005; Käab and Vollmer 2000; Quincey et al. 2005; Scambos et al. 1992; Scherler et al. 2008; Skvarca et al. 2003; Taylor et al. 2008; Wangensteen et al. 2006).

Although NCC has been documented to be simple and reliable, a number of drawbacks have been reported as well (Lewis 1995; Scambos et al. 1992; Zhao et al. 2006). Firstly, NCC is sensitive to noise in the images. Secondly, NCC is sensitive to significant scale, rotation or shearing differences between the images to be correlated. Thirdly, for the

measurement to be reliable the displacement has to be greater than the mean error of the image (co-)registration. Fourthly, the precision of NCC is, in principle, limited to one pixel, and thus varies with the pixel size of the image data used.

Pixel-level accuracy might be satisfactory depending on the spatial resolution of the imagery available and the type of process being investigated. Improving NCC precision, however, improves displacement accuracy twofold: by reducing the image co-registration error and by improving the matching accuracy directly. To achieve sub-pixel precision in NCC, two approaches can be used. The first option is to resample the image intensity to a higher spatial resolution through interpolation. This approach has been applied in stereo matching (e.g. Szeliski and Scharstein 2002) and in displacement measurement of Earth surface movements (e.g. Crippen and Blom 1991; Yamaguchi et al. 2003). The second option is to interpolate the cross-correlation surface after the matching process to a higher spatial resolution in order to locate the correlation peak with sub-pixel precision. This approach has been applied in image registration (e.g. Althof et al. 1997; Scambos et al. 1992), in mechanics to measure the velocity of particles (e.g. Westerweel 1993; Willert and Gharib 1991), in motion tracking to measure displacements of landslide (e.g. Delacourt et al. 2004; Yamaguchi et al. 2003) and glaciers (e.g. Scambos et al. 1992). There are also area-based spatial domain methods that are intrinsically capable of sub-pixel precision such as the least squares matching, which is more often used in stereoscopic DEM generation and image registration. Least square matching is known for its capability to deal with scaling and rotation and has occasionally been used in the displacement measurement of mass movements (e.g. Kaufmann and Ladstädter 2003; Whillans and Tseng 1995). Other techniques that are used in mass movement analysis for achieving sub-pixel precision are the Fourier-based phase matching and gradient-based matching (e.g. Haug et al. 2010; Leprince et al. 2007; Taylor et al. 2008). Preprocessing steps such as noise filtering and post-processing steps such as filtering of displacement vectors by averaging are also able to improve the precision and accuracies of displacement estimates (Kääb and Vollmer 2000; Zitová and Flusser 2003).

The present study focuses exclusively on mass movement analysis by NCC due to the wide-spread use of this technique, and its simplicity and reliability. Thus, we do not consider the above methods that are intrinsically capable of sub-pixel precision. Further, we concentrate on the intensity interpolation and the correlation interpolation approaches because both are generic and independent of image resolution. There is no study available that rigorously compares the relative performance of the two approaches when measuring the displacement of mass movements from repeat images.

Mass movement, in the context of our study, refers to the down slope movement of Earth materials including rocks, glacier ice and debris triggered by agents such as gravity, water, and tectonic activity (Ritter 2006). Many Earth surface mass movements such as landslide, glacier flow, and rockglacier creep are characterized by displacement rates of the same order of magnitude as the spatial resolution of the space-borne or air-borne imagery typically available for their measurement. Such masses usually move with rates in the order of several centimeters to some hundred meters per year. Sub-pixel precision of image matching algorithms, here NCC, therefore has a large potential to improve the signal-to-noise ratio of the measurements. In other words, improving the precision (i.e. level of detail of the measurement) of displacement estimation contributes to the improvement of accuracy (i.e. the certainty of the estimation).

Using NCC as an example, this study compares the accuracies of two fundamentally different approaches to reaching sub-pixel precision in mass movement measurement from repeat remotely sensed images, namely intensity interpolation and correlation interpolation. The study specifically aims at (i) quantifying the effects of pixel size (i.e. ground area represented by a pixel) on the accuracy of displacement matching, (ii) quantifying and comparing the performances of different sub-pixel precision algorithms, and (iii) identifying the gains and limit of the sub-pixel precision algorithms.

## **I.2. Methods**

### **I.2.1. Image data and resolution pyramid**

For this study, three different types of mass movements were selected based on their frequency in high mountain areas: land sliding, glacier flow, and rockglacier creep. Three temporal pairs of air photos each covering ground areas of 0.35 km<sup>2</sup>, 3 km<sup>2</sup> and 0.25 km<sup>2</sup> respectively were used. These images were orthorectified *prior* to displacement matching. Details are given in section 3.

Better understanding of the influence of spatial resolution on the accuracy of image matching requires images of the same area taken at the same time, under the same flight and ground conditions, but using sensors with different spatial resolutions. Such conditions are not easily met. Instead, different optical systems were simulated by down-sampling the original high-resolution aerial orthoimages to five levels of lower spatial resolution (Table I-1). One

resolution pyramid with six levels each was finally obtained for each of the two repeat images of each of the three mass movements as shown in Fig. I-1. The resolution pyramids are thus not the same as the Gaussian or Laplacian image pyramids often used in multi-scale image analysis or in image visualization. The down-sampling factors here are chosen for convenience. The down-sampling was performed using the MATLAB module ‘*imresize*’ with the most efficient and reliable algorithm for this purpose, namely bi-cubic convolution. The algorithm assigns the weighted average of pixel values in the nearest 4-by-4 neighborhood (Keys 1981). Although this resampling process is slightly different from the pure signal averaging happening in the instantaneous field of view of a sensor detector cell, we decided to choose bi-cubic convolution because most images used for matching will in practice have undergone such interpolation during image correction and Preprocessing steps, such as orthorectification (Toutin 2004).

Additionally, one resolution pyramid was created from one of the original glacier images after applying a two-dimensional translation of 15 pixels (9 pixels in the x-direction and 12 pixels in the y-direction). This translation becomes a non-integer pixel displacement in the lower resolution resampled images. Since this pair was made from just one original image and the displacement applied was only translation, the pair serves as a control data set as it is free of noise from temporal surface changes, changes in imaging condition, registration errors and geometric distortions.

Table I-1. Movement process types, spatial resolution of the original images and resolution pyramids used in this study, and examples of satellite sensors simulated by this image resolution resampling.

<b>Mass movement type</b>	<b>Resampling factor</b>	<b>Ground pixel size (m)</b>	<b>Examples of optical satellite systems simulated</b>
<b>Rockglacier and landslide</b>	original	0.2	
	2	0.4	IKONOS, WorldView-1
	4	0.8	IKONOS, QuickBird
	8	1.6	QuickBird
	16	3.2	SPOT 5 panchromatic, ALOS(PRISM)
	32	6.4	SPOT 5 panchromatic
<b>Glacier</b>	original	0.5	
	2	1	IKONOS
	4	2	IKONOS, QuickBird, SPOT 5 panchromatic, ALOS (PRISM)
	8	4	SPOT 5 panchromatic
	16	8	SPOT panchromatic
	32	16	ASTER, Landsat 7 panchromatic

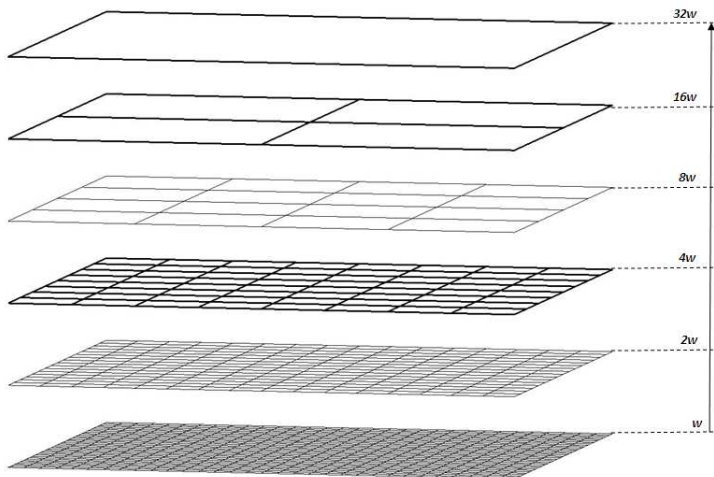


Fig. I-1 Setup of the image resolution pyramid,  $w$  being the ground pixel size of the original image

### I.2.2. Normalized cross-correlation

The normalized cross-correlation (NCC) algorithm is a similarity measure that is used in image matching to measure the similarity between matching entities in one image and their corresponding entities in the other image. The algorithm was developed based on the concept of distance measure but second normalized to account for the differences in brightness and contrast (Lewis 1995; Vosselman et al. 2004). An image  $I_1$  over an area is taken at time  $T_1$  and another image  $I_2$  over the same area at time  $T_2$  (Fig. I-2). The term  $f(x, y)$  stands for the intensity values of a squared area that is a subset of  $I_1$ ,  $t(x-u, y-v)$  for the intensity values in a squared area in  $I_2$  of the same size as  $f(x, y)$ , where  $u$  and  $v$  are integer pixel offsets in  $x$ - and  $y$ -direction respectively.  $f(x, y)$  is further called reference template and  $t(x-u, y-v)$  is called search template. The size of the template is chosen to be large enough to maximize the signal-to-noise ratio and small enough to minimize velocity gradients (Kanade and Okutomi 1991). The search area size is chosen to be large enough to include the farthest moving template and small enough to limit the computational cost of the matching. To find the corresponding



square to  $f(x, y)$  in  $I_2$ , the normalized cross correlation coefficient ( $\rho$ ) between  $f(x, y)$  and corresponding window in  $I_2$ ,  $t(x-u, y-v)$ , is computed. The NCC coefficient  $\rho$  is computed as given in Eq. (I-1) and is assigned to the central pixel of the template (Lewis 1995; Vosselman et al. 2004). The computation continues by moving  $t$  in every iteration by one pixel until the entire search window is covered. After finishing the computation, the pixel  $(x_0, y_0)$  in the search window with the highest correlation coefficient is considered as the likely best match for the central pixel of the reference template. The Euclidean distance between the coordinates of the reference point  $[x, y]$  and the matching point  $[x_0, y_0]$  is considered as the horizontal displacement magnitude,  $d(x, y)$ .

$$\rho(x, y) = \frac{\sum_{x,y}(f(x,y)-\bar{f})(t(x-u,y-v)-\bar{t})}{(\sum_{x,y}(f(x,y)-\bar{f})^2 \sum_{x,y}(t(x-u,y-v)-\bar{t})^2)^{1/2}} \quad \text{I-1}$$

$\bar{f}$  is the mean of the intensities in the reference template  $f(x, y)$  and  $\bar{t}$  is the mean of the intensities in the search template  $t(x-u, y-v)$ . The values of  $\rho$  range between -1 (when the matching entities are inverses of each other) and 1 (when the matching entities are exactly the same).  $\rho=0$  is an indication of no relationship between the matching entities. Even if there is no truly corresponding entity in the search image, there will always be some peak correlation coefficient. Therefore, it is necessary to decide a threshold for  $\rho$  below which the match is rejected.

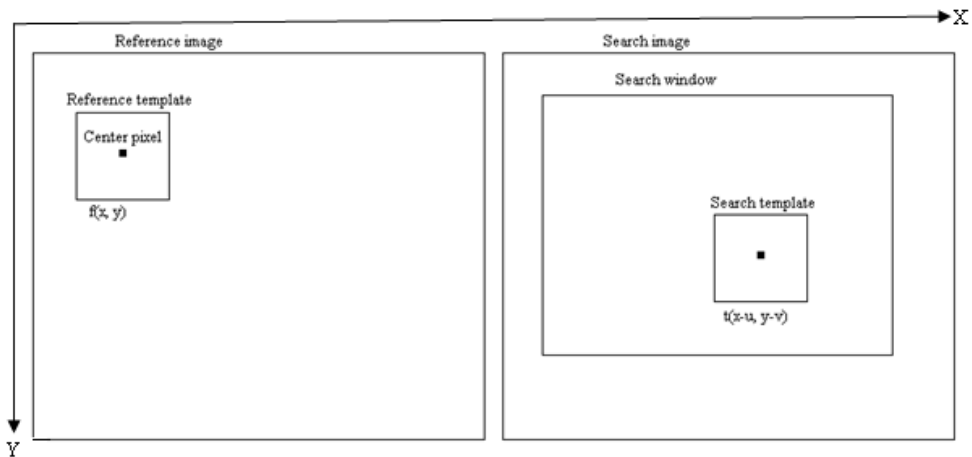


Fig. I-2. Scheme of the image pairs together with the reference template, central pixel, search template and the search window

### **I.2.3. Matching and displacement measurement at different pixel sizes**

First, the original high-resolution orthoimages (before resampling) were matched using the NCC algorithm at pixel-precision to determine the matching positions and compute the horizontal displacement magnitude and direction. Mismatches that were characterized by low peak correlation coefficients, very large displacements in relation to their neighboring templates, or displacements showing distinct upslope movement were removed manually. Since manual removal of the mismatches is heuristic and influences the final analysis, the proportion of mismatches is counted and reported separately as an indicator of performance. Additionally, displacements less than the mean orthorectification error were removed as they are not reliably distinct from the error. The orthorectification error (offset between the images) was computed by matching stable grounds. The computation revealed that a maximum of 1 pixel offset exists in each dimension at the resolution of the original orthoimages. In orthoimages, positional errors increase from the projection centre proportional to the magnitude of the vertical errors in the digital elevation model used for the orthoprojection. All our three mass movements are located near the centers of the original air photos and the stable grounds are located towards the edges. Therefore, the here-estimated offset error is assumed to exceed the actual positional errors on the mass movements. The matching results on the original full-resolution images were considered as reference for all other measurements throughout the resolution pyramid pairs.

Matching and displacement measurement were in a next step performed on all resolution levels of the resolution pyramid pairs for all locations used also above for the original images. The absolute sizes and positions of the reference templates and the search windows were kept constant in ground coordinates throughout the resolution pyramid by adjusting the number of pixels according to the resolution. This procedure was in order to avoid variations in signal content as a result of inclusion or exclusion of ground features. In other words, the ground area covered by the templates remained the same when the respective image resolution changed. The size of the template was kept at around 26 m and 65 m for the originally 0.2 m and 0.5 m resolution images, respectively. The size of the search window was kept at around 102 m and 265 m for the originally 0.2 m and 0.5 m resolution images, respectively, so that it certainly included the expected maximum surface displacement.

The performance of the matching at different resolutions was evaluated by comparing the obtained matching position to those obtained from the image pairs at original full

resolutions. Often, the accuracy of displacement measurements using cross-correlation is evaluated by comparing the estimated displacement magnitude ( $d_i$ ) to the actual displacement magnitude ( $d_0$ ). In this study, this is found to be misleading as the displacement direction is equally important to assess the matching accuracy. Therefore, instead of using the difference in displacement magnitude as an indicator of accuracy, we use the shift in matching position (Fig. I-3). The matching positions obtained during the correlation of the original images [ $x_0$ ,  $y_0$ ] are considered as references. All the matching positions at the different coarser or back-interpolated (see next Section) resolutions [ $x_i$ ,  $y_i$ ] are compared to these reference positions. The magnitude of this deviation ( $dev$ ) is here used as measure for the performance of the image and algorithm used (Eq. I-2).

$$dev = \sqrt{(x_i - x_0)^2 + (y_i - y_0)^2} \quad \text{I-2}$$

The image and algorithm performance was evaluated based on three types of errors known in image matching, namely mismatches (spurious matches), mean bias (here mean deviation) and the root mean square (RMS) error (Huang et al. 1997; Lourenco and Krothapalli 1995). Additionally, the proportion of undetected movements was also added as a measure of the influence of pixel size on the success of displacement measurements. The mismatches and the undetected moving entities were counted globally while the magnitudes of the mean deviation and the RMS were computed locally (Eqs. I-3 and I-4). Here,  $n$  stands for the total number of validly matched entities and  $i$  stands for the individual validly matched entity.

The mean deviation ( $\overline{dev}$ ) is given as:

$$\overline{dev} = \frac{\sum_{i=1}^n dev_i}{n} \quad \text{I-3}$$

And the RMS ( $\sigma_{dev}$ ) is given as:

$$\sigma_{dev} = \sqrt{\frac{\sum_{i=1}^n (dev_i - \overline{dev})^2}{n-1}} \quad \text{I-4}$$

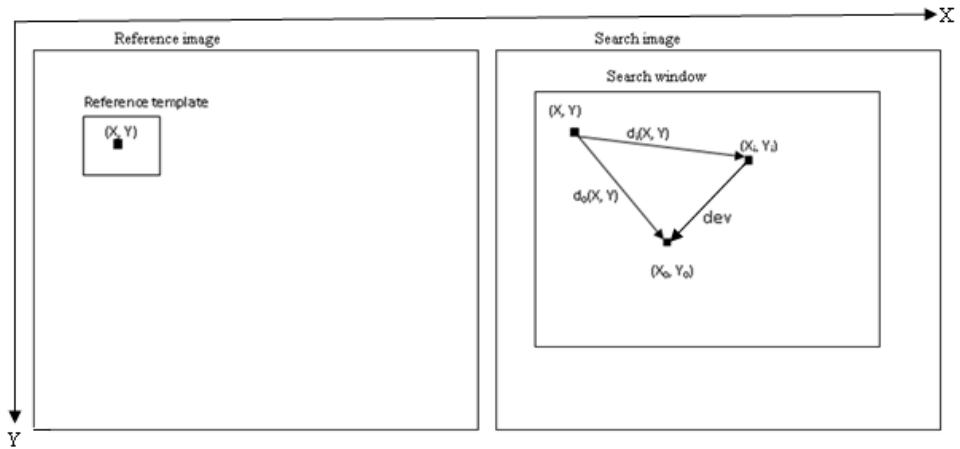


Fig. I-3. Scheme of the matching position deviations and the difference in displacement

### I.2.3. The sub-pixel precision approaches

#### I.2.3.1. Intensity interpolation

The issue of sub-pixel estimation appears because the images available are often not at the optimal resolution for precise quantification of movement. Signals in image pixels are created by integrating spatially continuous signals over the area covered by the pixel. If the continuous signal existed, one could choose the interval at which the integration is done, i.e. the pixel resolution, as long as the signals are detectable. However, since such integration of continuous signals is done by the imaging sensor during the image acquisition, the continuous signal is no longer available for later analysis. One alternative is thus to reconstruct the continuous signal from the spatially discrete images. Full reconstruction is only ideally possible, though. Therefore, the image itself is interpolated to the desired pixel resolution using certain interpolation schemes, preferably ones that can effectively reduce aliasing.

In this study, the coarse resolution images within the above-computed resolution pyramids were back-interpolated to different finer resolutions using the MATLAB-based '*imresize*' module with the bi-cubic interpolation scheme (Fig. I-4 left). The bi-cubic algorithm is an appropriate choice for accuracy and efficiency in comparison with other algorithms (Keys 1981; Meijering and Unser 2003). After such back-interpolation, the NCC algorithm with Eq. (1) was applied using the same templates and search windows as used in the original reference image pairs. The interpolation is done on the fly for each reference template and search window, and not for the entire image before the matching process to cope

with MATLAB's memory restrictions. Even in this approach when the resampling factor is doubled, the computation time increases about four times.

### 1.2.3.2. Similarity interpolation

The similarity measure used in this study, i.e. the NCC coefficient, produces pixel-level peak locations. However, that location might not be the exact position of the matching entity. To find the sub-pixel position from the discrete NCC coefficients, one can either interpolate the cross-correlation surface to a higher resolution using two dimensional interpolation algorithms or fit a two-dimensional analytical function to the correlation surface around the peak.

**Correlation interpolation using bi-cubic convolution.** The correlation surface around the peak is resampled to the desired higher resolution. A two-dimensional cubic convolution of the correlation coefficients is then applied to the resampled grid using the MATLAB module '*interp2*'. The bi-cubic convolution takes the weighted average of the nearest 16 (4-by-4) pixels. The peak is then relocated at the new resolution.

**Curve fitting.** As an alternative to peak interpolation, one can also create a continuous function that optimally fits the correlation coefficient data and compute the precise location of the peak from the maximum of the function. The challenge is that no single function can usually perfectly describe the cross-correlation surface. However, the fact that the correlation surface around its peak often approaches a bell shape can be exploited. Therefore, two dimensional polynomial functions can approximate the surface. A number of models have been tested in empirical and theoretical researches, particularly in particle image velocimetry (PIV), though with varying successes (Nobach and Honkanen 2005; Westerweel 1993; Willert and Gharib 1991). Parabola and Gaussian fitting are tested here for mass movement analysis, as these have shown successes in other areas, especially in PIV.

In parabola fitting, the shape of the correlation surface is assumed to fit two orthogonal parabolic curves. The location of the 'actual' peak is computed by independently fitting one dimensional quadratic function and computing the location of the peak (Nobach and Honkanen 2005; Shimizu and Okutomi 2002; Westerweel 1993). Assume we have computed the pixel level (integer) position of the peak as  $[x_0, y_0]$ . This pixel has two neighbors in each of the two orthogonal directions:  $(x_0-1)$  and  $(x_0+1)$  in the x-direction and  $(y_0-1)$  and  $(y_0+1)$  in the y-direction. To find the sub-pixel peak position in each direction  $(x_0+\Delta x, y_0+\Delta y)$ , we define a parabolic curve that connects the three points of that direction

and compute the position where the curve attains its maximum. Equations I-5 and I-6 compute the non-integer location of the peak in the x- and y-directions which will then be added to the pixel (integer).

$$\Delta X = \frac{\rho(X_0-1, Y_0) - \rho(X_0+1, Y_0)}{2\rho(X_0-1, Y_0) - 4\rho(X_0, Y_0) + 2\rho(X_0+1, Y_0)} \quad \text{I-5}$$

$$\Delta Y = \frac{\rho(X_0, Y_0-1) - \rho(X_0, Y_0+1)}{2\rho(X_0, Y_0-1) - 4\rho(X_0, Y_0) + 2\rho(X_0, Y_0+1)} \quad \text{I-6}$$

Likewise, in Gaussian fitting, the bell shape of the correlation surface is assumed to fit a 2D Gaussian function (Nobach and Honkanen 2005; Westerweel 1993; Willert and Gharib 1991). It is assumed that the two dimensions are separable and orthogonal. Thus, the sub-pixel peak location is calculated separately for the two directions by fitting a second-order polynomial to the logarithm of the maximum sample and the direct neighbors (Eqs. I-7 and I-8).

$$\Delta X = \frac{\ln(\rho(X_0-1, Y_0)) - \ln(\rho(X_0+1, Y_0))}{2\ln(\rho(X_0+1, Y_0)) - 4\ln(\rho(X_0, Y_0)) + 2\ln(\rho(X_0-1, Y_0))} \quad \text{I-7}$$

$$\Delta Y = \frac{\ln(\rho(X_0, Y_0-1)) - \ln(\rho(X_0, Y_0+1))}{2\ln(\rho(X_0, Y_0+1)) - 4\ln(\rho(X_0, Y_0)) + 2\ln(\rho(X_0, Y_0-1))} \quad \text{I-8}$$

#### **I.2.4. Evaluation of different levels of sub-pixel detail**

Section 2.4 evaluates which sub-pixel approach performs best in improving the precision and accuracy of NCC-based image matching. It is also important to know how far sub-pixel interpolation of coarse resolution image intensities or the correlation surface is able to substitute pixel-level matching of images of the corresponding but original resolution, as well as the sub-pixel detail at which the interpolation to achieve sub-pixel precision can no longer sufficiently substitute image of that resolution. The sub-pixel precision matching is thus computed at different levels of the resolution pyramid and its performance is evaluated in reference to the pixel-level matching of images with the same but original resolution. This procedure becomes clearer with an example: suppose we want to know the performance of sub-pixel precision matching at the level of half a pixel. This can be achieved by taking an image of, for instance, 8 m resolution, computing the sub-pixel precision matching to 4 m and

comparing the latter sub-pixel performance to the performance of pixel-level matching of an image with 4 m original resolution. Alternatively, one can take a 4 m resolution image, compute its sub-pixel resolution matching to 2 m and compare the performance of the latter in relation to a 2 m resolution original image. In our study, this procedure is iterated for the entire pre-processed resolution pyramid and all resolution steps included in it, not just the level-factor 2 exemplified here (Fig. I-4 right).

Equation I-3 was used to evaluate the deviation between the sub-pixel matching and the pixel-level matching at corresponding image resolutions. This time, the reference matching position  $[x_0, y_0]$  is the matching position obtained for the same template by using a pixel-level matching of an image pair of a resolution equal to the resolution to which the sub-pixel algorithm is conducted. If the sub-pixel matching between two coarse images exactly substitutes pixel-level matching of images with corresponding fine resolution, there will be no deviation between the two matching positions.

In addition to the performance evaluation parameter  $dev$  explained above, the proportion by which each error term of the pixel-level precision was reduced by a sub-pixel algorithm was used as an alternative indicator for the accuracy improvement. For example, if an algorithm  $i$  was used, its performance in reducing the mean deviation from the pixel-level algorithm mean deviation is given as in Eq. (I-9).

$$per_i = \frac{(\overline{dev}_i - \overline{dev}_p) * 100}{\overline{dev}_p} \quad \text{I-9}$$

Here,  $per_i$  is the percentage reduced mean bias when sub-pixel algorithm  $i$  is used,  $\overline{dev}_i$  is the mean bias of that algorithm, and  $\overline{dev}_p$  is the mean deviation of the pixel-level NCC algorithm.

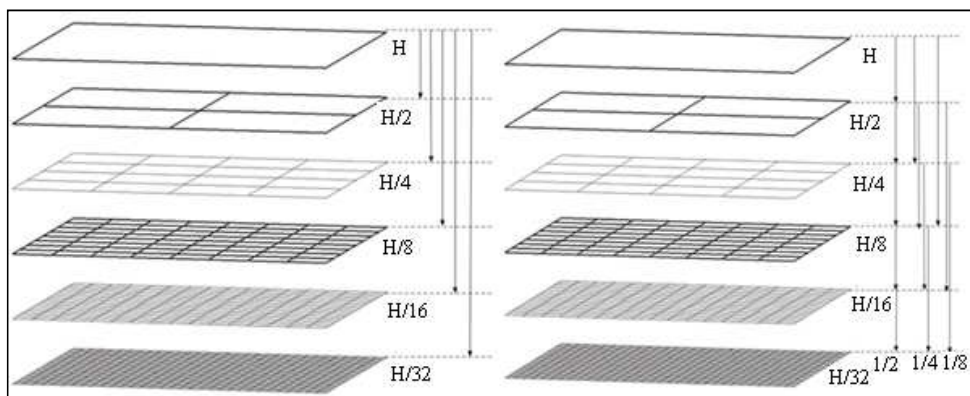


Fig. I-4. Schematic setup of intensity and correlation interpolation of the coarsest resolution images to different sub-pixel details (left) with the different possible alternatives of assessing

sub-pixel performance (right).  $H$  stands for the ground pixel size of the coarsest resolution images

### **I.3. Test sites**

As an example for glacier flow, we use the glacier Ghiacciaio del Belvedere. It is located below the Monte Rosa peak, above Macugnaga and the Anzasca valley of the Italian Alps (approx.  $7^{\circ}54'39''$  E,  $45^{\circ}54'39''$  N). This glacier has recently become known for its surge-type movement (Haerberli et al. 2000; Käab et al. 2004). It is a very dynamic glacier with a history of flooding and hazardous incidences. Since the glacier was at the time of photography very dynamic with high surface speeds, the images chosen for the present study were taken on 6 September and 11 October 2001 with a temporal baseline of around one month and an orthoimage pixel resolution of 0.5 m. More details on the images and the glacier can be found in Käab et al. (2005).

Rockglaciers consist of permanently frozen debris that slowly deforms down slope under gravity. The rockglacier chosen as test site for this study is located in the Muragl valley of the Upper Engadine area of the Swiss Alps (approx.  $9^{\circ}55'30''$  E,  $46^{\circ}30'15''$  N). It has been under investigation for decades using technologies such as photogrammetry, geodesy and geophysics to understand the mechanics of the rockglacier (Käab 2002; Käab and Vollmer 2000). The previous studies showed maximum creep speeds of up to  $0.5 \text{ m a}^{-1}$ . The orthoimages used in the present study were based on aerial images taken on 7 September 1981 and 23 August 1994 with 13 years of temporal baseline and 0.2 m of spatial resolution.

The Aletsch rockslide, used here as an example for a slow landslide, is located near the tongue of the Aletsch Glacier, Canton of Valais, Swiss Alps (approx.  $8^{\circ}01'28''$  E,  $46^{\circ}24'11''$  N). The driving force behind the rockslide is the continuous retreat of the Aletsch Glacier since approximately 1850 causing debuttrressing of the adjacent slopes (Käab 2002; Käab et al. 2005). A study that investigated the velocity of the rockslide between 1976 and 1995 showed that the rock masses have moved up to 2 m on average over 19 years (Käab 2002). The orthoimage pair used in the present study is based on air photos taken on 6 September 1976 and 5 September 2006 with 30 years temporal baseline and 0.2 m spatial resolution.



## I.4. Results

### I.4.1. Displacement vectors of the three different mass movements

Table I-2 summarizes displacement statistics for the three mass movements investigated. The results were produced from the analyses of the original orthoimages after filtering all the mismatches. One can see that the glacier moves fast as compared to the rockglacier and the even slower moving rockslide. Fig. I-5 to Fig. I-7 present the displacement vectors of the three mass movements systematically sampled at 128 pixels in both dimensions. Image matching showed that also the stable ground in the scene show non-zero displacements due to the presence of systematic image (co-)registration errors. However, after filtering of the vectors based on the estimated overall image registration error of one pixel, after thresholding of the correlation coefficients (0.65 for the rockglacier, 0.6 for the glacier and 0.45 for the landslide) and after excluding upslope movements, only the remaining vectors presented in the Figs. are considered to be valid and useful as reference.

Table I-2. Summary statistics for the displacement magnitudes and average horizontal speed of the mass movements and the translation-only control image as estimated from the matching of the original full-resolution orthoimages

<b>Mass movement</b>	<b>Temporal baseline</b>	<b>Mean displacement (m)</b>	<b>Maximum displacement (m)</b>	<b>Standard deviation of displacement (m)</b>	<b>Maximum speed (ma<sup>-1</sup>)</b>
<b>Aletsch rockslide</b>	30 years	1.5	4.2	0.45	0.14
<b>Muragl rock glacier</b>	13 years	2.4	5.8	1.20	0.45
<b>Ghiacciaio del Belvedere glacier</b>	1 month	12.22	18.83	5.0	226
<b>Control (translation only)</b>		7.50	7.50	0	7.50

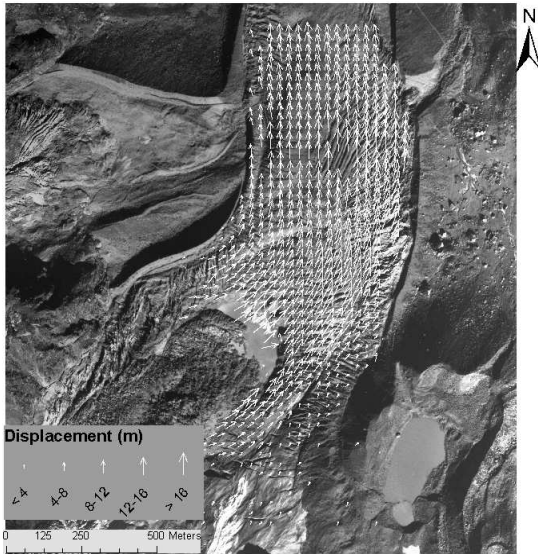


Fig. I-5. Displacement vectors on the Ghiacciaio del Belvedere (Sept. – Oct. 2001) as estimated by matching the original orthoimages and systematically sampled at 128 pixels interval in each dimension. The image displayed is from Oct. 2001.

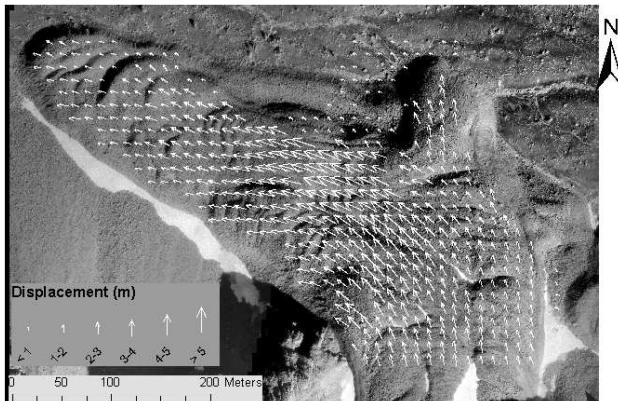


Fig. I-6. Displacement vectors on the Muragl rockglacier (1981-1994) as estimated by matching the original orthoimages and systematically sampled at 128 pixels interval in each dimension. The image displayed is from 1992.

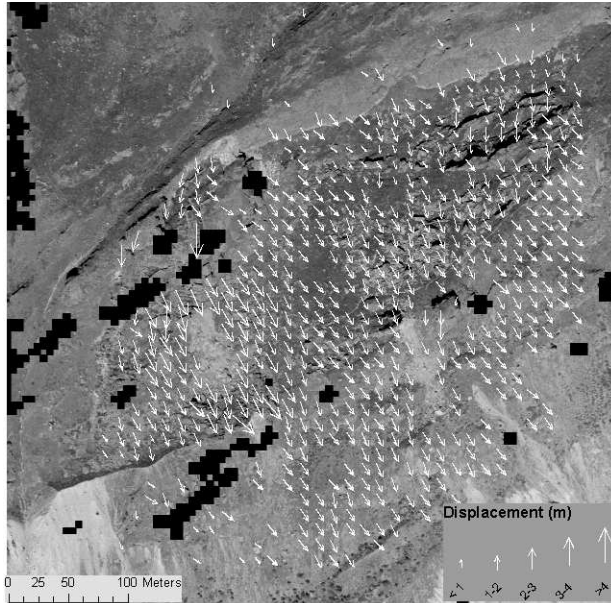


Fig. I-7. Displacement vectors on the Aletsch rockslides (1976 – 2006) as estimated by matching the original orthoimages and systematically sampled at 128 pixels interval in each dimension. The image displayed is from 2006. Aletsch Glacier is to the lower right.

#### I.4.2. Pixel resolution and matching accuracy

As expected, Fig. I-8 (A) shows for all the three mass movement types that, as the pixel size increases, the mean deviation ( $\overline{dev}$ ) also increases. There is no observable difference among the three mass movements on this type of error. The control matching shows that the mean deviation increases linearly with the factor by which the pixel size increases. In fact, the mean deviation is about half a pixel at every resolution, and similar for the real mass movement images. However, at larger pixel sizes the deviations for the real mass movements tend to be lower than a linear increase between pixel size and mean deviation, as opposed to that of the control image set which maintains the linear relationship.

The random error (RMS) shows a similar pattern except that it is very low at small pixel sizes (Fig. I-8 B). The trend in RMS for the landslide appears to be higher than for the other two sites, with that for the glacier being the lowest. The control does not have any random error until the pixel size is increased by the factor of 8.

The proportion of mismatches (Fig. I-8 C) dramatically increases with increasing pixel size. There appear to be fewer mismatches for the glacier compared to the other mass

movement types for the same metric pixel resolution. In the case of the control set, there was no mismatch observed until the pixel size was increased by the factor of 8.

The proportion of undetected moving templates also increases with pixel size (Fig. I-8 D). There seems to be no difference between the rockglacier and the landslide, but for the glacier the proportion is lower at comparable resolutions. Movements are undetected when the pixel size is greater than the displacement. That can practically be observed in the case of the control which has a uniform translation of 7.5 m over the whole image. All of the movements were detected as long as the pixel resolution was kept less than 8 m. However, as soon as the pixel resolution became 16 m, about 50% of the moving entities were not detected. In the case of the three mass movements, undetected movements were first observed after the pixel size was doubled. This is due to the existence of slow movements in all scenes that could be missed in resolution pyramid levels with comparably fine resolution. At a pixel resolution of 6.4 m approximately 35% of the original landslide and rockglacier movements and 65% of the original glacier movements could be detected.

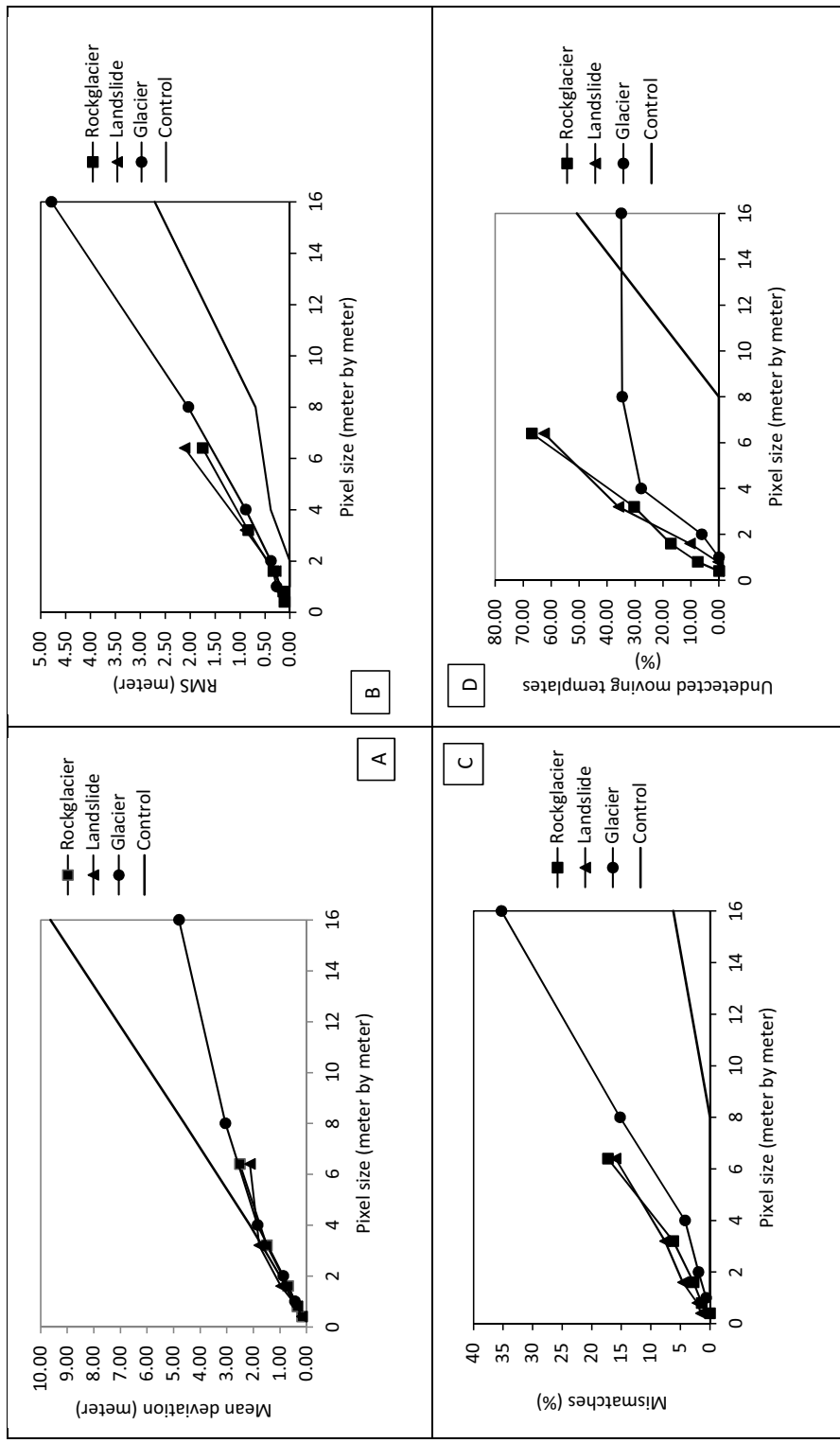


Fig. 1-8. Mean deviation (A), RMS (B), percentage mismatches (C) and percentage undetected moving templates (D) for the three mass movement types and the translation-only control set for varying pixel resolutions.

#### I.4.4. Accuracies of the sub-pixel precision algorithms

In this section we present the results of the test described in Section 2.4. Fig. I-9 and Fig. I-12 depict the mean deviation  $\overline{dev}$  of the matching positions against the sub-pixel precisions of each of the algorithms for the control set and the three mass movements respectively. The magnitudes (Fig. I-12) are created by averaging the values obtained for the three mass movement types as the trend is similar for all the three. Both Figs. show that interpolation of the image intensity before matching results in the best matching accuracy. In the control set, the bi-cubic interpolation of intensity and correlation perform alike up to the precision of 0.25 pixel below which they clearly separate. The bi-cubic interpolation of the correlation surface follows the intensity interpolation. The curve-fitting using the parabola and Gaussian models perform better than bi-cubic interpolations to only one half of the original pixel size. For the real mass movements, there is very little accuracy gain by interpolating to lower than 0.1 pixels. The control result shows that when the movement is only translation, the magnitude of the deviation is very low. Besides, it seems that for the control set interpolation to more detail level than 0.1 pixels improves the accuracy even further.

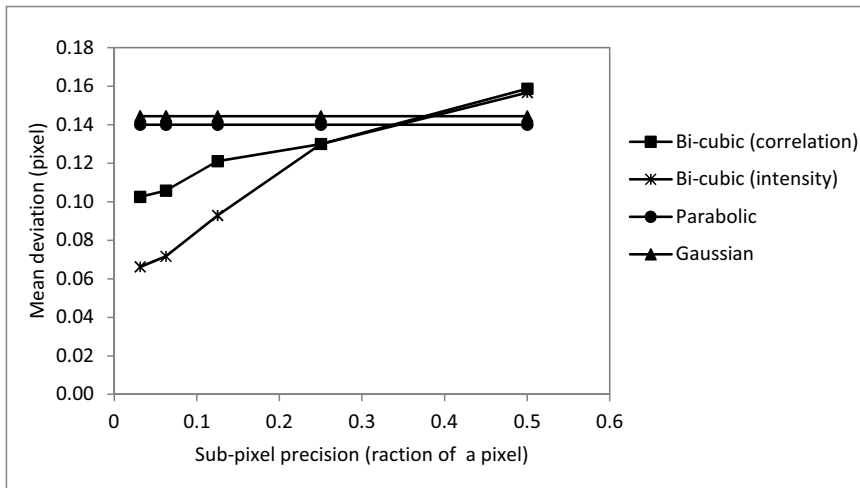


Fig. I-9 Comparison of the different sub-pixel precision approaches for the translation-only control image set.

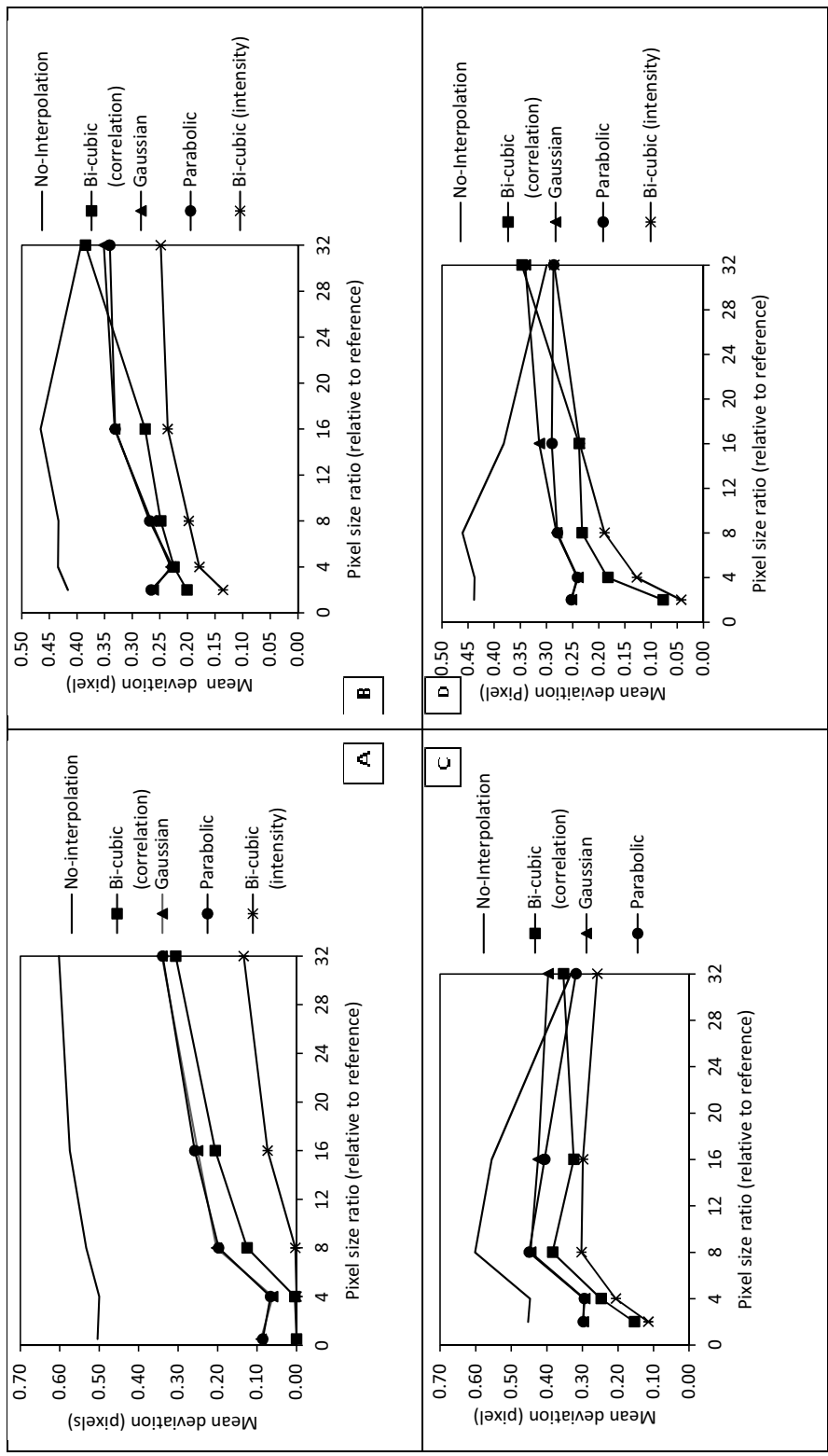


Fig. I-10. Mean deviation (normalized to pixel size) of the control set (A), rockglacier (B), landslide (C) and glacier (D) for the different sub-pixel precision algorithms

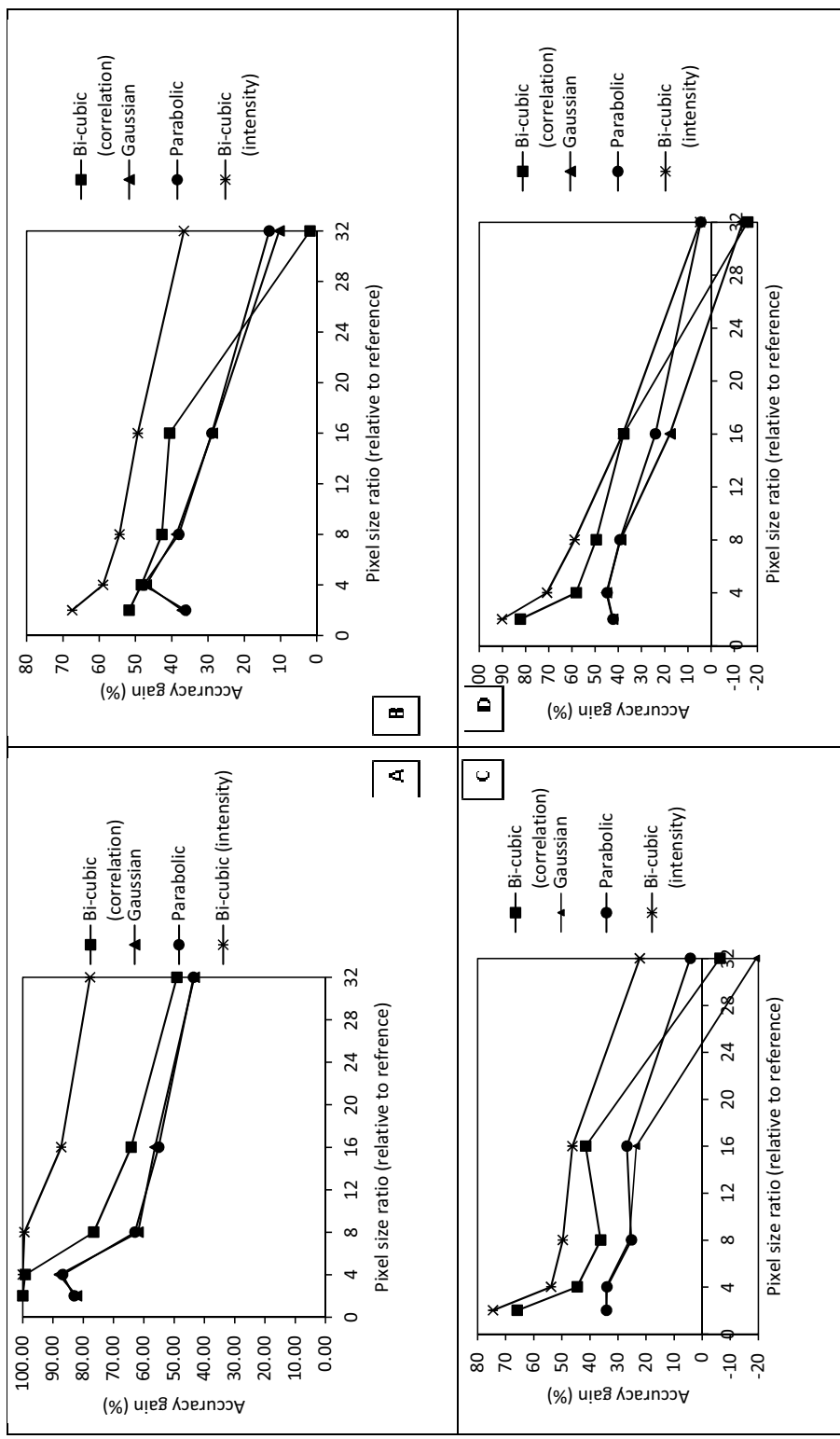


Fig. I-1.1. Percentage accuracy gain in relation to same resolution original image of the control set (A), rockglacier (B), landslide (C) and glacier (D) for the different sub-pixel algorithms



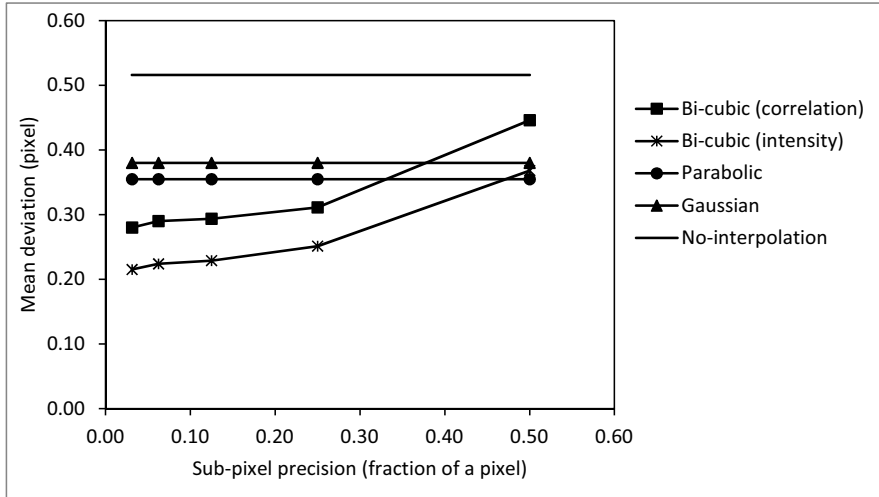


Fig. I-12 Comparison of the different sub-pixel precision approaches for the real mass movements averaged from the three mass movement types investigated

#### I.4.5. Relative performance of the algorithms at different sub-pixel details

This Section presents how much each level of sub-pixel detail substitutes original images of the same resolution. The set-up of this test is described in Section 2.5. Fig. I-10 shows the mean deviation between the matching position of the interpolated image pairs and the matching of the reference image pairs, against the factor of resolution difference between the original reference and the coarse image. Results are presented for the control set and the three mass movement types.

Fig. I-10 (A) shows that when the difference between the images is only the here-applied translation, sub-pixel interpolation of the image intensities up to  $1/8^{\text{th}}$  of the original pixel size prior to matching can perfectly substitute images of comparable original resolution. This exact substitution can be achieved by using bi-cubic interpolation of the correlation surface only up to  $1/4^{\text{th}}$  of the original pixel size. For example, a 16 m resolution image interpolated to 2 m using bi-cubic interpolation before matching performs exactly as a 2 m resolution image pair as long as there is no other source of difference between the image pairs than rigid translation. But when the level of detail goes beyond  $1/8^{\text{th}}$ , there appears to be a deviation between the two. The magnitude of these numbers depends, of course, on the translation magnitude applied in the control set. However, the test shows the better performance of bi-cubic intensity interpolation over the other sub-pixel algorithms tested.

For all the real mass movement types, as the difference in pixel size between the coarse resolution and the reference resolution increases, the deviation  $\overline{dev}$  of the sub-pixel matching position from the matching position of the same, but original image resolution, increases regardless of the algorithm (Fig. I-10 B, C and D). This means, not surprisingly, that the sub-pixel algorithm resembles images of comparable resolution less and less as the sub-pixel detail increases. At every resolution, the mean deviation is the lowest when intensity interpolation was used before matching followed by the bi-cubic interpolation of the correlation surface. The parabola- and Gaussian-based peak localizations perform poorer and alike. This confirms the above results based on the control set.

Remarkably, at a certain level of sub-pixel detail, the deviation between the sub-pixel algorithm and same resolution original image becomes high enough that further interpolation has no meaningful advantage. For the real mass movements used in this study, such level of detail is about 1/16<sup>th</sup> although the control set gives less deviation even at greater level of detail.

Similar performance is observed for the RMS although the differences are not as clear as for the mean deviation. Noticeably, the RMS of the pixel-precision matching of the control set is lower than that of the similarity interpolation whichever algorithm is chosen. For the real mass movements the lowest RMS is recorded for intensity interpolation followed by similarity interpolation using bi-cubic, parabolic and Gaussian algorithms.

No clear difference is observed among the algorithms in the proportion of mismatches. One of the advantages of sub-pixel algorithms is locating the exact position within the pixel and thus the detection of all movements as long as the resolution at which the interpolation is conducted is less than the displacement. This implies that when using low resolution images, slow-moving terminus and margins of the masses are hardly detected. For example, Fig. I-13 shows non-zero displacement vectors computed by matching images of 3.2 m ground pixel size without sub-pixel interpolation (black vectors) and after sub-pixel interpolation of the images to 0.4 m ground pixel size using bi-cubic interpolation (white vectors). As can be seen from the regions indicated by the four thick black arrows, slow motions, as typically found for e.g. towards the margins and terminus of a rockglacier, are detected only using sub-pixel interpolation. Success of displacement measurement from repeat images therefore varies spatially depending on the ground pixel size of the images and the displacement magnitude of the moving masses.

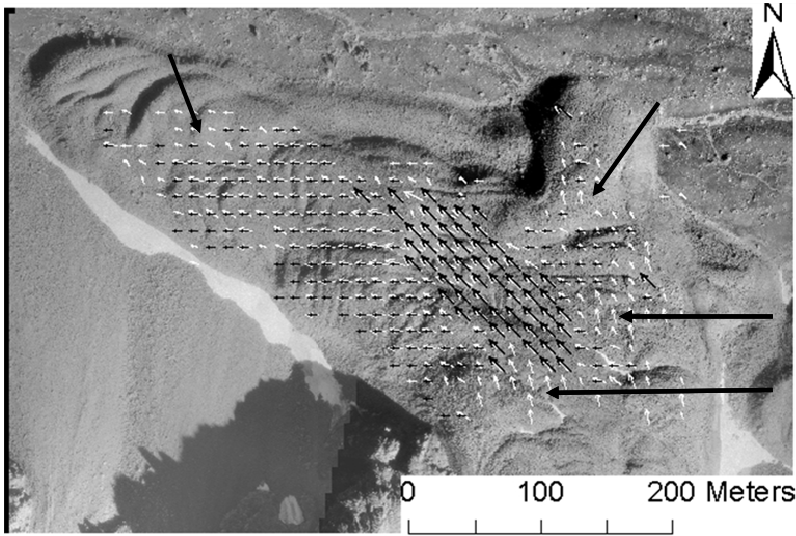


Fig. I-13. Spatial variation of the success of image matching at different ground pixel sizes. Black vectors are computed by matching images of 3.2 m ground pixel size while white vectors are computed by interpolating the images to 0.4 m ground pixel size and matching them afterwards. Notice the slow-moving regions indicated by the four thick black arrows

The decrease in errors due to the sub-pixel algorithms was also quantified as a measure of accuracy gain (*per<sub>i</sub>*) or as a measure of how much the sub-pixel precision emulates images of the resolution it models. Fig. I-11 (A) shows that in the case of the control set, intensity interpolation using the bi-cubic convolution can completely (100%) remove the mean deviation between the pixel precision matching position and the high resolution reference matching position when interpolated up to 1/8<sup>th</sup> of a pixel. This means for identical but translated images, for instance, when an image of 8 m resolution is used one can use intensity interpolation and compute displacements at 1 m precision and achieve the same accuracy as an original 1 m image. It is important to note that this does not mean that the matching is free of errors. It rather means that the error is the same as the error one would receive if one used original 1 m resolution images. Similar achievements can be obtained using similarity interpolation using bi-cubic interpolation up to only 1/4<sup>th</sup> of a pixel. Other algorithms could not achieve this 100% removal of the errors; they seem to contain systematic errors.

The algorithms did of course not perform so well for the real mass movements due to the fact that the matched images are not identical. The trends are however the same as the ones found for the control image. Fig. I-11 (B to D) shows that up to 80% error removal can

be achieved. Intensity interpolation performed best in all cases removing in average between 40% and 80% of the mean deviation when interpolated to  $1/16^{\text{th}}$  and one-half of a pixel, respectively. There is no point of interpolating beyond  $1/16^{\text{th}}$  of a pixel as the improvements gained are quite limited. According to our three test cases, for instance when using images of 16 m resolution such as approximately ASTER, one can use intensity interpolation and improve the accuracy of matching by 40% in reference to that obtained from matching 1 m original resolution images, or by 80% in reference to 8 m-resolution imagery.

## **I.5. Discussion**

### **I.5.1. Image resolution issues**

The effect of the spatial image resolution on the matching accuracy, as presented in Section 4.2, shows that, not surprisingly, all forms of errors increased with increasing pixel size. The mean deviation increased with increasing pixel size simply due to the systematic aggregation of the pixels. The reason why it deviates from linearity for the real mass movements at large pixel sizes can be ascribed to noise due to temporal surface changes, changes in imaging conditions, rotation and deformation which the control set is free of. The control is free of registration errors of the image pairs as well. Additionally and importantly, the fact that the template size is kept constant may have reduced the signal-to-noise ratio due to fewer numbers of pixels per template at large pixel sizes. Real mass movements are more sensitive to this due to the already lower SNR compared to the control set.

The random error (RMS) increases with pixel size due to a number of reasons. Firstly, for a fixed template size, the number of pixels decreases with increasing pixel size leading to lower information content (lower signal-to-noise ratio). Secondly, the low-resolution images used in this study were created by down-sampling the high-resolution images. Resampling introduces noise which increases with the resampling factor. The introduced noise and the noise that already exists in the original image from various sources lead to a higher RMS and even mismatches. If there are too few pixels in an entity, the entity may get chance-based matches in the target image as ambiguity and noise-related correlation dominates (Kanade and Okutomi 1991; Westerweel 1993). In reality, when low-resolution images are used, the random error might not be as high as the ones in this study. Firstly, the template sizes will be adjusted according to the image resolution. Secondly, noise in real images might be lower than that of the comparable resolution images created through down-sampling from high-resolution images.

As both the RMS and the mismatches are results of noise of various sources, image pairs such as the landslide and rockglacier which contain more noise due to the large temporal baselines have more of those errors (Fig. I-8 B and C). These large periods imply changes of the ground surfaces leading to poorer correlation. The mode of movement of these masses which is far from the pure translation of a rigid body including deformation and rotation also contributes to random errors. Especially the landslide moves in a fragmented pattern lacking good spatial coherence that is needed for good template correlation. The glacier observed over 1 month moves more coherently than the other mass movements and thus shows a relatively lower matching RMS. On the other hand, the control set, which contained only pure translation between otherwise identical images, did not have any random error or mismatch until the pixel size was increased by the factor of 8 and 16 respectively due to reduced SNR.

The proportion of undetected moving entities increases as the number of entities with displacements less than the pixel size increases (Fig. I-8 D and Fig. I-13). It is obvious that if one continues to increase the pixel size, there will be a point at which no moving template will be detected and the terrain would be reported stable. As can be observed from Fig. I-8 D, for the specific mass movements investigated here, if only pixel-level precision matching is to be used, the resolution of the images should not be coarser than about 3 m so that the majority of the displacements (less than 3 m) would be detected.

As stated in Section I.2, the bi-cubic method of resampling was used for the creation of the resolution pyramid. This does not perform significantly differently from signal averaging that happens within imaging sensors. A test run on the rockglacier image to compare the averaging method and the bi-cubic method showed no observable difference in performance between the two methods except when the factor of down-sampling is high. The difference in performance in the latter case originates from the difference in the number of nearby pixels that contribute to the computation of the value of the resampled pixel in the two methods. While weighted average of the 16 nearest pixels is used for the bi-cubic, arithmetic average of the aggregated pixels is used in the averaging method.

### **I.5.2. Performance of the sub-pixel algorithms and levels of detail**

Comparison of the sub-pixel precision approaches shows that intensity interpolation outperforms all the other algorithms of similarity interpolation. There can be two explanations to this. Firstly, in correlation interpolation the positions of the correlation values on which the interpolation is based, and which are computed based on coarse resolution images, influence

the position of the recomputed correlation peak. Secondly, the number of pixels in an entity is higher when intensity interpolation is applied leading to the suppression of noise. Fewer numbers of pixels in an entity makes the entity more susceptible to chance-based, i.e. erroneous matching results. This is able to explain the increased difference between the performances of the bi-cubic interpolation of the intensity and the correlation surface of the control images at very detailed levels of sub-pixel precision while they are very close at less detail level where the signal-to-noise ratio is still high.

The bi-cubic interpolation scheme that was used for the intensity interpolation is known to replicate the reference data better than most other interpolation schemes (Keys 1981), and it is known to approximate the *sinc* interpolation that is ideal in image interpolation (Dodgson 1992). This has led to the fact that the images re-interpolated from coarser resolutions were found to have high correlation with the aerial images of corresponding original resolution. For example, when the down-sampled rockglacier image of resolutions 0.4 m, 0.8 m, 1.6 m, 3.2 m and 6.4 m were re-interpolated to a resolution of 0.2 m (1/2 to 1/32 of a pixel respectively) their global correlation coefficients with the reference image of 0.2 m resolution were 0.98, 0.96, 0.93, 0.90 and 0.86 respectively. Although the images deteriorate due to resampling noise, they still remain well-correlated with the reference image due to the good performance of the interpolation algorithm. Correlation is, in fact, one of the quality measures of image interpolation (Lehmann et al. 1999). Fig. I-14 shows a sub-image over rockglacier in the original 0.2 m spatial resolution (A), a 1.6 m spatial resolution image resampled to 0.2 m, i.e. 1/8<sup>th</sup>, (B) and the 1.6 m spatial resolution itself (C). One can observe the clear image quality of the original 0.2 m spatial resolution (A) as compared to the resampled one (B) which appears to be noisy. The coarse 1.6 m spatial resolution (C) appears blurry showing the lack of detail.

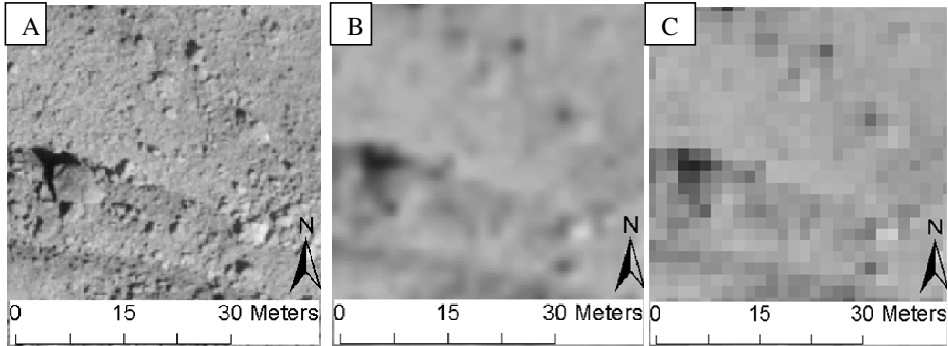


Fig. I-14 A part of the Muragl rockglacier image with original 0.2 m spatial resolution (A) and resampled to 0.2 m (B) from a 1.6 m resolution image (C)

The same interpolation algorithm, bi-cubic, performed also best in the similarity interpolation approach although not as good as in the intensity interpolation. The better performance in comparison to the Gaussian and parabola fitting is partially ascribed to the reasons explained above. In addition, parabola fitting is reported in many occasions to have a systematic bias known as “pixel locking”, which forces the estimated sub-pixel locations to approach integer values (Nobach and Honkanen 2005; Prasad et al. 1992). The presence of a systematic bias is testified by the fact that both parabola and Gaussian fitting could not remove 100% of the errors of pixel-level precision in the case of the control set unlike the other two algorithms (Fig. I-11). Although reports from PIV state that Gaussian peak finding does not have that kind of bias and performs better (Westerweel 1993; Willert and Gharib 1991), it performed no better than parabola fitting in the present study. We believe the underlying reason is the fact that the cross-correlation surfaces of the mass movements cannot be perfectly modeled by either parabolic or Gaussian functions. The image resolutions used in the present study are not high enough to be compared to that of particle images used in mechanics which are high enough to be approximated by, for example, Gaussian. Noise that is present in the images due to temporal surface changes and other sources contribute to the deviation of the correlation shape from both Gaussian and parabolic ones.

Finally, two important points regarding the size of the matching entities: first, in this study the absolute metric size of the matching entities was kept constant across image resolutions. This means that the number of pixels in each entity varies with the pixel resolution, leading to a variable signal-to-noise ratio. This had to be done for the sake of comparison. In reality, the size of matching entities will vary with the resolution of the image pair to keep a good signal-to-noise ratio. Second, the size of the matching entities was kept constant for the entire scene as is done in most area-based image matching practices.

### **I.5.3. Velocity fields**

The results of the present study for the Muragl rockglacier correspond very well with those of previous studies (Kääb 2002; Kääb and Vollmer 2000). Both the displacement vectors and their spatial variation agree with those studies, although comparison is not the aim here. The maximum velocity recorded here ( $0.45 \text{ ma}^{-1}$ ) is only slightly lower than the one recorded by Kääb (2002), i.e.  $0.5 \text{ ma}^{-1}$ , as the latter covered a wider geographical area. This shows the consistency of the NCC as a reliable tool for such applications. Since the Muragl rockglacier creep reflects spatio-temporally variable thermal regimes and ground compositions, also the

surface velocities vary. The presented results show mean horizontal velocities over 13 years (1981 to 1994).

Although a number of investigations have been conducted on the dynamics of the great Aletsch Glacier, there are only few regarding the landslides that are occurring in response to the glacier retreat. Investigations made for the period between 1976 and 1995 reported up to 2 m ( $10.5 \text{ cm a}^{-1}$ ) mean horizontal displacement magnitude (Kääb 2002, 2005). The 4 m ( $13 \text{ cm a}^{-1}$ ) maximum horizontal displacement magnitude reported in the present study is for the period 1976 to 2006, and shows only a slight increase in average horizontal velocity.

The displacement and velocity statistics obtained for the Ghiacciaio del Belvedere glacier agree well with the results presented in Kääb et al. (2005). Both studies used the same images. However, since the main focus of the present study was not to investigate the mass movements per se, the full extent of the image was not used. Therefore, the velocities were somewhat overestimated in comparison with the other study as, coincidentally, a part of slow-moving areas were left out of the present study. The high velocity of this glacier is recorded also by Haerberli et al. (2002) and Kääb et al. (2004).

The difference in velocity among the three types of masses can be ascribed to the sediment characteristics, terrain type, thermal regime, topography, etc. These velocity differences led to the use of images of different temporal resolutions. Large temporal baselines lead to changes in surface conditions decreasing the potential correlation between the two images. Slow-moving masses such as rockglaciers and landslides can be investigated using longer temporal baselines. Although the surfaces might not change drastically compared with a glacier, growth of vegetation and erosion of the surface can lead to decorrelation between the two images. This was a challenge in the landslide case. The rockglacier surface was found to be largely stable over the 13 year observation period. This stability owes to the lack of vegetation growth on the rockglacier surface and the somewhat rigid movement due to the geotechnical coherence by ground ice saturation. On the contrary, the landslide moves in a way that is far from rigid-body translation as the rock masses deform and fragment when moving. This leads to poorer correlation, increased random error and even mismatches in cases.



## I.6. Conclusions and outlook

This study has clarified a number of questions around the relation of accuracy and pixel or sub-pixel resolution when matching terrain displacements such as glacier flow, land sliding and permafrost creep from repeat optical images by using pixel-precision correlation measures, here namely the normalized cross correlation (NCC). The study contributes to better exploiting the large archives of repeat remotely sensed images that exist over actual or potential Earth surface mass movements, as well as to better meeting the increasing needs to quantify and monitor mass movements, in particular when they are accompanied by adverse effects.

The study has in particular evaluated the performance of two different approaches to sub-pixel precision in NCC for displacement measurement based on repeat images. It has also investigated the influence of pixel resolution on image matching and displacement estimation. The findings reveal that with increasing pixel size, all types of matching errors increase. The mean deviation between a displacement and its reference measurement has a linear relationship with the factor by which the pixel size increases. Random errors and mismatches tend to be higher for larger temporal baselines and where the mode of the movement deviates much from rigid-body translation.

When sub-pixel accuracy is aimed for, interpolating image intensities to a higher resolution using bi-cubic interpolation prior to the actual image correlation performs better than both interpolation of the correlation surface using the same algorithm and peak localization using curve fitting. Correlation peak localization using the Gaussian and polynomial algorithms are inferior in such applications.

Therefore, we conclude that more precise and accurate displacement measurements are obtained by interpolating the available images to a higher resolution using bi-cubic interpolation prior to matching. In such approaches, one can gain over 40% reduction in mean error (in reference to the same resolution original image) by interpolating the images to up to  $1/16^{\text{th}}$  of a pixel. Interpolating to a more detailed sub-pixel resolution than  $1/16^{\text{th}}$  of a pixel does not add much. Or in other words, when matching low-resolution images using normalized cross-correlation with intensity-interpolation based sub-pixel precision, 40% or better accuracy increment can be achieved compared to pixel-precision matching in reference to images with the same original resolution as the interpolated image. When actual low-resolution images are used together with varying sizes of matching entities, as opposed to the approach used in this study, even better precision and accuracy might be obtained as the noise

due to resampling will not be present, and template and search window sizes will be adjusted with the pixel size.

Although the relative performances of the algorithms is expected to be valid at least for other spatial domain matching approaches and for other applications, the magnitudes given here are strictly valid only for the similarity measure and test sites used in this paper. Validation outside the conditions described in this study requires further research focusing on the development of a rigorous theoretical concept. Future investigations can, for example, aim at comparing the relatively best performing algorithm of this finding to other area-based approaches that intrinsically result in sub-pixel precision, namely least squares matching and Fourier-based phase matching. Besides, the performance of the approach in comparison with feature-based approaches needs to be evaluated as well. There are also other accuracy improving approaches such as preprocessing (e.g. noise filtering) and post-processing (e.g. filtering of displacement vectors by averaging). Further research is needed to know if they even improve the accuracy further after sub-pixel precision.

## **Acknowledgements**

Special thanks are due to three anonymous referees and the editor of the paper for their careful and constructive comments. We would like to express our gratitude to the colleagues of the Geomatics Section of our department for their fruitful discussions on the manuscript. We are also very grateful to Kimberly Ann Casey for proof reading of the manuscript. The orthoimages of the Aletsch rockslide and the Muragl rockglacier are based on air photos acquired by the Swisstopo/flight service (BA057212, BA081844). The orthoimages of the Belvedere glacier are based on air photos by Swisstopo and CNR-IRPI within the Glaciorisk project. This study is funded by the Research Council of Norway (NFR) through the CORRIA project (no. 185906/V30) and contributes to the NFR International Centre for Geohazards (SFF-ICG 146035/420) and the ESA DUE GlobGlacier project.

## **I.7. References**

Althof, R.J., Wind, M.G.J., & Dobbins, J.T., III (1997). A rapid and automatic image registration algorithm with subpixel accuracy. *IEEE Transactions on Medical Imaging*, 16, 308-316

- Barsch, D. (1996). *Rockglaciers: Indicators for the Present and Former Geoecology in High Mountain Environments*. Berlin: Springer Verlag
- Brown, L.G. (1992). A survey of image registration techniques. *ACM Comput. Surv.*, 24, 325-376
- Crippen, R.E., & Blom, R.G. (1991). Measurement of subresolution terrain displacements using Spot panchromatic imagery. In, *Geoscience and Remote Sensing Symposium, 1991. IGARSS '91. Remote Sensing: Global Monitoring for Earth Management., International* (pp. 1667-1670)
- Delacourt, C., Allemand, P., Casson, B., & Vadon, H. (2004). Velocity field of the "La Clapière" landslide measured by the correlation of aerial and QuickBird satellite images. *Geophys. Res. Lett.*, 31, 15-19
- Dodgson, N.A. (1992). *Image resampling*. London: University of Cambridge Computer Laboratory
- Haerberli, W., & Beniston, M. (1998). Climate change and its impacts on glaciers and permafrost in the Alps. *Ambio*, 27, 258-265
- Haerberli, W., Cihlar, J., & Barry, R.G. (2000). Glacier monitoring within the Global Climate Observing System. *Annals of Glaciology*, 31, 241-246
- Haerberli, W., Kääh, A., Paul, F., Chiarle, M., Mortara, G., Mazza, A., Deline, P., & Richardson, S. (2002). A surge-type movement at Ghiacciaio del Belvedere and a developing slope instability in the east face of Monte Rosa, Macugnaga, Italian Alps. *Norsk Geografisk Tidsskrift - Norwegian Journal of Geography*, 56, 104 - 111
- Haug, T., Kääh, A., & Skvarca, P. (2010). Monitoring ice shelf velocities from repeat MODIS and Landsat data - a method study on the Larsen C ice shelf, Antarctic Peninsula, and 10 other ice shelves around Antarctica. *The Cryosphere*, 4, 161-178
- Huang, H., Dabiri, D., & Gharib, M. (1997). On errors of digital particle image velocimetry. *Measurement Science and Technology*, 8, 1427-1440
- Kanade, T., & Okutomi, M. (1991). A Stereo Matching Algorithm with an Adaptive Window - Theory and Experiment. *1991 IEEE International Conference on Robotics and Automation, Vols 1-3*, 1088-1095
- Kaufmann, V., & Ladstädter, R. (2003). Quantitative analysis of rock glacier creep by means of digital photogrammetry using multi-temporal aerial photographs: two case studies in the Austrian Alps. In M. Phillips, S.M. Springman & L.U. Arenson (Eds.), *Eighth international conference on permafrost* (pp. 525-530). Zurich, Switzerland: Taylor & Francis

- Keys, R.G. (1981). Cubic convolution interpolation for digital Image processing. *IEEE transactions on acoustics, speech and signal processing*, 29, 1153-1160
- Kääb, A. (2002). Monitoring high-mountain terrain deformation from repeated air- and spaceborne optical data: examples using digital aerial imagery and ASTER data. *ISPRS Journal of Photogrammetry and Remote Sensing*, 57, 39-52
- Kääb, A. (2005). *Remote sensing of mountain glaciers and permafrost creep*. Zürich: Geographisches Institut der Universität Zürich
- Kääb, A., Huggel, C., Barbero, S., Chiarle, M., Cordola, M., Epifani, F., Haeblerli, W., Mortara, G., Semino, P., Tamburini, A., & Viazzo, G. (2004). Glacier hazards at Belvedere Glacier and the Monte Rosa east face, Italian Alps: processes and mitigation. In, *Internationales Symposium Interpraevent* (pp. 67-78). Riva/Trient
- Kääb, A., Huggel, C., Fischer, L., Guex, S., Paul, F., Roer, I., Salzmann, N., Schlaefli, S., Schmutz, K., Schneider, D., Strozzi, T., & Weidmann, Y. (2005). Remote sensing of glacier- and permafrost-related hazards in high mountains: an overview. *Nat. Hazards Earth Syst. Sci.*, 5, 527-554
- Kääb, A., & Vollmer, M. (2000). Surface geometry, thickness changes and flow fields on creeping mountain permafrost: automatic extraction by digital image analysis. *Permafrost and Periglacial Processes*, 11, 315-326
- Lehmann, T.M., Gonner, C., & Spitzer, K. (1999). Survey: interpolation methods in medical image processing. *IEEE Transactions on Medical Imaging*, 18, 1049-1075
- Leprince, S., Barbot, S., Ayoub, F., & Avouac, J.P. (2007). Automatic and Precise Orthorectification, Co-registration, and Subpixel Correlation of Satellite Images, Application to Ground Deformation Measurements. *Geoscience and Remote Sensing, IEEE Transactions on*, 45, 1529-1558
- Lewis, J.P. (1995). Fast Normalized Cross-Correlation. *Vision Interface*, 120-123
- Lourenco, L., & Krothapalli, A. (1995). On the accuracy of velocity and vorticity measurements with PIV. *Experiments in Fluids*, 18, 421-428
- Meijering, E., & Unser, M. (2003). A note on cubic convolution interpolation. *IEEE Transactions on Image Processing*, 12, 477-479
- Nobach, H., & Honkanen, M. (2005). Two-dimensional Gaussian regression for sub-pixel displacement estimation in particle image velocimetry or particle position estimation in particle tracking velocimetry. *Experiments in Fluids*, 38, 511-515

- Prasad, A., Adrian, R., Landreth, C., & Offutt, P. (1992). Effect of resolution on the speed and accuracy of particle image velocimetry interrogation. *Experiments in Fluids*, 13, 105-116
- Quincey, D.J., Lucas, R.M., Richardson, S.D., Glasser, N.F., Hambrey, M.J., & Reynolds, J.M. (2005). Optical remote sensing techniques in high-mountain environments: application to glacial hazards. *Progress in Physical Geography*, 29, 475-505
- Rebetez, M., Lugon, R., & Baeriswyl, P.-A. (1997). Climatic change and debris flows in high mountain regions: the case study of the Ritigraben Torrent (Swiss Alps). *Climatic Change*, 36, 371-389
- Ritter, M. (2006). The physical environment: an introduction to physical geography. 10.01.2009: [http://www.uwsp.edu/geo/faculty/ritter/geog101/textbook/title\\_page.html](http://www.uwsp.edu/geo/faculty/ritter/geog101/textbook/title_page.html), 14.06.2010
- Scambos, T.A., Dutkiewicz, M.J., Wilson, J.C., & Bindschadler, R.A. (1992). Application of image cross-correlation to the measurement of glacier velocity using satellite image data. *Remote Sensing of Environment*, 42, 177-186
- Scherler, D., Leprince, S., & Striker, M.R. (2008). Glacier-surface velocities in alpine terrain from optical satellite imagery--Accuracy improvement and quality assessment. *Remote Sensing of Environment*, 112, 3806-3819
- Shimizu, M., & Okutomi, M. (2002). An analysis of sub-pixel estimation error on area-based image matching. In, *14th International Conference on Digital Signal Processing* (pp. 1239-1242 )
- Skvarca, P., Arup, B., & De Angelis, H. (2003). Recent behavior of Glaciario Upsala, a fast-flowing calving glacier in Lago Argentino, southern Patagonia. *Annals of Glaciology*, 36, 184-188
- Szeliski, R., & Scharstein, D. (2002). Symmetric Sub-pixel Stereo Matching. *Computer Vision — ECCV 2002* (pp. 657-659)
- Taylor, M.H., Leprince, S., Avouac, J.P., & Sieh, K. (2008). Detecting co-seismic displacements in glaciated regions: An example from the great November 2002 Denali earthquake using SPOT horizontal offsets. *Earth and Planetary Science Letters*, 270, 209-220
- Toutin, T. (2004). Review article: Geometric processing of remote sensing images: models, algorithms and methods. *International Journal of Remote Sensing*, 25, 1893 - 1924

- Vosselman, G., Sester, M., & Mayer, H. (2004). Basic computer vision techniques. In J.C. McGlone (Ed.), *Manual of photogrammetry* (pp. 455-504). Bethesda: American Society of Photogrammetry and Remote Sensing
- Wangenstein, B., Gumundsson, Á., Eiken, T., Kääb, A., Farbroth, H., & Etzelmüller, B. (2006). Surface displacements and surface age estimates for creeping slope landforms in Northern and Eastern Iceland using digital photogrammetry. *Geomorphology*, 80, 59-79
- Westerweel, J. (1993). *Digital particle image velocimetry: theory and application*. Delft: Delft University Press
- Whillans, I.M., & Tseng, Y.-H. (1995). Automatic tracking of crevasses on satellite images. *Cold Regions Science and Technology*, 23, 201-214
- Willert, C.E., & Gharib, M. (1991). Digital particle image velocimetry. *Experiments in Fluids*, 10, 181-193
- Yamaguchi, Y., Tanaka, S., Odajima, T., Kamai, T., & Tsuchida, S. (2003). Detection of a landslide movement as geometric misregistration in image matching of SPOT HRV data of two different dates. *International Journal of Remote Sensing*, 24, 3523 - 3534
- Zhao, F., Huang, Q.M., & Gao, W. (2006). Image matching by normalized cross-correlation. In, *31st IEEE International Conference on Acoustics, Speech and Signal Processing* (pp. 1977-1980). Toulouse, FRANCE
- Zitová, B., & Flusser, J. (2003). Image registration methods: a survey. *Image and Vision Computing*, 21, 977-1000







## II. Locally adaptive template sizes for matching repeat images of Earth surface mass movements<sup>2</sup>

Misganu DEBELLA-GILO<sup>a</sup> and Andreas KÄÄB<sup>b</sup>

<sup>a,b</sup>Institute of Geosciences, University of Oslo, P. O. Box 1047, Oslo, Norway

<sup>a</sup>[m.d.gilo@geo.uio.no](mailto:m.d.gilo@geo.uio.no) (corresponding author)

**ABSTRACT.** This paper presents an algorithm for locally adaptive template sizes in normalized cross-correlation (NCC) based image matching for measuring surface displacement of mass movements. After adaptively identifying candidate templates based on the image signal-to-noise ratio (SNR), the algorithm iteratively looks for the size at which the maximum cross-correlation coefficient attains a local peak and the matching position gets fixed. The algorithm is tested on modeled (deformed) images and applied to real bi-temporal images of different Earth surface mass movements. It is evaluated in comparison with globally (image-wide) fixed template sizes ranging from 11 to 101 pixels based on the improvement in the accuracy of displacement estimation and the SNR of the matching. The results show that the algorithm could reduce the error of displacement estimation by up to over 90% (in the modeled case) and improve the SNR of the matching by up to over 4 times compared to the globally fixed template sizes. The algorithm reduces the effects of geometric distortion and noise. Besides, it excludes most of the templates that lack good signal variance from the analysis through its candidate selection step. The algorithm pushes terrain displacement measurement from repeat images one step forward towards full automation. Although not investigated, the findings are expected to be useful for other area-based image matching methods in the spatial domain.

**Keywords:** Image matching, Repeat imagery, Normalized cross-correlation, Change detection, Mass movement, Displacement, Adaptive template

### II.1. Introduction

One of remote sensing techniques that have become increasingly popular in analyzing and monitoring Earth surface mass movements is matching of repeat images (e.g. Debella-Gilo and Käab, 2011; Haug et al., 2010; Käab and Vollmer, 2000; Scambos et al., 1992; Scherler et al., 2008; Taylor et al., 2008; Wangensteen et al., 2006). Of the image matching methods available, the group of area-based methods with the normalized cross-correlation (NCC) as its similarity measure is widely used due to its simplicity and reliability (Brown, 1992; Zitová

---

<sup>2</sup> ISPRS Journal of Photogrammetry and Remote Sensing, Revision submitted

and Flusser, 2003). The NCC calculates the correlation coefficient between an image subset (template) in the reference image and template of the same size in the target (search) image (Lewis, 1995; Vosselman et al., 2004). It assigns the correlation coefficient to the central pixel (i.e. the pixel at the center of the square template) of the search template. It continues doing so by moving the search template by one pixel at a time until the entire search window is covered. The pixel within the search window which produces the maximum correlation coefficient is considered as the best matching central pixel. Horizontal displacement is then computed as the Euclidean distance between the positions of the central pixels of the reference and the matching templates. This displacement is then assigned to all pixels of the template.

There are two key assumptions here. First, the template that produces the highest correlation coefficient is unambiguously the matching template. Second, all the pixels within the template are displaced rigidly. This means that the two matching templates are equal in size, shape and orientation. The first assumption is realized if there is no ambiguity between the true match and duplicates. The second assumption is realized if the template is not changed in shape, size and orientation.

The ideal situation would be finding a match for each and every pixel independently which is not practically possible and feasible. An image subset (template) is therefore created by including neighboring pixels until the entity becomes unique. The number of the neighboring pixels to be included in the subset basically depends on a number of factors such as surface roughness (contrast), the noise content of the image and the extent of geometric distortion (Schenk, 1999).

In principle, increasing the size of the template makes the template more unique (Okutomi and Kanade, 1990; Schenk, 1999). However, increasing template size poses two challenges. First, it increases the computation time exponentially which is, however, not anymore a major concern for many applications over limited areas. Secondly, it increases geometric distortion within the template. The challenge in deciding template size is therefore finding the optimum size that contains high signal variation in relation to noise variation with minimum geometric distortion. As these parameters vary spatially, template sizes need to be locally adaptive (Kanade and Okutomi, 1994; Okutomi and Kanade, 1990; Okutomi and Kanade, 1992). The local adaptability becomes even more important in Earth surface mass movements due to the often non-rigid motion of these masses and the often necessary large temporal baseline.

Attempts made so far to achieve this locally adaptive optimum template size vary fundamentally and/or in the parameters and assumptions they rely on. Most popularly, intensity and statistical models of the disparity distribution within the template are used to determine optimum template sizes for each central pixel (Kanade and Okutomi, 1994; Okutomi and Kanade, 1990; Okutomi and Kanade, 1992; Scherer et al., 1998). Multiple fixed window sizes are also found to be improving the accuracy over fixed windows (Fusiello et al., 1997). Template sizes are also related to physical boundaries by using disparity variation together with edge boundaries as limits to window sizes, combining area-based matching with feature-based matching (Koo and Jeong, 2001; Lotti and Giraudon, 1994). There are approaches that use weighting of the pixels in the template (Yihua et al., 2002; Yoon and Kweon, 2006). Pan et al. (2008) used combination of noise variance and sum of square of intensity gradients to select subset size in digital image correlation. Cyganek (2005) presents an adaptive window growing technique based on the entropy of the window. Entropy and intensity variances can be used to identify matchable templates with good information content. However, they do not guarantee the presence of conjugate for such candidates in the search image.

The algorithm presented here aims at locally adaptive optimization of template sizes in NCC-based image matching for displacement measurement of Earth surface mass movements. It relies on the maximization of the signal-to-noise ratio (SNR) for matchable template identification. The algorithm then iteratively defines optimum template sizes based on the local maximization of the peak of the NCC coefficient which is another way of minimization of uncertainty of the matching. The optimization is based on the principle that the reliability of a match for a template with optimum size should be greater than not only that of other templates but also that of the same (concentric) templates with other sizes.

The paper starts by investigating the influence of template size on signal-to-noise ratio and on the NCC coefficient. Based on the findings of these investigations, presentation of a new algorithm for adaptively identifying candidate templates and iteratively determining their optimum sizes follows. The procedures of testing, implementation and evaluation of the algorithm are then presented together with the datasets used. After presenting and discussing the results, the paper winds up by giving concluding remarks.

## II.2. Template size in image matching

A template in this context refers to an image subset of a square shape defined in the reference image for which a conjugate is sought in the search image. Template size is defined by  $2\tau + 1$  by  $2\tau + 1$  pixels, where  $\tau$  represents the number of pixels on either side of the central pixel  $[x, y]$  in both dimensions (Fig. II-1). Similarly, the size of the search area is defined by  $2\omega + 1$  by  $2\omega + 1$ . Area-based image matching in the spatial domain using NCC is basically measurement of co-variation of the intensities of the two templates being matched, i.e.  $f(x, y)$  and  $t(x-u, y-v)$ . Therefore, templates which lack a significant level of intensity variance are not good candidates for matching. Information content of an image subset is better represented by SNR. The information content (SNR) per ground size of an image subset is among others dependent on the image contrast (roughness), noise and the ground pixel size (Gonzalez and Woods, 2008; Woodcock and Strahler, 1987). A good matching candidate over an area is obtained if the surface has good contrast, the images contain low level of noise and the spatial resolution of the image is high.

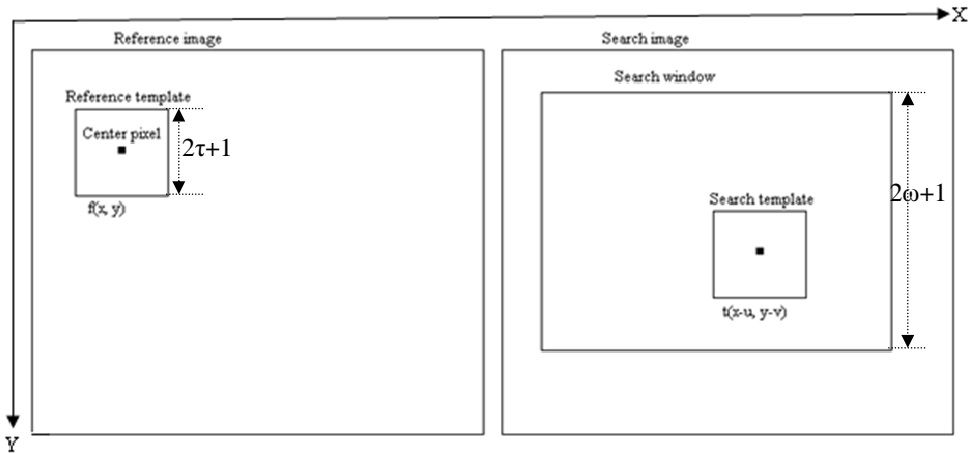


Fig. II-1 The structural layout of reference image, search image, reference template, search template and search window in area-based image matching

Image matching becomes successful only when an exact match with precise location has been identified. Thus, it is not only the identification of the matchable templates but also their presence (or absence) and location in the second image that is important. The (un)certainty of the presence of a match is measured by the value and location of the peak of the NCC coefficient. Therefore, the behavior of the SNR and the maximum NCC coefficient has to be

explored in relation to different template sizes so that an automatic method of defining locally adaptive optimum template sizes may be devised.

### II.2.1. Template size and signal-to-noise ratio

Assume  $I(x_i, y_j)$  represents the intensity value of pixels  $[x_i, y_j]$  in an image (or its subset) with size  $M$  rows by  $N$  columns. The mean ( $\bar{I}$ ) and variance ( $\sigma^2$ ) of the image intensity for  $MN$  number of pixels are computed as in Eqs. II-1 and II-2 respectively.

$$\bar{I} = \frac{\sum_{i,j}^{M,N} I(x_i, y_j)}{MN} \quad \text{II-1}$$

$$\sigma^2(I) = \frac{\sum_{i,j}^{M,N} (I(x_i, y_j) - \bar{I})^2}{MN} \quad \text{II-2}$$

For every pixel  $[x_i, y_j]$  the digital number ( $I$ ) contains the true image signal ( $S$ ) and noise ( $e$ ). Thus, intensity variance has to be decomposed into noise and signal variances. The major type of noise that affects optical image is additive noise although other noise types may also be present (Gonzalez and Woods, 2008). This noise type is stationary, independent of the signal, and Gaussian distributed with zero mean and variance  $\sigma^2(e)$ . Thus:

$$I = S + e \quad \text{II-3}$$

$$\sigma^2(I) = \sigma^2(S + e) \quad \text{II-4}$$

$$\sigma^2(S + e) = \sigma^2(S) + \sigma^2(e) + 2\gamma(S, e) \quad \text{II-5}$$

Here,  $\sigma^2(S)$  is the signal variance;  $\sigma^2(e)$  is the noise variance; and,  $\gamma(S, e)$  is the covariance between the signal and noise. Since the noise is assumed to be completely independent of the signal,  $\gamma(S, e)$  equals zero. Image variance is thus the sum of signal variance and noise variance. It can be decomposed into the signal and noise variances by computationally estimating noise variance and subtracting it from the image variance (Eq. II-6). The *SNR* can then be computed as in Eq. II-7.

$$\sigma^2(S) = \sigma^2(I) - \sigma^2(e) \quad \text{II-6}$$

$$\text{SNR} = \frac{\sigma^2(S)}{\sigma^2(e)} \quad \text{II-7}$$

A fast and efficient approach to noise variance estimation is presented by (Immerkær, 1996) where the difference between two Laplacian masks is used to convolve the image. The mask has zero mean and is almost insensitive to image structures such as edges. The variance of the output of the convolution is used to estimate noise variance. Eqs. II-2 and Immerkær's method are used to compute image and noise variances respectively for varying template sizes to investigate the relationship between SNR and template sizes. Image and noise variances are computed for  $\tau$  values ranging from 1 to a maximum size set (Fig. II-1). The  $M$  and  $N$  of Eqs. II-1 and II-2 are replaced by  $(2\tau + 1)$  each.

The relationship is first investigated on a synthetic image which is made of square grid features of 61 by 61 pixels that repeat themselves with clear edges at their borders (Fig. II-2). Intensity values within each grid vary non-uniformly in all directions from the center. The synthetic image is used to investigate how SNR is related to feature boundaries (edges) and information content in a controlled situation. The computation was then extended to real images of Earth surface masses. It was later conducted on images down-sampled to lower resolutions to understand the relationship between SNR and template size is affected by ground pixel size.

The findings show that the SNR is low for small template sizes (Fig. II-2 A to C). This is because at small template sizes noise and signal are hardly distinguished. As the template size increases, the SNR increases as well indicating that new pixels bring in new variances. If the template reaches an edge, the SNR increases considerably as edges are characterized by sharp intensity change. After the edge is crossed, the SNR tends to decrease as the new pixels do not add new information. If, however, another edge is encountered, the SNR increases again. Therefore, SNR plotted against template sizes will characteristically show a number of peaks depending on the presence of edges. Even if no edge is encountered, the SNR does not keep on increasing indefinitely. It will reach a certain peak and starts to decrease when new sources of variation cease to appear. In both cases, the size at which the first peak is attained defines the minimum size of the unique entity surrounding the central pixel.

In the examples of the synthetic images, when the central pixel is placed at the center of the grid (Fig. II-2 A), the local maxima (peaks) of the SNR are observed at window sizes ca. 60 pixels and its multiples indicating the repetitive patterns (Fig. II-2 lower right A). This size is the edge-crossing size. When the central pixel is located at the edges of the grids (Fig. II-2 B), the image variance starts with high value due to the high intensity variation at the edges although the SNR attains the first peak at a similar template size. For other locations

(Fig. II-2 C), the window size at which the SNR attains a peak varies depending on the distance of the point from the edges (Fig. II-2 lower right C). The peaks coincide with edges or boundaries of unique entities which in most cases represent physical feature boundaries. These findings show that SNR can be used to identify the smallest size of distinct features around a given point. It is also a good parameter for identifying image sections that lack such clear pattern of SNR as shown by the examples.

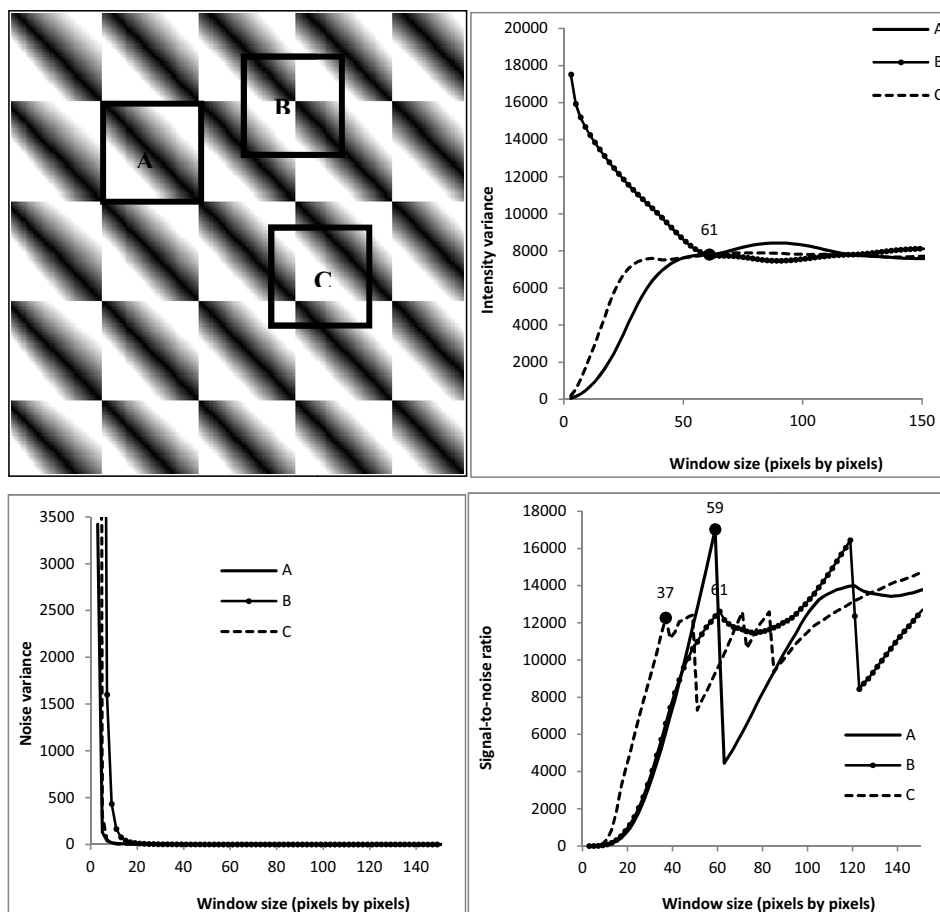


Fig. II-2 The center pixel located at the center (A), corner (B) and randomly in a grid (C) of a synthetic image with their respective image intensity variance (upper right), noise variance (lower left) and signal-to-noise ratio together with the first local maximum (lower right) as plotted against the window size around the center pixel

The computation was extended to real images of Earth surface masses. The results are organized for convenience of presentation in Figs. 3 to 5. For example, distinct surface

features such as rock blocks in an aerial image of a rockglacier exhibit a clear SNR peak due to the edge-like behavior at the boundaries often enhanced by the shadow of the block (Fig. II-3). However, not all Earth surface masses contain such distinct features at the image resolutions usually available. When the intensity variation is smooth, the SNR peak is also less pronounced (Fig. II-4). As long as there is good signal variation and there is a limited level of noise, SNR will reach a certain local peak identifying a unique entity.

The influence of noise at small template sizes can easily be observed by the differences between image variance and SNR as exhibited by the noisy synthetic aperture radar (SAR) image over a glacier (Fig. II-5). This type of images has very low SNR due to its high noise content (radar speckle) which is characteristic for SAR intensity images.

Monotonous features that lack signal variance as in the case of low contrast surfaces such as snow, water and shadow lack the distinct SNR maxima. Even if they have a certain SNR peak, they attain it at very large size, which shows that the peak is attributed more to the far off entities than to the entity close to the central pixel. They also have very low SNR values as shown by the monotonously dark image of Fig. II-3 and bright image of Fig. II-4. Such entities are not good candidates for area-based spatial domain image matching as they lack adequate signal variance.

The examples show that the SNR attains certain peaks regardless of the ground pixel size. However, the ground distance over which these peaks are attained is dependent on the ground pixel size. Computation of SNR for the same central pixel at different ground pixel size, although not shown here, reveals that the metric window size of SNR peak is resolution dependent. The metric window size at which the SNR peak is attained remains constant only over a short range of ground pixel sizes. Investigations show that images over a certain feature attain high signal variance when the ground pixel size is just less than the average size of the surface features (Woodcock and Strahler, 1987). When the ground pixel size changes, the scale at which the observation is carried out, and hence the features being observed, change. Therefore, in addition to the intra-image variation, the optimum size of a unique entity at an individual location varies across images depending, among others, on the spatial resolution of the images.



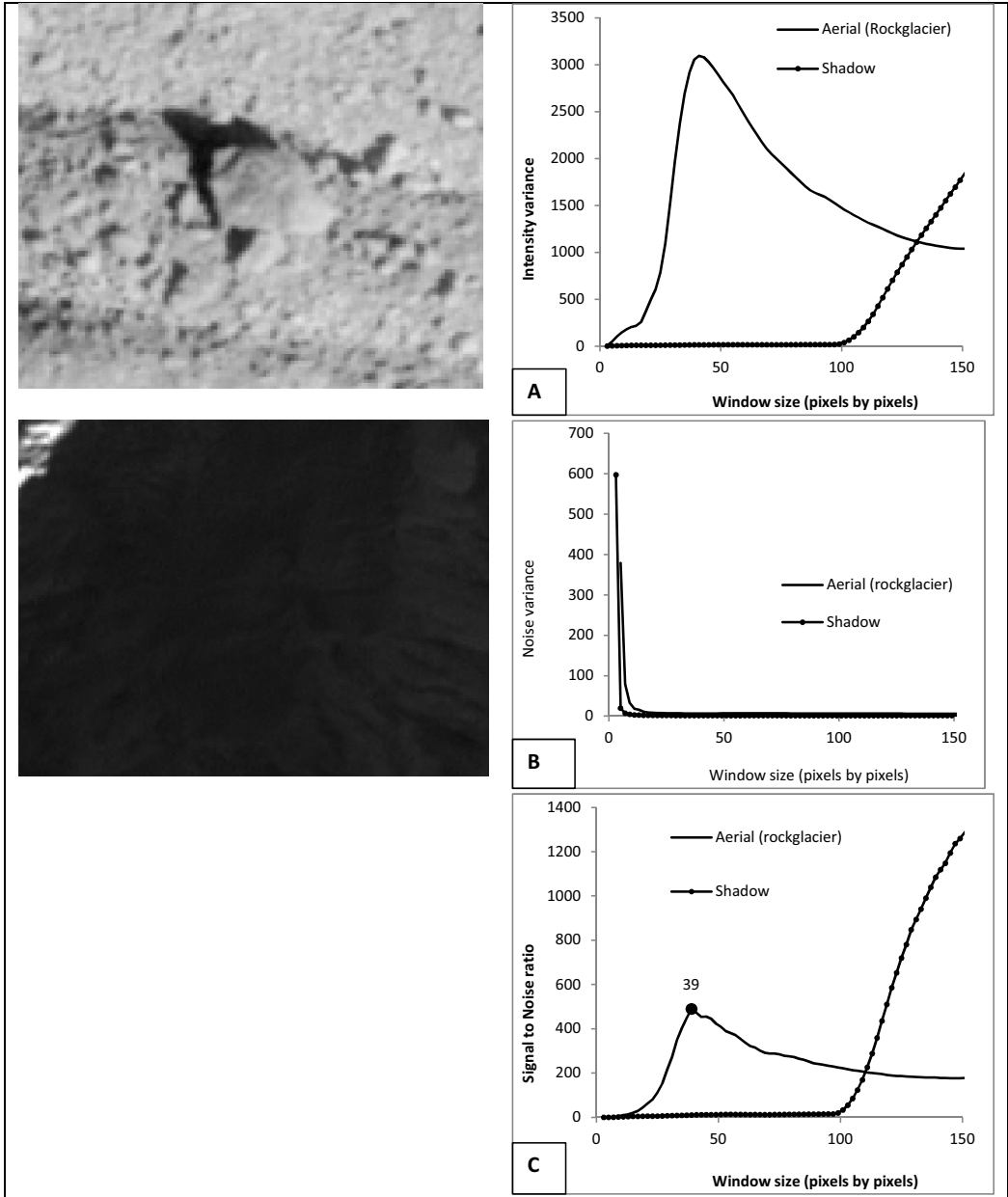


Fig. II-3 Image intensity variance (A), noise variance (B) and signal-to-noise ratio together with the first local maximum (D) as plotted against the window size for an aerial image of real rock block (upper left) shadow area (lower left)

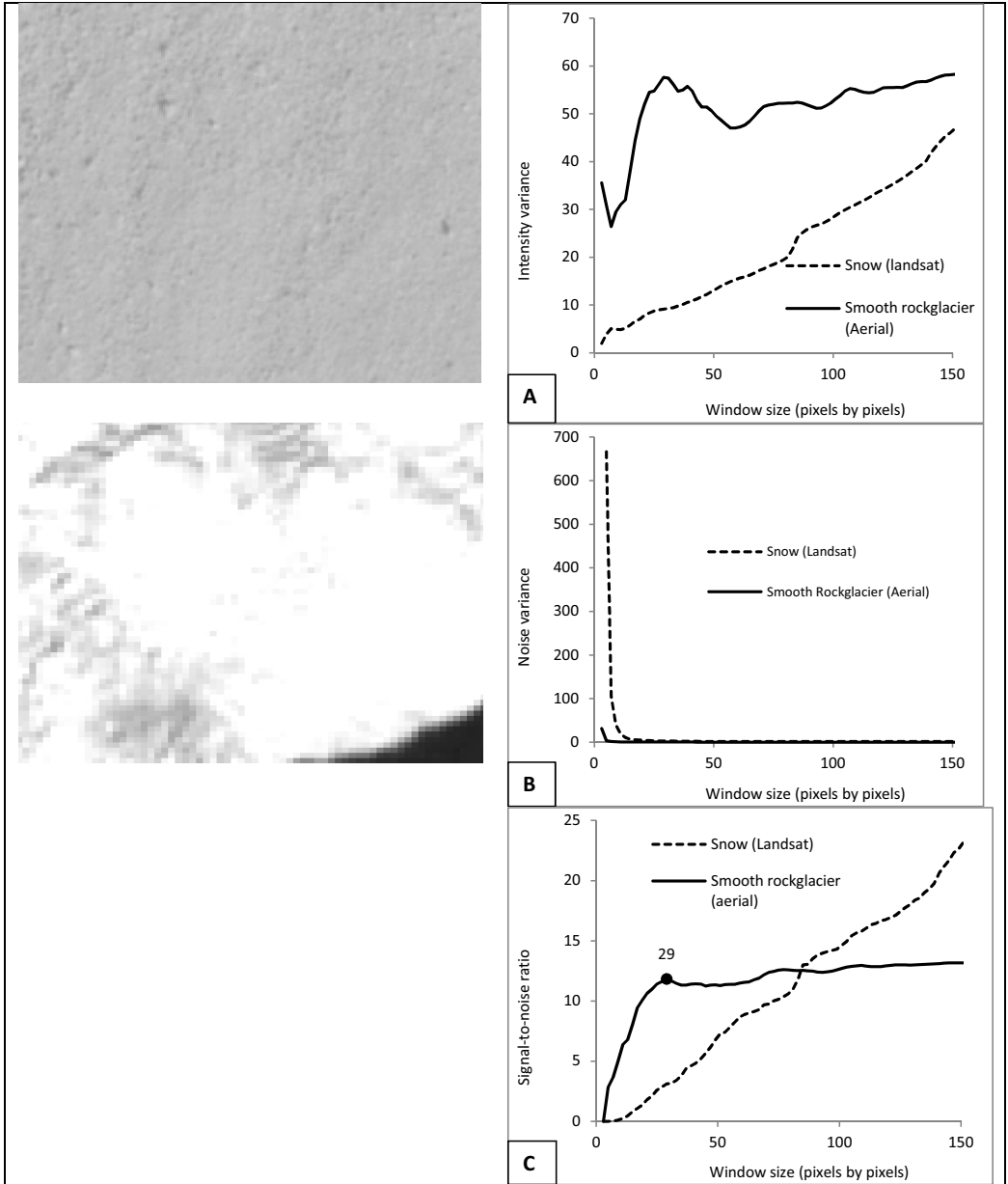


Fig. II-4 Image intensity variance (A), noise variance (B) and signal-to-noise ratio together with the first local maximum (C) as plotted against the window size for an aerial image of a fine-grained rockglacier surface (upper left) and a snow covered surface (lower left)

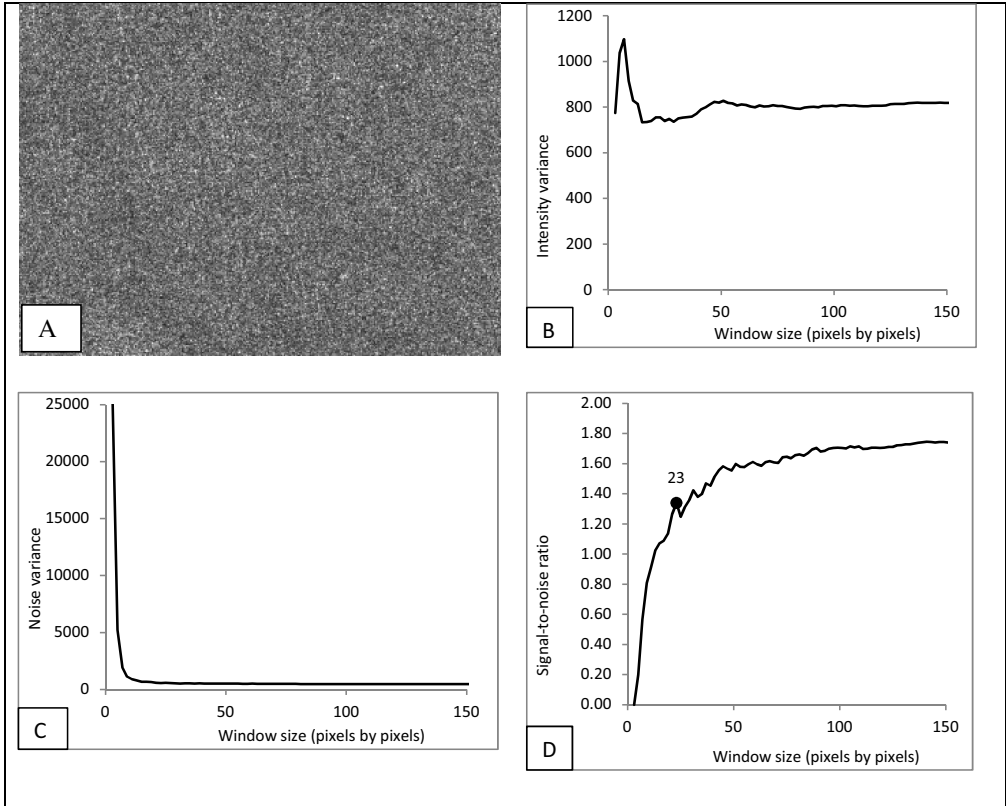


Fig. II-5 Image intensity variance (B), noise variance (C) and signal-to-noise ratio together with the first local maximum (D) as plotted against the window size for a high-resolution SAR image (A) of a glacier.

## II.2.2. Template size and cross-correlation coefficient

As stated, the most reliable disparity (displacement) estimate is the one with the least uncertainty of matching. The value of the NCC coefficient is a measure for the level of (un)certainty of the matching. Conventionally the value of NCC coefficient is used to compare the similarity of different consecutive templates in the search window to the reference template. Here, it is hypothesized that the variations of the NCC coefficients for the same central pixel but for different template sizes can be used to compare the certainty of the matching. Therefore, the relationship between the maximum NCC coefficient and template sizes is explicitly investigated. A Section of aerial images taken over rockglacier with 13 years apart were used. Using the older image as reference, the maximum NCC coefficients are computed for each  $\tau$  value ranging from 1 to a maximum size set by increasing  $\tau$  by steps of 1.

A number of points in the reference image are selected and NCC-based matching is performed using different  $\tau$  values. For each  $\tau$ , only the peak of the NCC coefficient and the position of the match are recorded. A typical example of the relationship between template size and the maximum correlation coefficient is presented in Fig. II-6 and summarized in the text that follows.

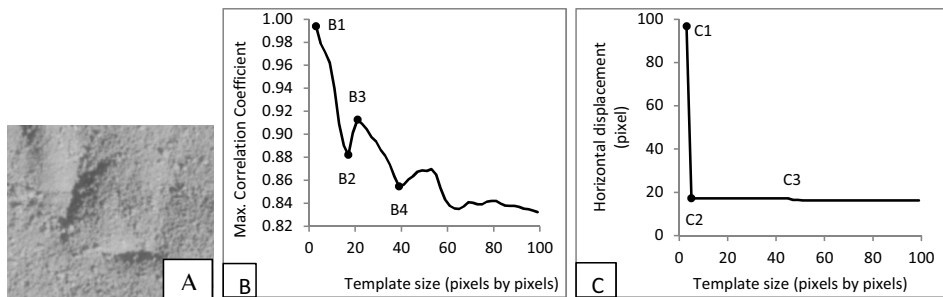


Fig. II-6 The relationship between template size and the maximum NCC coefficient (B) and the displacement estimates (C) for an image subset (A) that contains good signal variance

i) For small template sizes, the maximum NCC coefficient is very high (Fig. II-6B, point B1). It is likely that many exact matches can be found. The matches may include a true match, naturally existing duplicates and noise-related duplicates. Identifying the true match is therefore ambiguous. It is even difficult to distinguish the signal correlation from that of noise (Fig. II-7 A). The matching position is thus located randomly leading to an unreliable displacement estimate (Fig. II-6C, between C1 and C2). As the template size increases, the template will become more unique but still contains noise. The peak of the NCC coefficient will be reduced due to noise. As more and more pixels are included, the noises get suppressed and the peaks become clearer (Fig. II-7 B).

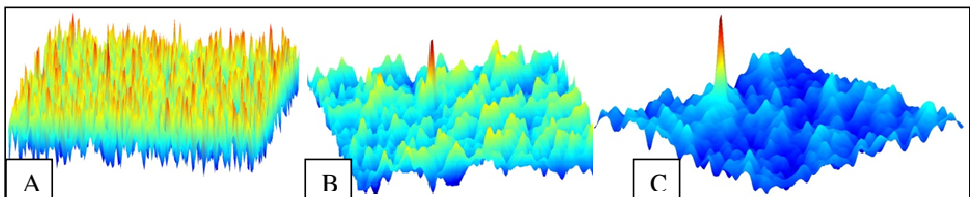


Fig. II-7 Typical NCC coefficient surfaces for template sizes of 7 pixels (A), 20 pixels (B) and 51 pixels (C) for search window size of 256 pixels

ii) After the noise is optimally suppressed, the correlation of the signal takes over. The maximum NCC coefficient increases again (Fig. II-6B between B2 and B3). It will then

reach a certain local peak at a certain template size (B3). This size is assumed to contain minimum geometric distortion and noise. Fig. II-6C shows that the matching position may get fixed already before the correlation attains this peak (C2). However, maximizing the correlation coefficient increases the certainty of the matching position. The actual displacement of 17.26 pixels is now correctly computed.

iii)The NCC coefficient then starts to decrease again after point B3 of Fig. II-6B. The decrease this time is related to the fact that additional pixels mean more source of dissimilarity as a result of increased geometric distortion. This decrease is proportional to the velocity gradient (deformation) within the template. When the displacement gradient increases, the correlation coefficient decreases until the gradient gets so high that the matching position shifts by a pixel. The correlation coefficient starts to increase again (Fig. II-6B B4). This time the correlation belongs more to the farther off entity than to the entities close to the central pixel. The matching position also shifts slightly changing the displacement magnitude (Fig. II-6C C3). The displacement is now underestimated to be 16.28 pixels due to averaging over the large template. Such shift is small compared to the mismatches due to ambiguity.

The relationship between the maximum NCC coefficient and the template size presented above is typical for features that contain sufficient signal variability. For shadows, water surfaces, snow, and other monotonous surfaces that lack adequate signal variability (at least for optical imagery), or for terrain Sections that are very unstable over time, the relationship is quite different. Such templates are usually mismatched or occluded (lack a match) due to the fact that they may no longer exist or may have changed pattern. Their matching position may thus not get fixed easily or at all (e.g. Fig. II-8).

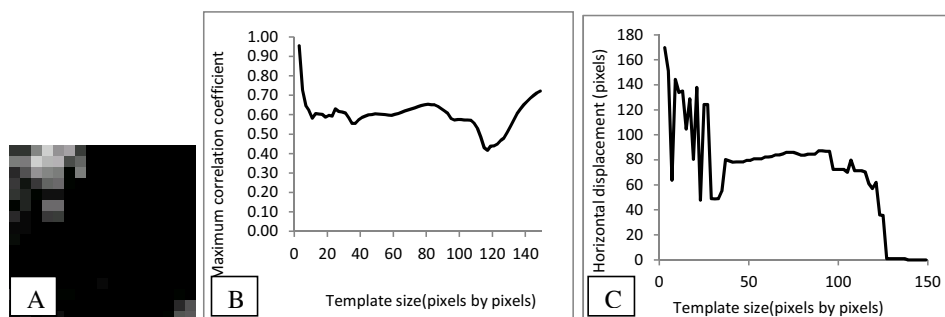


Fig. II-8 The relationship between template size and the maximum NCC coefficient (B) and the displacement estimates (C) for a feature in shadow (A) presented here as an example

In addition to noise and velocity gradients the ground pixel size has a role to play in the relationship between template size and NCC. High spatial resolution images enable to match smaller features and detect small disparity (displacement) enabling to deal with the problem of velocity gradient more elegantly. In low spatial resolution images, features are observed at different scale. Small features are hardly matched and small displacements cannot be detected (Debella-Gilo and Kääh, 2011). Besides, velocity gradients are harder to deal with. There can be velocity gradient even within a single pixel. Therefore, although NCC peaks can be observed at any spatial resolution, its precision and reliability is dependent on the resolution.

### **II.2.3. Signal-to-noise ratio and cross-correlation coefficient**

The relationship between SNR and template size can be used to identify unique entities with good information content and entities that lack such qualifications. Although matchable entities can be identified, there is no guarantee that these entities remain as they are geometrically and radiometrically. Therefore, using the size of the entity with optimum SNR as template size for matching may lead to mismatches as one of the following scenarios may happen due to the time lag between the images and different imaging conditions:

- The entity does not move or moves rigidly with limited level of noise in the image. In such cases, the template size at which the first local peak of the NCC coefficient is attained is the same as or smaller than the window size at which the first SNR peak is attained.
- The entity does not move or moves rigidly but the image is highly noisy. The size at which the first local peak of the NCC coefficient is attained will therefore be greater than the window size at which the first SNR peak is attained so that the noises are optimally suppressed.
- The entity disintegrates into smaller pieces or deforms significantly. In such cases, the optimum template size will be smaller than the window size at which the first SNR peak is attained. If the images are too noisy the matching may no longer be reliable.
- The entity is unrecognizably altered or disappears. In such cases, the optimum template size does not exist. The template should be excluded from the analysis.

## II.3. Methods

### II.3.1 Algorithm for locally adaptive template sizes

The scenarios stated in Section II.2.3 and discussions of Sections II.2.1 and II.2.2 help us design an algorithm which uses the SNR and the NCC peaks to identify matchable templates and determine their optimum sizes. Such an algorithm is presented in two steps in the following Sections.

#### II.3.1.1. Matching candidate selection using SNR

The relationship between SNR and window size described in Section II.2.1 indicates that for every entity the relationship between SNR and the size of the entity can be approximated by a polynomial function. Based on this relationship we can use Fermat's theorem to find the position of the first local maximum. Fermat's theorem states that the necessary condition for every local extremum (maximum or minimum) is that the function's derivative is zero at that point (Zlobec, 2009). Assume  $f(x)$  is a differentiable function and for a certain domain value  $x_0$ , the function decreases for  $x$  values just before  $x_0$  and increases for  $x$  values just after  $x_0$ . In other words, the derivative of  $f$  is positive as  $x$  gets close to  $x_0$  from the left and negative as  $x$  gets close to  $x_0$  from the right. Intuitively, and by Darboux's theorem (Olsen, 2004), there exists  $x_0$  where the derivative of  $f(x)$  is zero. At such  $x_0$  the function attains its local maximum. Since we do not have a continuous function relating SNR to the template size, we use its differencing ( $\Delta SNR$ ) over a unit of the template size ( $\tau$ ) and then find the  $\tau$  value where the difference changes from positive to negative. Additionally, at this  $\tau$  the signal variance has to exceed the noise variance, otherwise it would simply be matching noises.

$$\Delta SNR(\tau) = SNR(\tau) - SNR(\tau - 1) \quad \text{II-8}$$

The template size at which the SNR attains its local maximum ( $\tau_{opt}$ ) is then:

$$\tau_{opt} = \tau \quad \text{II-9}$$

with  $\tau$  such that:

$$\text{I. } \sigma^2(S) > \sigma^2(e)$$

- II.  $\Delta\text{SNR}(\tau - 1) > 0$ , and
- III.  $\Delta\text{SNR}(\tau + 1) < 0$ .
- IV. II and III imply  $\Delta\text{SNR}(\tau) = 0$ .

The algorithm is implemented as follows. For every  $\tau$  ranging from 1 to a certain value chosen based on the maximum acceptable ground template size, the SNR is computed. For every  $\tau$  greater than 1, the  $\Delta\text{SNR}$  is computed. The computation continues until the conditions of Eq. II-9) are satisfied at which point the computation stops and that  $\tau$  value (in fact  $2\tau + 1$ ) is used as the candidate window size. If it fails to satisfy the condition, the algorithm discards the entity and continues to the next central pixel.

### II.3.1.2. Optimization of the local template sizes

The behavior of the different features discussed in Section II.2.2 shows that for every image subset, there is a size at which the maximum NCC coefficient attains a first local peak and the position of the match is identified, unless it lacks true match. The variation of the maximum NCC coefficient ( $\rho_{\max}$ ) with template size approximates the shape of a polynomial function (Fig. II-6). Based on this, just like in Section II.3.1.1, we can use Fermat's theorem and differentiate the function  $\rho_{\max}$  over a unit of the template size ( $\tau$ ) and then find the value where the derivative changes from positive to negative (Eq. II-10 and II-11).

$$\Delta\rho_{\max}(\tau) = \rho_{\max}(\tau) - \rho_{\max}(\tau - 1) \quad \text{II-10}$$

The template size at which the maximum correlation coefficient attains its first local maximum ( $\tau_{\text{opt}}$ ) is then:

$$\tau_{\text{opt}} = \tau \quad \text{II-11}$$

with  $\tau$  such that:

- I.  $\Delta\rho_{\max}(\tau - 1) > 0$ , and
- II.  $\Delta\rho_{\max}(\tau + 1) < 0$ .
- III. I and II imply  $\Delta\rho_{\max}(\tau) = 0$ .

The first local peak found has to be checked whether it is attained at the optimum template size or noise-based template size. If it is at the optimum template size, the matching position is also fixed. This means that the matching position of the central pixel should not



change for template sizes greater than  $\tau_{\text{opt}}$  unless there is a full pixel shift in matching position. The matching position of the central pixel is expected to remain the same for template sizes starting from  $\tau_{\text{opt}}$  until the displacement gradient attains a full pixel. Increasing the template size until such point is reached only adds computational cost as full pixel displacement gradient may not be attained or may be obtained at very large template sizes. Therefore, iterating for 3 more template sizes (i.e. up to  $\tau = \tau_{\text{opt}}+3$ ) should suffice based on two assumptions. Firstly, this size difference is too large for chance-based (ambiguous) matching positions to remain the same for three consecutive template sizes. Secondly, it is too small for the displacement gradient to attain one full pixel in most slow-moving masses. Therefore, if the matching position does not change within that range, it is considered to be the true match. If it changes, it is an indication of randomness or ambiguity. To formalize this, let's assume that when the template size is  $\tau$ , the position of the matching central pixel is  $[X_\tau, Y_\tau]$ . If  $\tau$  is the optimum template size, Eqs. II-12 and II-13 should be true:

$$X_\tau = X_{\tau+1} = X_{\tau+2} = X_{\tau+3} \quad \text{II-12}$$

$$Y_\tau = Y_{\tau+1} = Y_{\tau+2} = Y_{\tau+3} \quad \text{II-13}$$

For every  $\tau$ , the  $\rho_{\text{max}}$ ,  $\Delta\rho_{\text{max}}$  and the matching positions are computed. The algorithm then checks if the conditions are fulfilled. If they are fulfilled,  $\tau$  is used for the optimum template size. If the conditions are not fulfilled within the given search range, it is assumed that the entity lacks a reliable match and the algorithm ignores the entity and moves to the next central pixel.

Iterating for all templates and from template sizes of 3 by 3 to the maximum size set for every template is computationally expensive. To limit this, the SNR-based matchable template identifier is used as follows: first, the iteration is done only for the central pixels identified by the SNR-based algorithm of Section II.3.1.1. Second, since the optimum template size is related to the SNR as explained in Section II.2.3, the iteration is done for template sizes ranging from half to twice the window size at which the first SNR peak is attained. The lower boundary is set to include all the features that might have moved with significant displacement gradient, and the higher limit is set to include candidates affected by high level of noise.

### II.3.2. Test and implementation of the algorithm

The here-developed algorithm is tested on modeled deformation image pairs with known displacement for each pixel. It is then implemented on real bi-temporal images of Earth surface mass movements. The algorithm's performance is evaluated in reference to the performances of various globally (i.e. image-wide) fixed template sizes.

#### II.3.2.1. Simulation of deformation and algorithm test

To model bi-temporal Earth surface mass displacement image, let's first clarify the theoretical assumptions of displacement and deformation in images:

- An entity at a certain location  $(x, y)$  has the intensity value  $f(x, y)$  in the reference image. This entity is displaced to a new location  $(x_1, y_1)$  and gets intensity value  $g(x_1, y_1)$  in the search image.
- The two intensity values are expected to be the same unless radiometric (sometimes referred to as photometric) distortion exists. The most common forms of radiometric distortion are shift (also called offset;  $\eta$ ), scaling (also called gain;  $\lambda$ ) and random noise ( $e$ ). Therefore, the transformation of the intensity values can be approximated as:

$$g(x_1, y_1) = \lambda f(x, y) + \eta + e \quad \text{II-14}$$

- The mode of displacement varies from simple translation (constant velocity) to a more complicated deformation that involves translation, rotation, shearing and scaling. For most mass movement types first order deformation is sufficient to approximate the relationship between the two locations within typical template sizes. Therefore, affine transformation with six parameters of the following form can approximate the relationship:

$$x_1 = a_1 + b_1x + c_1y \quad \text{II-15}$$

$$y_1 = a_2 + b_2x + c_2y \quad \text{II-16}$$

NCC measures the similarity between  $f(x, y)$  and  $g(x_1, y_1)$ . NCC is insensitive to both radiometric illumination and brightness (Nillius and Eklundh, 2002). Therefore, it is influenced only by the presence of random noise ( $e$ ) and the velocity gradients that deform the templates. This means, the NCC coefficient is expected to be high for  $e$ ,  $c_1$  and  $b_2$  values close or equal to 0 and for  $b_1$  and  $c_2$  values close or equal to 1. In fact, assumption of rigid translation means that all of these parameters are assumed to be so within a given template.

Therefore, to model Earth surface mass movements and investigate the influence of the factors independently, artificial displacement is introduced to a real image based on the above principles as follows: First, a Section of an aerial image covering a debris-free glacier with crevasses, and bedrock and debris surrounding the glacier is taken (Fig. II-9 A). More details on the image and site are given in Section II.3.2.2. First order affine transformation of Eqs. II-17 and II-18 are used to artificially model a deformed image of time 2. Note that only full-pixel displacements are allowed to avoid unnecessary image interpolation. The horizontal displacement magnitude in Euclidean distance is thus computed as in Eqs. II-19, II-20 and II-21. The displacement map of Fig. II-9 (B) is the result of this computation at integer pixel precision. Exploration of the computed displacement shows that the displacement magnitude coincidentally changes every 20 pixel in the x-direction and at variable but larger distances in the y-direction. No radiometric distortion or noise is introduced at this moment. The intensity value of a pixel is thus expected to remain the same although the pixel is moved to another location (Eq. II-22).

$$x_1 = \text{round}(10 + 0.97x + 0.001y) \quad \text{II-17}$$

$$y_1 = \text{round}(10 + 0.01x + 0.95y) \quad \text{II-18}$$

$$u = x - x_1 \quad \text{II-19}$$

$$v = y - y_1 \quad \text{II-20}$$

$$d = \sqrt{u^2 + v^2} \quad \text{II-21}$$

$$f(x, y) = g(x_1, y_1) \quad \text{II-22}$$

In the second case, the same displacement is modified by distortion of the image intensities by the addition of Gaussian random noise of mean 0 and variance 0.1 using the inbuilt MATLAB module “*imnoise*” in order to model random temporal changes in image intensities. Thus, the image of time 2 is not only a displaced version of the first image but also contaminated by Gaussian random noise. No radiometric gain or offset is included into the model as they are believed to have no effect on the NCC.

Now we have two pairs of images: one with just displacement and the other with displacement and additive Gaussian noise. Image matching is then applied on the two pairs of images using the NCC algorithm. First, different globally fixed template sizes ranging from 11 to 101 pixels (with 10 pixels interval) are used. Then, the here-developed locally adaptive algorithm is applied. The same search window size is used for all cases so that the comparison

is conducted under the same condition and no manual filtering was conducted in order to mimic full automation.

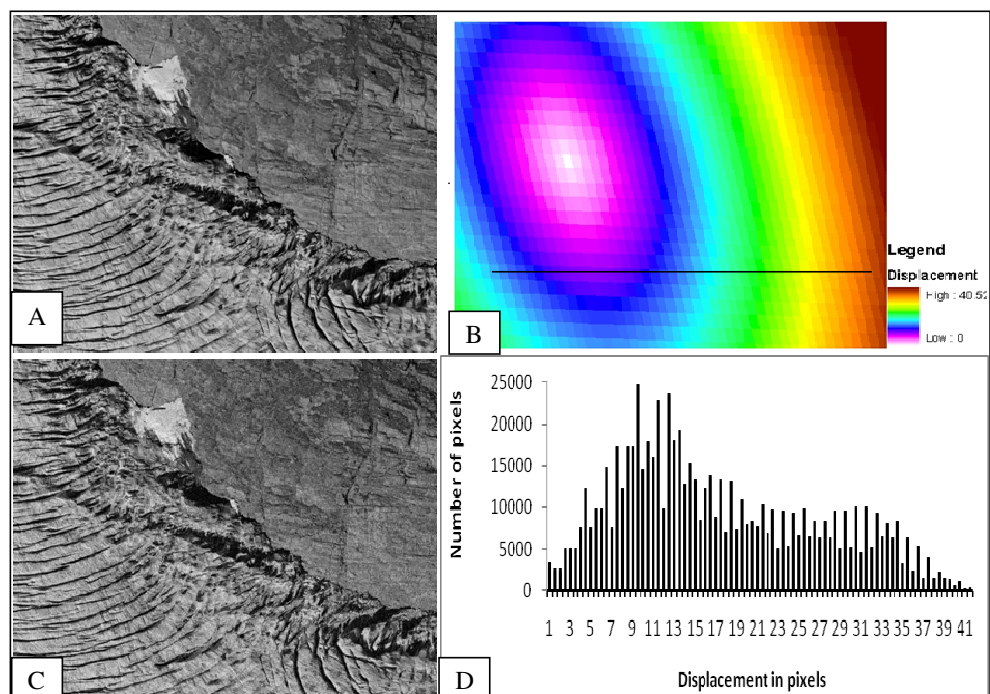


Fig. II-9 A segment of the test image of the crevassed Nigardsbreen glacier and its surroundings (A), the artificially created displacement magnitude for every pixel (B), the same image after getting displaced by B and after adding Gaussian noise of 0 mean and variance 0.1 (C), and the histogram of the displacement (D)

### II.3.2.2. Example data for real Earth surface mass movements

The algorithm is mainly applied to three types of bi-temporal images of glacier flow. This selection is governed by the aim to choose very different image types (aerial, satellite optical, radar), but on the same type of process in order to facilitate the comparison. Other mass movement types (Muragl rockglacier creep and Aletsch land sliding) have also been tested for which the description of dataset is found in (Debella-Gilo and Kääh, 2011) and the outcomes are only briefly reported here.

- 1) The first image pair is a Section from panchromatic aerial images over the Nigardsbreen glacier in Southern Norway (lat 61.68°N, lon 7.20°E). The images were acquired on August 19 and 29, 2001 within the EU Glaciorisk project (see Fig. II-9). The images were orthorectified using photogrammetric stereo pairs and automatic DEM extraction of the two dates. The ground resolution of the orthoimages is 0.3 m. Surface changes within the

very short time period of 10 days were very small. More details on the images and on their glaciological analysis can be found in (Wangensteen et al., 2006).

- 2) The second image pair is composed of a section of synthetic aperture radar (SAR) intensity images over a Section of Kronebreen glacier on Svalbard, Norwegian Arctic (lat 78.87°N, lon 12.5°E; Fig. II-10 left). Note that the image used here is in original SAR geometry and appears therefore mirrored with respect to map geometry. The noise level (radar speckle) of SAR images is much higher than that of optical images. Both images used here are taken from Radarsat-2 in high-resolution mode (ultrafine beam) in HH polarization, with a ground resolution of approximately 3 by 3 m. The first image is taken on April 06, 2009 while the second is taken on April 30, 2009. Both images have been acquired from the same orbit so that no orthorectification was required but a polynomial adjustment was sufficient to reach sub-pixel accuracy co-registration between both images. The latter co-registration was performed using the GAMMA radar software. The radar images are courtesy of Radarsat, the Norwegian Space Center and KSAT. More information on the flow field of Kronebreen can be found in (Kääb et al., 2005).

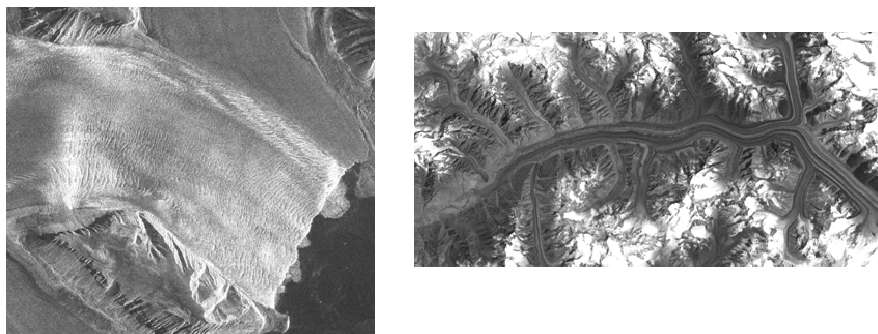


Fig. II-10 A Section of the SAR image of the Kronebreen taken on April 06, 2009 (left) and a Section of a Landsat 7 panchromatic image over the Baltoro Glacier taken on June 16, 2000 (right)

- 3) The third image pair is composed of Landsat7 ETM+ panchromatic images with 15 m resolution captured on June 16, 2000 and July 27, 2001 over a part of the Karakoram Mountains of Pakistan (Landsat7 path 148, row 35). Here, a small Section over the Baltoro Glacier is used (lat 35.74°N, lon 76.43°E; Fig. II-10 right). More detailed description of the glacier and its dynamics is found in Copland et al. (2009). Both images were acquired and orthorectified by the US Geological Survey (L1T level). The terrain correction and the fact that both images were acquired from the same orbit path minimize

differential topographic distortions within the image pair. Landsat7 ETM+ pan data are known to have a noise level of several digital numbers (Haug et al., 2010).

### **II.3.3. Performance evaluation of the algorithm**

#### **I.3.3.1. Evaluating the test images using displacement data**

Every pixel in the two test image pairs has a known displacement value which can be computed from the transformation equation used for the modeling. The accuracy here is therefore the straight forward comparison of the actual displacement and the estimated displacement. A few different statistical parameters could be used to measure the accuracy of the estimation: namely, the mean of the differences between the actual and estimated displacements (mean bias), the mean absolute error (MAE), and the root mean squared error (RMSE). Since mean bias measures only the systematic bias of the estimation and the RMSE is too sensitive to extreme values such as mismatches due to the squaring (Willmott and Matsuura, 2005), the MAE is found appropriate. MAE (Eq. II-23) is the mean of the absolute values of the difference between the estimated displacement ( $d_i$ ) and the actual displacement ( $d_{oi}$ ). Every deviation is accounted with its magnitude at the scale of the measurement. Best estimate of displacement is, therefore, the one with MAE equal or close to zero. As the actual displacements in the real images are not known, only the test images can be evaluated using this approach.

$$MAE = \frac{\sum_1^n |d_i - d_{oi}|}{n} \quad \text{II-23}$$

#### **I.3.3.2. Evaluating the real multi-temporal images using intensity data**

In real multi-temporal images displacement-based assessment procedure is not possible as true displacement data is usually not available. Subjective evaluation approaches such as visualization of the velocity fields and looking for outlying displacement vectors can be used at first glance. Such approaches can identify most of the mismatches caused by ambiguity as they often result in observable gross errors. However, misrepresentation errors (i.e. errors due to displacement gradient within the template) can hardly be detected visually. Therefore, a self-relying quantitative approach is devised. It is based on the assumption that, even if displaced, Earth surface entities retain their radiometric characteristics over the temporal

baseline of the image acquisition. This retention of the radiometric characteristics can be measured by the correlation coefficient as outlined below.

Assume a pixel  $(x, y)$  of the reference image with intensity value of  $f(x, y)$  is displaced by  $u$  and  $v$  in  $x$  and  $y$  directions respectively and located at  $(x_I, y_I)$  in the search image with new intensity value  $g(x_I, y_I)$ . After finding the matching positions, every pixel in the deformed (second) image is moved back to its original location,  $(x, y)$ , taking the intensity value of the search image (Eq. II-24). This back-simulates the reference (first) image using the imaging condition of the search (or second) image registering each pixel of the second image back to the first image. Theoretically, if the displacement is perfectly estimated, the imaging conditions are equal and there is no temporal surface changes,  $f(x, y)$  is expected to be equal to  $g(x_I, y_I)$  which is here equal to  $h(x, y)$ . However, in reality there can be radiometric gain ( $\lambda$ ), offset ( $\eta$ ) and noise ( $e$ ). For every pixel  $(x, y)$  in a reference template, the new intensity values,  $h(x, y)$ , can be reconstructed as:

$$h(x, y) = g(x + u, y + v) = \lambda f(x, y) + \eta + e \quad \text{II-24}$$

The algorithm that produces the least difference between  $f(x, y)$  and  $h(x, y)$  is considered to be the best performing algorithm. The computed difference is cumulative of the systematic offset, gain and random radiometric deviations. Consequently, simple differencing cannot be a good parameter of the evaluation. The correlation coefficient is a more suiting parameter. Here, the global correlation coefficient ( $\rho$ ) between the reference image,  $f(x, y)$ , and the reconstructed image,  $h(x, y)$ , is computed. The  $\rho$  can then be used as a measure of the SNR between the images (Thong et al., 2001). If  $\rho$  is the correlation coefficient between the two images, the SNR is then given as:

$$SNR = \frac{\rho}{1-\rho} \quad \text{II-25}$$

Assume the initial correlation coefficient between the reference image and the search image before the matching is  $\rho_i$ .  $\rho_i$ , implicitly  $SNR_i$ , is typically low in cases where there is significant change in geometry (deformation) and surface condition (noise). Estimating the displacement and reconstructing the image is thus expected to improve the correlation coefficient, and the SNR. How much the SNR improves depends on how successful the image matching technique is. The success of our locally adaptive algorithm under different imaging and surface conditions can therefore be evaluated based on this parameter. If we assume  $SNR_f$  to be the SNR between the reference image and the reconstructed image after matching using

globally fixed template size, the gain ( $SNR_{gf}$ ) can be computed as in Eq. II-26. Likewise, if we assume  $SNR_a$  to be the SNR between the reference image and the reconstructed image after matching using locally adaptive template sizes, the gain ( $SNR_{ga}$ ) can be computed as in Eq. II-27).

$$SNR_{gf} = SNR_f - SNR_i \quad \text{II-26}$$

$$SNR_{ga} = SNR_a - SNR_i \quad \text{II-27}$$

The relative advantage of the locally adaptive template sizes over the globally fixed ones can then be quantified as in Eq. II-28. Here, 1 means equal performance; values below 1 indicate the fixed templates performing better; while, above 1 indicates better performance of the adaptive approach by that much factor. This is computed against different globally fixed template sizes for different Earth surface mass movement types and for different imagery.

$$Relative\ advantage = \frac{SNR_{ga}}{SNR_{gf}} \quad \text{II-28}$$

## II.4. Results

### II.4.1. Performance of the algorithm on the test images

#### II.4.1.1. Displacement-based evaluation

Fig. II-11 (left) shows the mean absolute error of the estimated displacement ( $MAE_d$  hereafter) plotted against the template size for the noise-free test image pair. When the globally fixed templates are too small (less than 11 by 11 pixels), there are mismatches due to ambiguity that lead to erroneous estimation of displacement increasing the  $MAE_d$ . The lowest  $MAE_d$  (0.18 pixel for this case) is attained at template size of 11 pixels. The  $MAE_d$  then increases gradually due to the displacement gradient which increases with template size.

Adaptively optimizing the template size for each location using the here-presented algorithm increases the accuracy, removing errors of ambiguity and velocity gradient (Fig. II-11). The algorithm produces  $MAE_d$  of 0.38 pixels which is a little higher than that of the best performing globally fixed template size. The algorithm reduces  $MAE_d$  of the globally fixed template size of 101 pixels (1.13 pixels MAE) by 66% and that of the ambiguous 5



pixels (3.7 pixels MAE) by 90%. Notice that due to the linear deformation the  $MAE_d$  of the globally fixed template size increases linearly with the template size. This is an evidence of the relationship between velocity gradient (which is by design linearly related to the template size) and  $MAE_d$ .

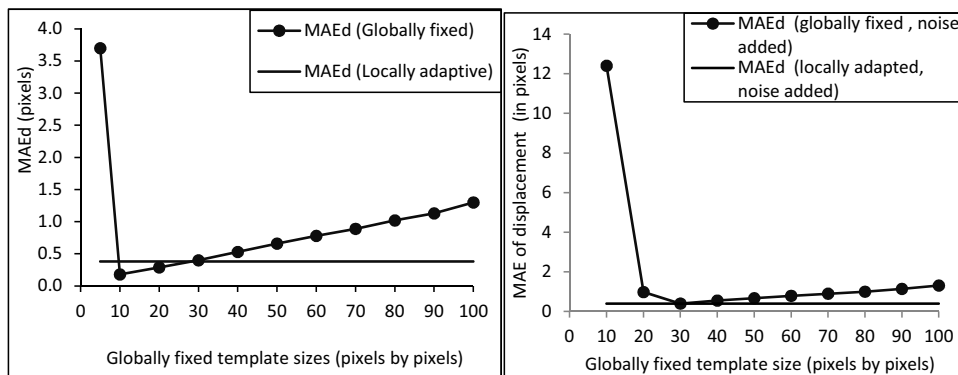


Fig. II-11. Mean absolute error of displacement ( $MAE_d$ ) of the globally fixed template sizes (dotted line) and the locally adaptive algorithm (horizontal line) for the noise-free (left) and noisy (right) test images

The presence of Gaussian noise of zero mean and variance 0.1 significantly increases the  $MAE_d$  of the globally fixed small templates (Fig. II-11, right). Globally fixed template sizes of 11 pixels now produce very high  $MAE_d$  (12.2 pixels). The lowest  $MAE_d$  (0.41 pixels) is now attained at template size of 31 pixels (dotted curve), not 11 pixels as before. For globally fixed template sizes greater than 31 pixels, both the noisy and noise-free test images perform alike. The locally adaptive algorithm actually registered the lowest  $MAE_d$  (0.40 pixels) which is about 96% reduction from that of 11 pixels. The mean of the template size of the locally adaptive algorithm is about 21 pixels, which is the template size at which the displacement gradient attains one full pixel (Fig. II-12D). The optimum template size is smaller for areas with good signal contrast and larger for low signal contrast areas. Most of them range between 11 and 35 pixels as can be seen from the histogram.

The results presented so far for both the noisy and the noise-free test images are based on combined errors of both mismatches and misrepresentations. Table II-1 presents the displacement statistics for the central pixels for a globally fixed small (11 pixels), large (61 pixels) and the locally adapted template sizes for the noisy test image. The table clearly shows that the locally adaptive algorithm registered the lowest  $MAE_d$ . Besides, its mean and standard

deviation of the estimated displacement is much closer to the actual one as compared to the two globally fixed template sizes showing better performance in dense matching as well.

Table II-1. Displacement statistics for the small, large and locally adapted template sizes for the central pixel of their respective templates of the noisy test image.

Statistic	Actual data	61 pixels	11 pixel	Locally adapted
Minimum	0	0	1	0
Maximum	37	35.90	96.88	36.67
Mean	16.04	15.17 ( <b>1.76</b> ) <sup>a</sup>	27.62 ( <b>7.49</b> ) <sup>a</sup>	16.05 ( <b>0.65</b> ) <sup>a</sup>
Standard deviation	9.18	8.84	22.90	9.16

<sup>a</sup>The numbers in the brackets are the corresponding MAE<sub>d</sub>. Notice that by using the locally adaptive algorithm, the MAE<sub>d</sub> of the large template size is reduced by about 63% while that of the small template size is reduced by about 91%.

The displacement vectors of Fig. II-12 show that when small templates are used the mismatching vectors can easily be visualized. However, errors of misrepresentation when using large template size cannot be detected visually. The vectors of the locally adaptive algorithm are similar to that of the large template sizes except the absence of vectors in areas which lacked good SNR maxima or correlation maxima.

The spatial distribution of the errors is also significantly important. Analyzing error data along a horizontal transect that passes through central pixels of a number of templates (transect depicted in Fig. II-9 B) reveals interesting result. Fig. II-13 shows the displacement magnitude (A), absolute horizontal displacement gradient (B), the absolute error of the displacement estimation for the fixed template sizes of 101 by 101 pixels (C) and 5 by 5 pixels (D), and for the locally adaptive template sizes (E) along the transect. The error of the globally fixed template sizes of 101 pixels is systematically related to the displacement gradient. The displacement of the test image changes horizontally by a pixel every 20 pixels as stated above. Likewise, the displacement estimation error of the globally fixed large templates changes horizontally every 20 pixels ranging from zero (close to the template center) to many pixels at the template peripheries depending on the displacement gradient and the template size. The situation with small template sizes is different. The random mismatches created due to ambiguity lead to matching error of the entire template including the central pixel. They often end up far away from the true match overestimating the displacement. The only limit to the overestimation is the extent of the search area. The use of the locally adaptive

algorithm removes much of the error (Fig. II-13 E). Notice the magnitudes of the absolute errors of the three cases for comparison.

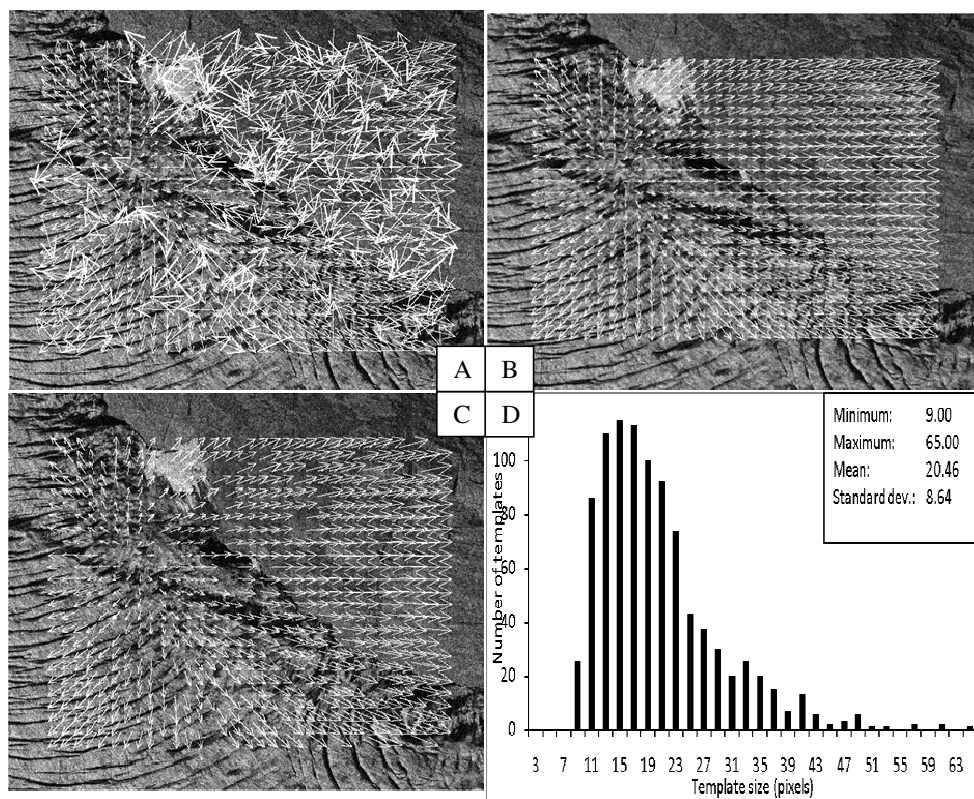


Fig. II-12 . Displacement vectors computed using globally fixed template sizes of 11 pixels (A), 61 pixels (B) and the locally adaptive algorithm (C) together with the histogram of the template sizes of the locally adaptive algorithm (D) for the noisy test image.

#### II.4.1.1. Intensity-based evaluation

Due to deformation there is low initial global correlation coefficient between the reference image and the original noise-free test image (Fig. II-14, left, dashed line). The correlation coefficient between the reference and the reconstructed image after matching using the globally fixed template size (dotted line) is much higher. Globally fixed template sizes below 21 pixels produce the best reconstruction. However, too small template sizes (e.g. 5 pixels) suffer from ambiguity due to insufficient signal variance. As the template size increases over 21 pixels, the performance of the reconstruction decreases due to the misrepresentation error resulting from the velocity gradient within the templates. The locally adaptive algorithm

seems to have effectively removed the problems of misrepresentation as its performance is comparable to that of the globally fixed size of 31 pixels (smooth line). The reason why it could not improve the correlation further is because, as stated above, that in some cases it uses large template sizes to maximize both the SNR and NCC coefficient allowing some errors of misrepresentation.

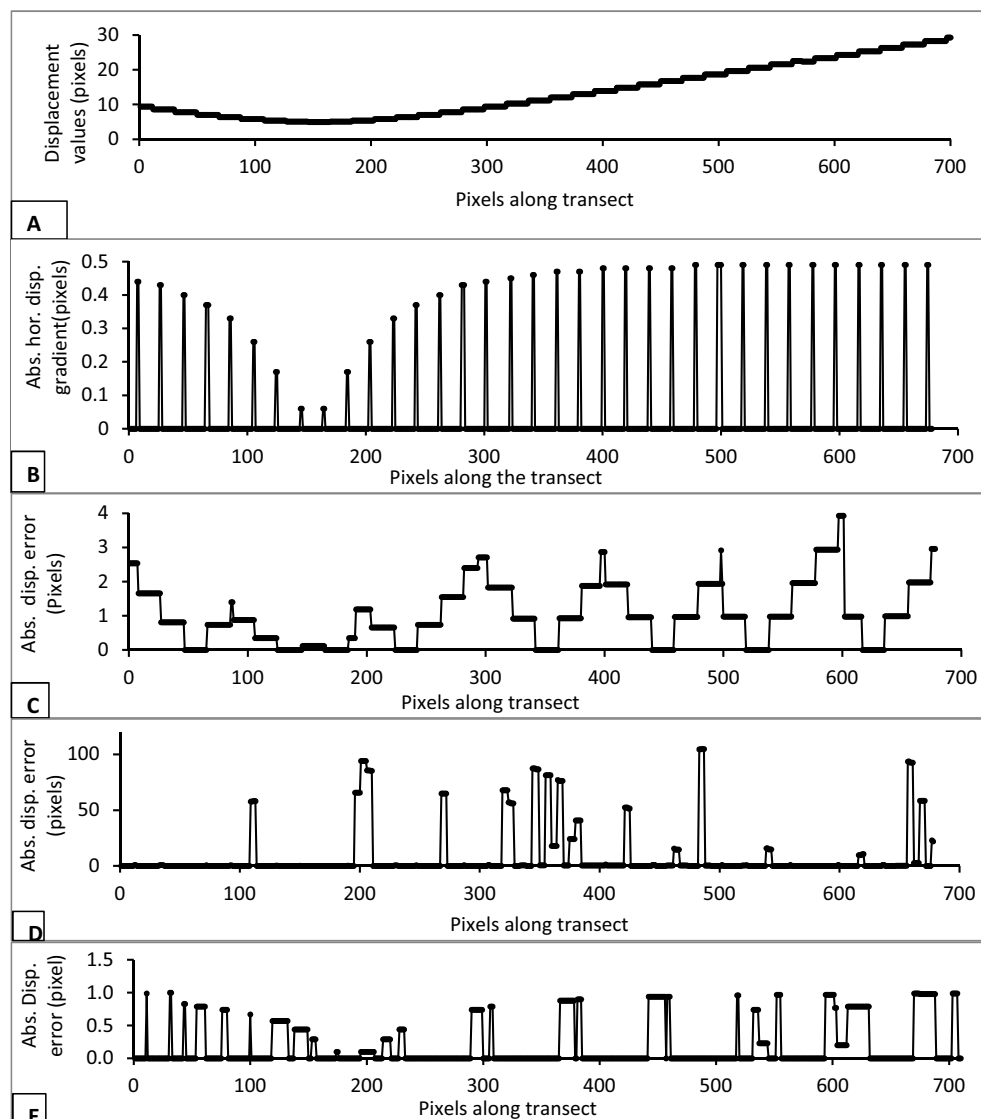


Fig. II-13 Displacement magnitude (A), absolute horizontal displacement gradient (B) absolute displacement error in pixels for the globally fixed template sizes of 101 by 101 pixels (C) and 5 by 5 pixels (D) and the locally adapted template sizes (E) along a horizontal transect that passes through template centers of the noise-free test images

For the test images with Gaussian noise, there is overall reduction of the global correlation coefficients (Fig. II-14 right). Additionally, the small templates now perform much poorer due to noise. The  $\rho$  first increases with template size up to about 21 pixels and then decreases again. Here, the locally adaptive algorithm performs better than that of the globally fixed template size of even 21 pixels proving that locally adapting the template sizes is more important in cases where there is high level of both noise and velocity gradient. The similarity between the corresponding curves of Fig. II-11 and Fig. II-14 shows that correlation-based evaluation can be used as a proxy for displacement-based evaluation. Once the ambiguity issue is resolved, the decrease in the reconstruction accuracy is linearly related to the template size due to the linear deformation (Fig. II-14).

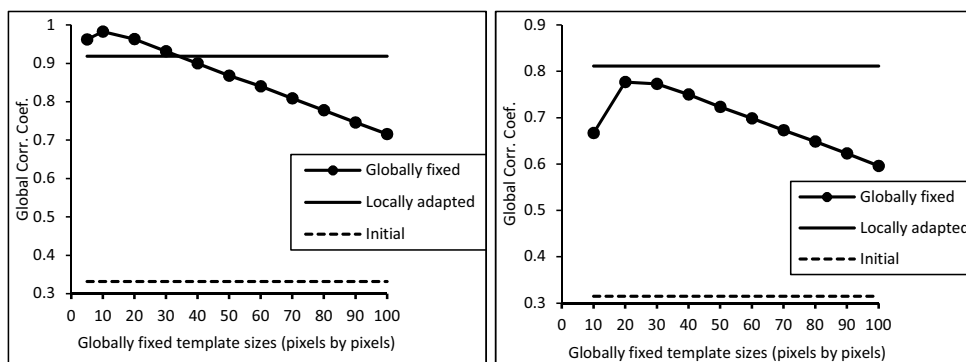


Fig. II-14. Global correlation coefficients between the original reference image and the search image before (dashed horizontal lines), after reconstructing using the globally fixed (dotted lines) and the locally adapted (smooth horizontal lines) template sizes for the noise-free (left) and the noisy (right) test images

The result of the test images reveals some interesting points. First, when estimating horizontal displacements from repeat images, the locally adaptive algorithm performs better than large globally fixed template sizes in cases of noise free images with significant deformation, and better than all globally fixed template sizes in cases where both significant noise and deformation are involved. Secondly, analysis on the test image showed that better reconstruction correlated well with higher displacement estimation accuracy. The test has therefore laid the ground for implementation of the algorithm on real multi-temporal images.

### II.4.3. Performance of the algorithms on the multi-temporal images

The performance of the algorithm on the bi-temporal images of glacier flow is consistent with that of the test images. For the Nigardsbreen aerial image, the initial global correlation coefficient is very low (0.2). Reconstructing the images after matching raised the correlation coefficient highly (Fig. II-15). Due to the lower noise content and the high signal contrast, template sizes of 21 to 31 pixels produce good reconstructions. The performance of the adaptive algorithm here is comparable to that of the noise-free test images. The explanation is that the Nigardsbreen aerial images are least affected by noise due to the short temporal baseline between the two image acquisitions (10 days). The image Section used is characterized by good intensity contrast due to the crevasses. The image covers mainly the glacier with a smaller area of stable ground.

The displacement vectors, computed using the adaptive algorithm, are presented in Fig. II-16. A limited number of outlying vectors are observed. The stable ground is almost perfectly identified with the absence of any moving template as can be seen on the northern part of the figure. The histogram of the template sizes (Fig. II-17) is skewed to the right indicating that most of the templates have small optimum sizes due to the low level of noise with limited geometric distortion.

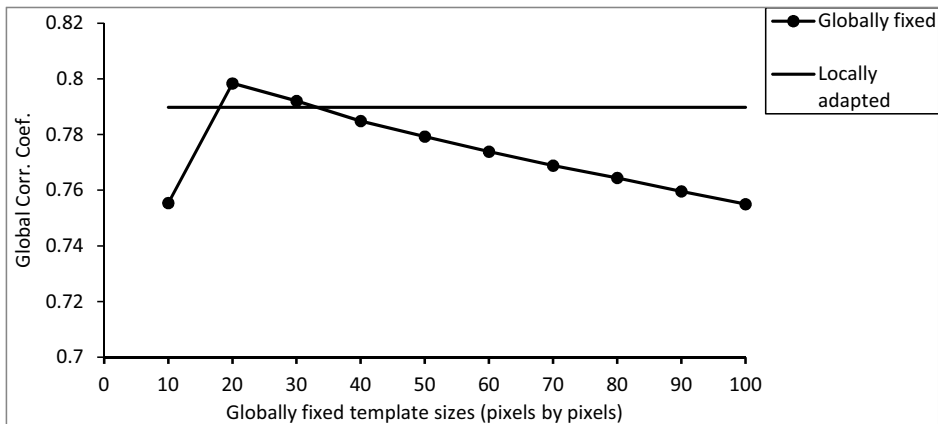


Fig. II-15 Global correlation coefficients between the original reference image and the search image after reconstructing using the globally fixed template sizes (dotted line) and the locally adaptive algorithm (smooth line) for the aerial images of the Nigardsbreen glacier.

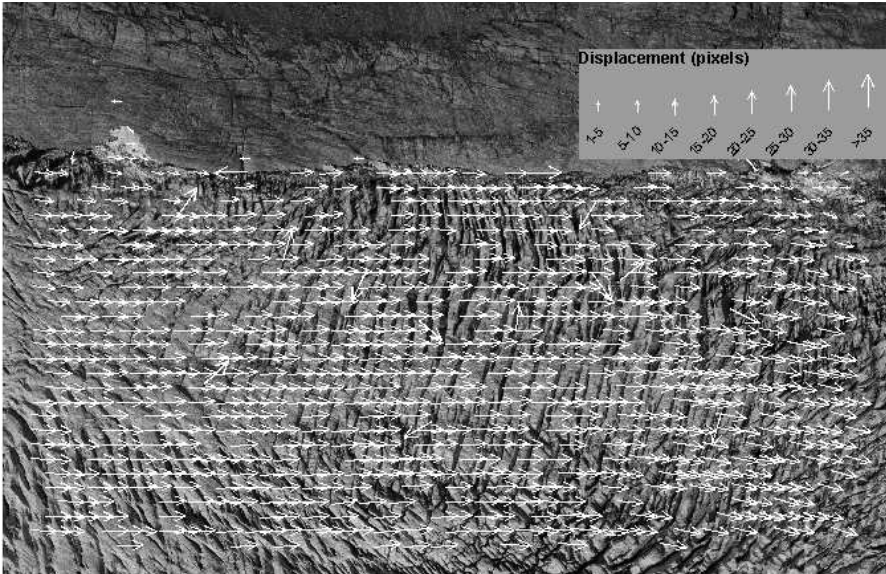


Fig. II-16 Displacement vectors of the Nigardsbreen glacier as computed from the bi-temporal aerial images using the locally adaptive algorithm.

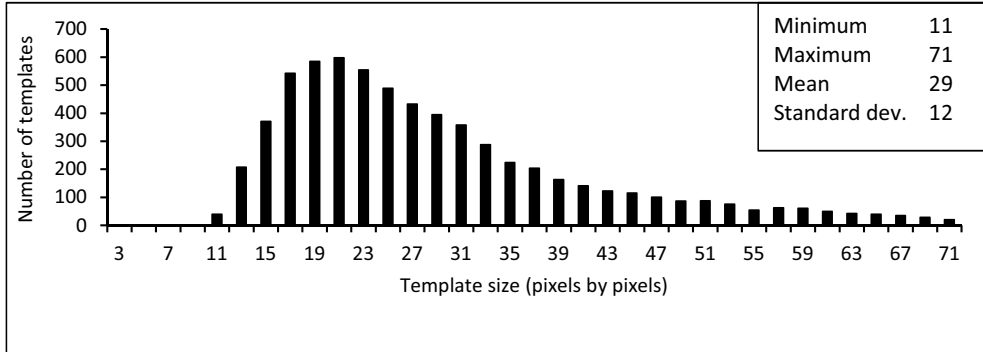


Fig. II-17 Histogram of the template sizes as computed by the adaptive algorithm for the Nigardsbreen glacier aerial images.

In the case of the Landsat panchromatic images over the Baltoro Glacier, the initial correlation itself is already high due to the large percentage of stable ground and the presence of white monotonous snowy surfaces in the scene (Fig. II-18). Matching with globally fixed small template sizes (11 pixels) lowered the correlation coefficient of the reconstruction even below the initial. That can be ascribed to a number of reasons. First, the temporal baseline (about one year) is large for a dynamic landform (glacier). Second, the noise level of Landsat7

ETM+ pan images is known to be high (Haug et al., 2010). Third, the spatial resolution of the image (15 m) is low. Matching errors of even one pixel are able to create a large intensity difference. Two neighboring pixels have a greater chance to cover two different surface features. Fourth, the study area includes monotonous features such as bright snow and gray glacier ice lacking good contrast over short distances. Due to these reasons, small template sizes do not correctly match even the stable ground. As can be seen from the Fig. II-19, the performance of the matching with globally fixed template sizes attains its peak at around 26 pixels. At larger template sizes the reconstruction accuracy is significantly lowered again. Large template sizes translate into large ground areas in such low resolution images, leading to comparably high velocity gradients in the templates especially due to the fact that the glacier studied is fast moving with varying velocities. The reconstruction accuracy of globally fixed template sizes greater than 60 pixels (which corresponds to a large ground distance of over 900 m) is even lower than the initial correlation coefficient between the two original images. In such low resolution images, large template sizes further distort the image rather than reconstruct it.

The histogram of the template sizes shows that the distribution is skewed to the right indicating that most optimum templates have in fact small sizes (Fig. II-19). The large template sizes are obtained on stable monotonous (bright or dark) surfaces which lack enough SNR over short distance.

Fig. II-20 presents displacement vectors of the Baltoro Glacier as computed using the locally adaptive algorithm. The figure shows both the strengths and the weaknesses of the algorithm. On the one hand, the fact that the algorithm could exclude most of the monotonous (dark and bright) regions from the matching, and that the stable areas are mainly correctly identified as stable, shows that the algorithm performs well even in such low spatial resolution images of low contrast. On the other hand, one can observe erroneous vectors especially at the transition between shadows and bright regions. These transitions create edge-like borders which make them pass the requirements of the algorithm. The flowing glacier stream is however very clearly identified without any manual filtering.



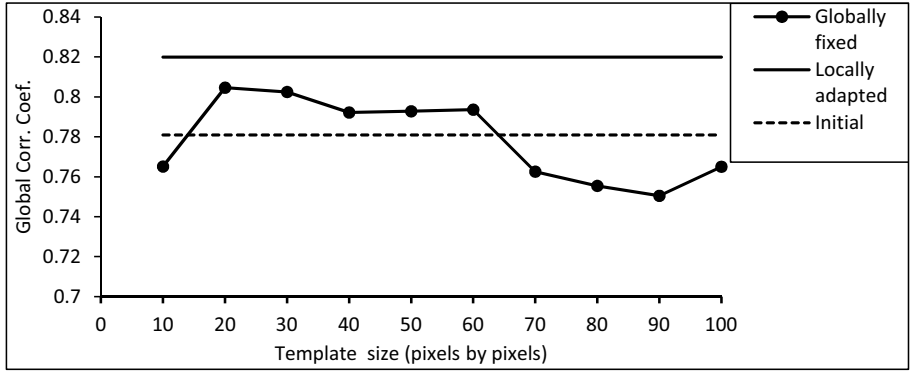


Fig. II-18 Global correlation coefficients between the original reference image and the target image before (dashed line), after reconstructing using the globally fixed template sizes (dotted line) and the locally adaptive algorithm (smooth line) for the Landsat image Section over the Baltoro glacier

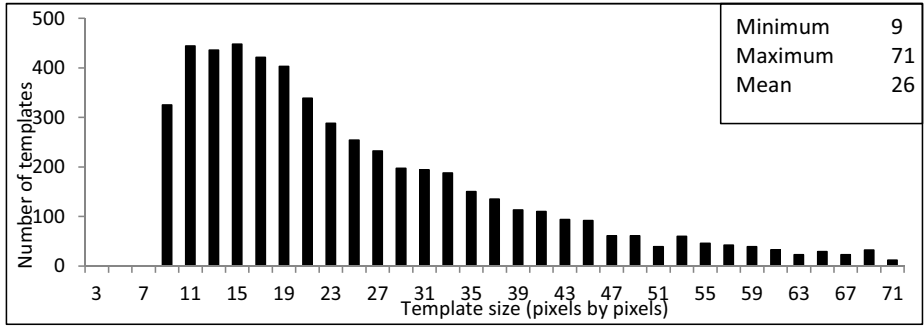


Fig. II-19 Histogram of the template sizes as computed by the adaptive algorithm for the Baltoro Glacier

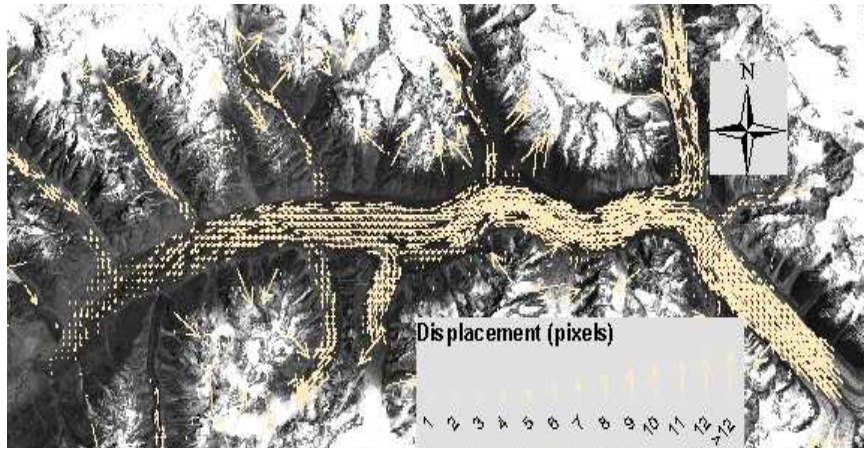


Fig. II-20 Displacement vectors on the Baltoro Glacier as computed from the bi-temporal Landsat panchromatic images using the locally adaptive algorithm

Fig. II-21 shows that for the SAR images at very small template sizes the matching is so noisy that the reconstruction itself becomes random. Large templates could not optimally remove the influences of noise. The adaptive algorithm thus produces better reconstruction than all the globally fixed template sizes used. However, the number of discarded templates for lacking an acceptable level of SNR is, not surprisingly, high in this image pair. The displacement vectors have a lot of gaps in those areas (Fig. II-23). The algorithm manages to exclude much of the low signal areas such as water surfaces at the lower right part of the image. The stable ground is also clearly identified by the absence of moving templates. SAR intensity images are well known to be very noisy due to radar speckle. Matching such noisy images using area-based spatial domain image matching is a daunting task. Unless the template size is large and temporal baseline is small, reliable displacement estimates are unlikely to be achieved. If severe deformation is involved, even large templates do not produce reliable estimates. Usually, intensive manual filtering is required to arrive at reliable displacement vectors. The algorithm here however produces few observable mismatches reducing such manual tasks and its heuristic impact on the reliability.

The mean template size (35 pixels) of this image is high due to the high noise level (Fig. II-22) compared to that of the aerial image of Nigardsbreen (29 pixels) and the Landsat Image of Baltoro glacier (26 pixels). The relatively smaller template size (in pixels) of the Landsat image over Baltoro glacier is ascribed to its low spatial resolution which indicates large ground template size and necessitates minimization of the projective distortion. The histograms are skewed to the right in all of the cases due to the presence of some features requiring large template size to maximize their SNR. If the iteration limit of the window size is reduced, the tails of the histogram would be shortened as such features will be excluded.

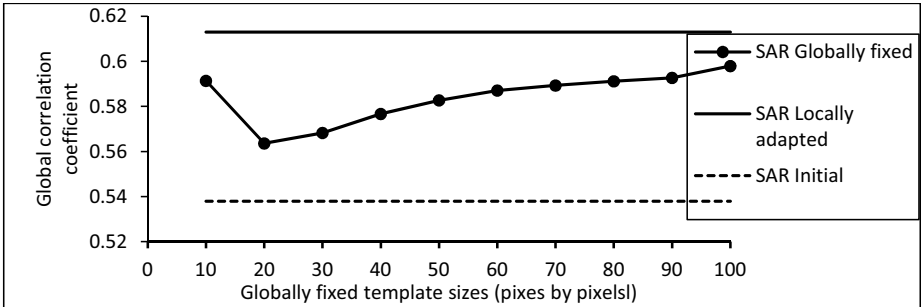


Fig. II-21. Global correlation coefficients between the original reference image and the target image before (dashed line), after reconstructing using the globally fixed template sizes (dotted line) and the locally adaptive algorithm (smooth line) for the SAR image pair over Kronebreen, Svalbard.

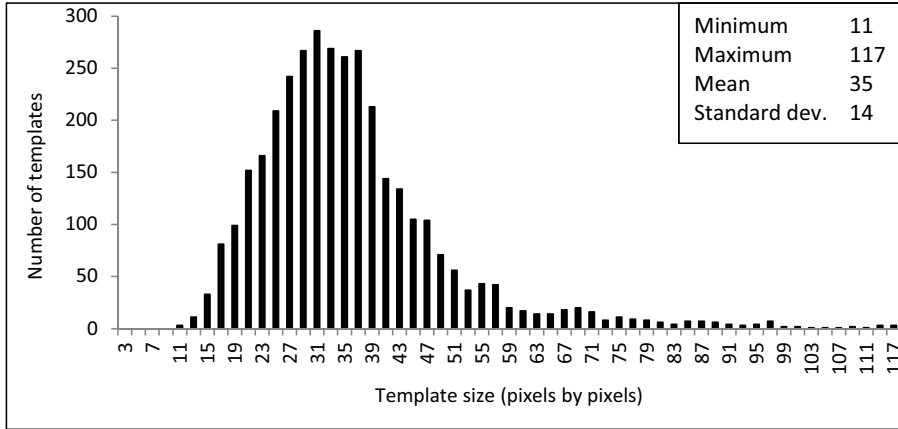


Fig. II-22 Histogram of the template sizes as computed by the adaptive algorithm for the Kronebreen glacier

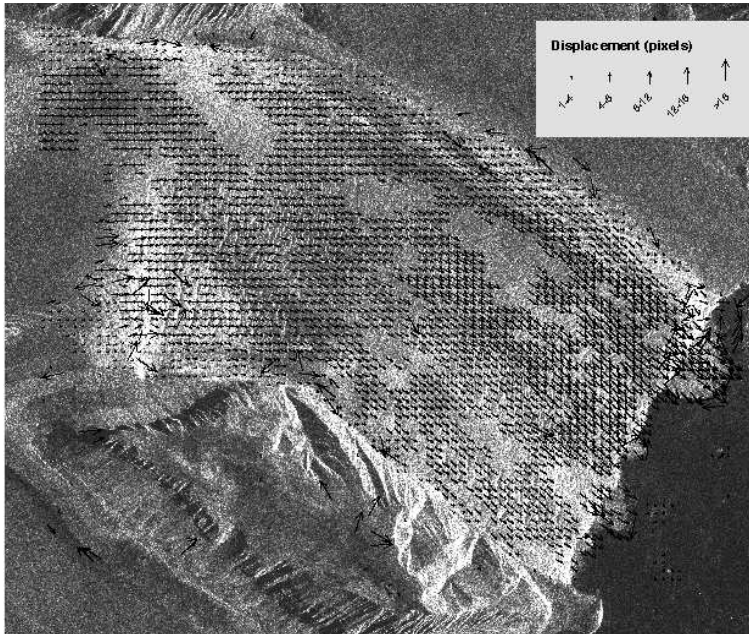


Fig. II-23 Displacement vectors of the Kronebreen glacier as computed from the bi-temporal SAR images using the locally adaptive algorithm.

#### **II.4.4. Relative advantage of the adaptive algorithm over globally fixed template sizes**

For every image pair, relative advantage varies with the size of the globally fixed template size it is compared with (Fig. II-24). In general, the algorithm registers better performance relative to small and large globally fixed template sizes. Although in most cases the gain in SNR is twice that of the globally fixed template sizes, it can reach over four times compared with very small and very large template sizes.

For the aerial image over Nigardsbreen glacier the lowest relative advantage is registered compared to the other image pairs. The reasons for this partly explain that of the others as well. The image pair over the Nigardsbreen is a high resolution (0.3 m) aerial image pair of short temporal baseline (10 days) over crevassed glacier with, thus, high signal contrast and little stable ground included. Therefore, it is relatively less error prone whether one uses relatively small (e.g. 21 pixels) or large (e.g. 61 pixels) template sizes. All the other images have either lower spatial resolutions, or larger temporal baselines, or large velocity gradients, or lower contrast, or combinations of these.

The algorithm performs much similarly on the Muragl rockglacier and the Aletsch rockslide images. These aerial images have high spatial resolution (0.2 meter), but large temporal baselines (13 years for the rockglacier and 30 years for the rockslide). For this group, the relative advantage of using locally adaptive template size decreases with increasing template size of up to 81 pixels, which is not too large in metric size but can suppress noises. For the SAR image the relative advantage continues to decrease with the increasing globally fixed template size. The image pairs contain a noise level so high that even large template sizes do not effectively suppress it. The locally adaptive algorithm is however more advantageous in all of the three cases.

The Landsat image pair over the Baltoro glacier stands out because the image pair is different from the others in its spatial resolution. This image is most sensitive to changes in template size as single pixel translates into large ground area. The advantage of using locally adaptive template size over large and small globally fixed template sizes is therefore well pronounced in this case. Although the template sizes are represented in pixels here, the ground size they represent varies with the spatial resolution of the images. The differences in the relative advantages presented in the figure are results of the combined effects of temporal baseline, spatial resolution, sensor type and surface type.

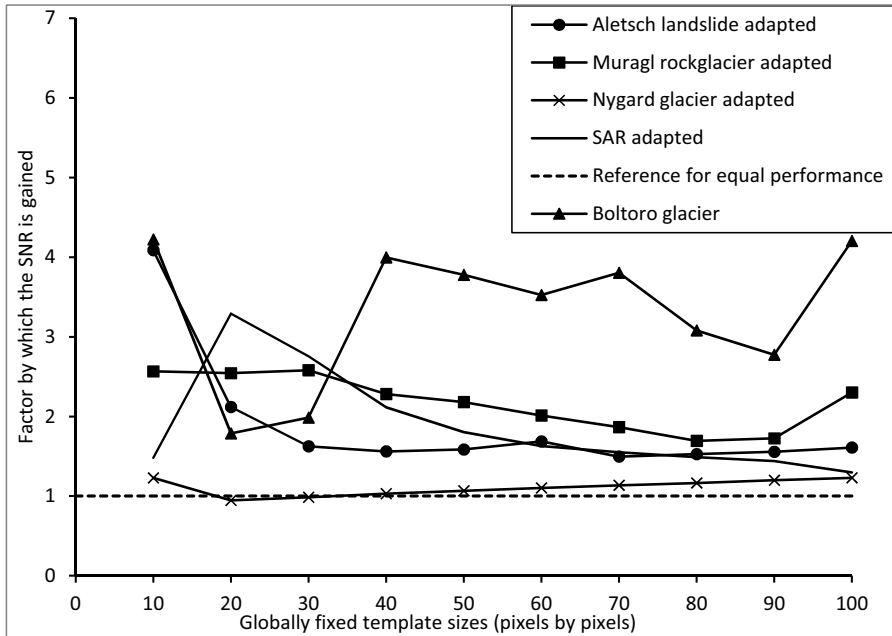


Fig. II-24. The factor by which the SNR of the reconstruction is improved by the locally adaptive algorithm plotted for different image pairs against different globally fixed template sizes

## II.5. General discussion

The above presentations of the results are accompanied by brief discussions. Therefore, a more general discussion is given here.

In area-based image matching, usually regularly spaced templates of square shape with an image-wide (globally) fixed size are used. The general assumptions of this procedure are that: 1) all of the templates are matchable (i.e. they contain enough information for matching); 2) their matches exist in the search image (i.e. they are not occluded). In our approach, the selection of matchable templates based on the optimization of the SNR identified only those templates that fulfill the first assumption and discard those failing to do so. This proved to be very useful in images which contain large sections of monotonous features lacking good signal variance over short distance in cases such as the Baltoro glacier and the inherently noisy images such as the SAR images of Kronebreen glacier.

The use of a non-optimal template size can lead to either or both mismatch and misrepresentation. Mismatch is in the sense that even the central pixel will not get the true

match, whereas, misrepresentation is in the sense that although the central pixel gets its true match, the pixels far away from the central pixel are erroneously represented as they may have been deformed. Optimizing the template sizes through the local maximization of the NCC peaks reduces both error types. Besides, it excludes entities which are completely altered or occluded. In so doing it excludes templates which fail to meet the second assumption stated above.

As the results for both the modeled and the real multi-temporal image pairs show, the locally adaptive algorithm performs better than the globally fixed template size in a range of image types: high spatial resolution optical (aerial), low spatial resolution optical (Landsat), noisy (radar intensity), large temporal base-line, short temporal baseline, etc. It also showed better performance on different Earth surface mass movement types: glacier flow, rockglacier creep and rock sliding. These outcomes show the robustness of the algorithm over different image and process characteristics. The algorithm has a strong advantage over the globally fixed template sizes particularly in cases where the images contain a high level of noise due to either their generic type or due to a large temporal baseline and/or severe deformation. The degree of advantage of using a locally adaptive algorithm depends on image (sensor) type, mass movement type, temporal-baseline, spatial resolution, etc. (Fig. II-24).

The results have shown that in cases where there is very limited or no noise, as in the case of the noise-free test image and the Nigardsbreen glacier aerial image, simply using globally fixed small template sizes may even perform better than the locally adapted algorithm as there is no noise to suppress. Also in cases where there is simple translation-only motion of large features, large template sizes perform well and there might be no need of locally adapting the template sizes. In reality these conditions are rarely encountered for entire mass movements. Repeat images of Earth surface mass movements often contain noises and velocity gradients.

One of the major goals of matching repeat mass movement images is to estimate the horizontal displacement of the masses. The test images showed that locally adapting the template sizes immensely improves the accuracy of the computed displacement. This is also justified by the high reconstruction accuracy as expressed in the correlation between the reference image and the reconstructed search image implying the possible use of the algorithm in other areas such as surface reconstruction, stereoscopy, etc albeit slow computation speed. The reduction in mismatches means less post-matching filtering and reduced heuristic impact of the manual filtering on the reliability. The use of optimized search

windows (which is not covered in this study) could remove most of the few remaining mismatches.

The principles followed in the algorithm discussed here are comprehensive of single principles developed in previous studies. Most popularly, intensity and disparity variations are used to model uncertainty of disparity estimation for different template sizes taking the size which produces the lowest uncertainty as the optimum size (Kanade and Okutomi, 1991; Kanade and Okutomi, 1994; Okutomi and Kanade, 1990; Okutomi and Kanade, 1992). Cyganek (2005) used entropy to look for template sizes with adequate information content. Pan (2008) used reduction of noise variance and maximization of sum of square intensity gradients to define optimum template sizes. Both approaches might be plausible in stereo matching. However, in Earth surface mass movements, as presented in this article, entities recognized to have adequate signal variance (entropy) in the reference image may or may not be retained due to the large temporal baseline and the non-rigid motion of the masses. In the present study, SNR maxima are used to model entity boundaries and to identify entities with good texture. They improve the reliability by discarding unmatchable templates. SNR maxima alone, without the iteration that maximizes the certainty, may not necessarily result in reliable estimate in Earth surface mass movement analysis. Optimization of the NCC peak is thus used.

The algorithm extended the use of the NCC from simply comparing different search templates to comparing concentric templates of different sizes. The study also made use of the normalized cross correlation to quantify the performance of the algorithm itself. Therefore, as the algorithm is much dependent on the NCC, its success and failures are very much related to the success and the failure of the NCC itself.

The algorithm is one step forward towards full automation of deformation measurement in Earth surface mass movements, which is increasingly becoming important due to the increasing need for fast and reliable monitoring system of such processes. The necessity is partly increased by the climate change driven hazardous Earth surface mass movements in high mountains and cold regions, sometimes with disastrous consequences. Besides, human activities are expanding to such areas driven by economic and population growth.

The drawback of the algorithm is that it is computationally expensive as iteration is involved in both the identification of matchable templates and finding their optimum sizes. It is over 10 times slower compared to the globally fixed template sizes depending on the SNR, contrast in the image and the maximum template size set. For example, to match 1912

templates on a computer with 6GB RAM and 3GHZ processor speed, the conventional NCC algorithm took about 62 seconds (ca. 1 minute), where as the locally adaptive algorithm took 551 seconds (ca. 9.2 minutes). The process can take up to hours depending on the computer performance, the search window size and the number of templates to be processed.

## **II.6. Conclusions and outlook**

This paper presented a new algorithm for locally adaptive template sizes in NCC-based image matching for displacement measurement of Earth surface mass movements. First, it investigated the relationship between template size and SNR. The relationship was then used to devise an algorithm that identifies matchable templates. Second, it investigated the relationship between template size and the NCC coefficient. The relationship was then used to iteratively identify the optimum size for each template. The two algorithms were combined step-wise to create a more efficient and more reliable algorithm.

Testing of the algorithm on artificially modeled image displacements and its implementation on real mass movement images show that the algorithm performs better than globally fixed template sizes. It removes the mismatches due to ambiguity in small template sizes and reduces the errors of misrepresentation due to geometric distortion in large template sizes depending on the noise content and deformation of the images. Up to over 90% reduction in mean absolute displacement error and up to over 4 times improvement in SNR of the image matching can be obtained compared to the globally fixed template sizes. Errors due to geometric distortion remain only where noise or lack of good signal variance necessitate the use of large template sizes. The algorithm discards most of the templates which lack sufficient SNR and occluded templates (i.e. templates whose matches do not exist). The algorithm is found to be fairly robust over different Earth surface mass movement types and images of different characteristics and qualities although its performance varies accordingly. It retains its superiority in dense matching as well.

Although the study focused on the NCC alone, it is in principle believed that the findings hold for other area-based image matching methods in the spatial domain. The algorithm pushes displacement measurement from repeat images one step forward towards full automation. One can also use the first part of the algorithm separately if one is interested in only identifying matchable templates.



This study also presented two other important procedures. First, Earth surface mass movements over a certain temporal baseline were computationally modeled. Such modeling approach can be used to evaluate other image processing methods for Earth surface mass movements. Second, a self-relying quantitative performance evaluation of image matching results was presented for cases where reference displacement data is not available, which is often the case. The first image is thereby reconstructed by reversing the measured displacements. Then the correlation coefficient and SNR between the reconstructed and the original first image are computed. The technique proved to be reliable and can be used in comparative evaluation of image matching methods.

There are some issues that need to be resolved through further investigations. First, the computational efficiency of the algorithm needs to be improved. Second, the algorithm needs to be extended to other template shapes as Earth surface features may better be modeled by other shapes than squares. Third, automated ways of defining optimum search window sizes need to be devised to limit the probability of mismatching and reduce computational cost.

## **Acknowledgements**

Special thanks are due to two anonymous referees and the editor of the paper for their careful and constructive comments. This study was supported by the Research Council of Norway (NFR) through the CORRIA project (no. 185906/V30), the International Centre for Geohazards (SFF-ICG 146035/420), and the ESA GlobGlacier and Climate Change Initiative “glaciers and ice caps” project. The Nigardsbreen aerial images are courtesy of EU Glaciorisk, the Landsat data are courtesy of NASA and USGS. The Radarsat data are provided by the Norwegian Space Center/KSAT under the Norwegian-Canadian Radarsat agreement 2009. We would like to express our gratitude to our colleague Torborg Heid for her valuable comments on the manuscript.

## **II.7. References**

- Brown, L.G., 1992. A survey of image registration techniques. *ACM Comput. Surv.*, 24(4): 325-376.
- Debella-Gilo, M. and Kääb, A., 2011. Sub-pixel precision image matching for measuring surface displacements on mass movements using normalized cross-correlation. *Remote Sensing of Environment*, 115(1): 130-142.

- Fusiello, A., Roberto, V. and Trucco, E., 1997. Efficient stereo with multiple windowing. In: Proc. of IEEE Computer Society Conference on Computer Vision and Pattern Recognition. IEEE Computer Society, San Juan, Puerto Rico, 17 - 19 June, 1997, pp. 858-863.
- Gonzalez, R.C. and Woods, R.E., 2008. Digital image processing, third ed. Pearson/Prentice Hall, Upper Saddle River, N.J.
- Haug, T., Käab, A. and Skvarca, P., 2010. Monitoring ice shelf velocities from repeat MODIS and Landsat data - a method study on the Larsen C ice shelf, antarctic Peninsula, and 10 other ice shelves around Antarctica. *The Cryosphere*, 4(1): 161-178.
- Immerkær, J., 1996. Fast Noise Variance Estimation. *Computer Vision and Image Understanding*, 64(2): 300-302.
- Kanade, T. and Okutomi, M., 1991. A Stereo Matching Algorithm with an Adaptive Window - Theory and Experiment. In: Proc. of IEEE International Conference on Robotics and Automation, IEEE Computer Society, Sacramento, California, April, 1991, pp. 1088-1095.
- Kanade, T. and Okutomi, M., 1994. A stereo matching algorithm with an adaptive window: theory and experiment. *IEEE Transactions on Pattern Analysis and Machine Intelligence*, 16(9): 920-932.
- Koo, H.S. and Jeong, C.S., 2001. An area-based stereo matching using adaptive search range and window size. *Lecture Notes in Computer Science*, vol. 2074, pp. 44-53, May, 2001.
- Käab, A., Lefauconnier, B. and Melvold, K., 2005. Flow field of Kronebreen, Svalbard, using repeated Landsat 7 and ASTER data. *Annals of Glaciology*, 42: 7-13.
- Lewis, J.P., 1995. Fast Normalized Cross-Correlation. *Vision Interface*: 120-123.
- Lotti, J.-L. and Giraudon, G., 1994. Correlation algorithm with adaptive window for aerial image in stereo vision, *Image and Signal Processing for Remote Sensing*. SPIE, Rome, Italy, pp. 76-87.
- Nillius, P. and Eklundh, J.-O., 2002. Fast Block Matching with Normalized Cross-Correlation using Walsh Transforms.
- Okutomi, M. and Kanade, T., 1990. A Locally Adaptive Window for Signal Matching. In: Proc. of the International Conference on Computer Vision, December 1990 : 190-199.
- Okutomi, M. and Kanade, T., 1992. A locally adaptive window for signal matching. *International Journal of Computer Vision*, 7(2): 143-162.
- Olsen, L., 2004. A New Proof of Darboux's Theorem *The American Mathematical Monthly* 111(8): 713-715.
- Rank, K., Lendl, M. and Unbehauen, R., 1999. Estimation of image noise variance. In: Proc. of IEE Conference on Vision, Image, and Signal Processing, 146(2): 80-84.
- Schenk, T., 1999. Digital photogrammetry. TerraScience, Laurelville, Ohio.
- Scherer, S., Andexer, W. and Pinz, A., 1998. Robust adaptive window matching by homogeneity constraint and integration of descriptions, In: Proc. of the Fourteenth International Conference on Pattern Recognition, Brisbane, Australia, 16-20 August, 1998, pp. 777-779
- Thong, J.T.L., Sim, K.S. and Phang, J.C.H., 2001. Single-image signal-to-noise ratio estimation. *Scanning*, 23(5): 328-336.
- Veksler, O., 2003. Fast variable window for stereo correspondence using integral images, In: Proc. of IEEE Computer Society Conference on Computer Vision and Pattern Recognition, Madison, Wisconsin, 18-20 June, 2003, pp. 556-561
- Vosselman, G., Sester, M. and Mayer, H., 2004. Basic computer vision techniques. In: J.C. McGlone (Editor), *Manual of photogrammetry*. American Society of Photogrammetry and Remote Sensing, Bethesda, pp. 455-504.

- Wangensteen, B., Gumundsson, Á., Eiken, T., Kääb, A., Farbrot, H. and Etzelmüller, B., 2006. Surface displacements and surface age estimates for creeping slope landforms in Northern and Eastern Iceland using digital photogrammetry. *Geomorphology*, 80(1-2): 59-79.
- Willmott, C.J. and Matsuura, K., 2005. Advantages of the mean absolute error (MAE) over the root mean square error (RMSE) in assessing average model performance. *Climate Research*, 30(1): 79-82.
- Woodcock, C.E. and Strahler, A.H., 1987. The Factor of Scale in Remote Sensing. *Remote Sensing of Environment*, 21(3): 311-332.
- Yihua, X., Dongsheng, W., Tao, F. and Heung-Yeung, S., 2002. Stereo computation using radial adaptive windows, In: *Proc. of the 16th International Conference on Pattern Recognition*, Quebec, Canada, 11.15 August, 2002, pp. 595-598
- Yoon, K.-J. and Kweon, I.S., 2006. Adaptive support-weight approach for correspondence search. *IEEE Transactions on Pattern Analysis and Machine Intelligence*, 28(4): 650-656.
- Zitová, B. and Flusser, J., 2003. Image registration methods: a survey. *Image and Vision Computing*, 21(11): 977-1000.
- Zlobec, S., 2009. Characterizing zero-derivative points. *Journal of Global Optimization*, 46(1): 155-161.



# III. Measurement of surface displacement and deformation on mass movements using least squares matching of repeat images<sup>3</sup>

Misganu DEBELLA-GILO<sup>1</sup> and Andreas KÄÄB<sup>2</sup>

<sup>1,2</sup>Institute of Geosciences, University of Oslo, P. O. Box 1047, Oslo, Norway

<sup>1</sup>[m.d.gilo@geo.uio.no](mailto:m.d.gilo@geo.uio.no) (corresponding author)

**ABSTRACT:** Displacement and deformation are fundamental measures of Earth surface mass movements such as glacier flow, rockglacier creep and rockslides. Ground based monitoring methods can be cost inefficient, time consuming and limited in spatial and temporal data coverage. Remote sensing techniques such as matching of repeat optical images are increasingly used to compute displacement and deformation fields. Strain rates are usually computed in a post-processing step from the velocity gradients. This study explores the potential of automatically computing velocity, rotation and strain rates of Earth surface mass movements simultaneously from the matching positions and from the parameters of the geometric transformation models using the least squares matching (LSM) approach. The procedures are exemplified using bi-temporal high resolution satellite and airborne images of glacier flow, rockglacier creep and land sliding. The results show that LSM matches images and computes longitudinal strain rates, transverse strain rates and shear strain rates reliably with mean absolute deviation in the order of  $10^{-4}$  as evaluated on stable grounds. The LSM also improves the accuracy of displacement estimation of the normalized cross-correlation by over 90% in ideal (simulated) case and by about 25% in real multi-temporal images of mass movements.

**Keywords:** Image matching, Least squares, Mass movement, Displacement, Velocity, Deformation, Strain rate

## III.1. Introduction

Remote sensing is highly suited for slope monitoring in easily inaccessible areas such as high mountains and cold regions where mass movement processes such as glacier flow, permafrost creep and rock sliding are common. Repeat optical image matching is used to compute displacements of slope movements within the temporal baseline of the images' acquisitions [1-5]. The most commonly used group of image matching methods are area-based methods, where intensities of image patches (hereafter referred to as templates), usually of square shape

---

<sup>3</sup> Remote sensing, Revision submitted

and certain size, are matched using a chosen similarity measure. The template within the search image that maximizes similarity or minimizes dissimilarity (depending on the statistic) with the reference template is considered the most likely match [6]. The Euclidean distance between the positions of the reference and the matching templates quantifies displacement, specifically the horizontal displacement component if orthorectified image data are used. The displacement gradient between neighboring templates defines the strain [7,8]. Although there is a range of possible similarity measures [6,9], the normalized cross-correlation (NCC) is the most widely used due to the normalization that makes it insensitive to differences in brightness and contrast [10].

The NCC, and other similarity measures, is subject to a number of shortcomings: (1) The NCC is only reliable in cases where the template is not significantly deformed except shift in position. (2) The precision with which the matching position is located is limited to the pixel size unless some sub-pixel precision procedures [11] are applied. (3) Radiometric differences are not accounted for except normalizing. Thus, the images are matched with a lower precision and accuracy than theoretically possible. In response to these shortcomings least squares matching (LSM) was designed [12]. Instead of assuming exact shape and size of the matching templates, LSM models both geometric and radiometric distortions. The model parameters are determined iteratively using least squares adjustment. The LSM has no limitation of precision as the location of the matches can theoretically be determined at any sub-pixel precision.

Matching of orthorectified and co-registered bi/multi-temporal images of the Earth surface can be thought of as looking to the changing object from a fixed camera multiple times with small (or absent) spatial baselines and dominant temporal baselines. The spatial transformation models are in this case used to model the distortion of the mass, not the perspective one as done in multi-angular parallax matching [13]. The models can thus be used to directly compute intra-template deformation parameters such as normal strain rates, shear strain rates and rotation. The computation of displacement using LSM by itself leads to improved precision of the computed strain even when it is computed later, after the matching, from displacement gradients as is conventional practice. The fact that the LSM is able to model the template's geometric deformation has also the advantage that larger template sizes with higher signal-to-noise ratios (SNR) can be used for the matching as the intra-template deformation, that normally limits the template size, is accounted for.

There is limited application of this powerful image matching approach in mass movement analysis [14-16]. The algorithm has to be tested and evaluated on different types of mass movement and imagery. The possibility of computing deformation parameters directly from the spatial transformation model has to be explored. The study presented here implements the LSM with the affine transformation model on three different types of mass movements and evaluates its performances in displacement measurement compared to that of the NCC. The procedures with which deformation parameters such as longitudinal strain rate, transverse strain rate, shear strain rate and rotation rate are automatically computed during the

matching are implemented and evaluated. The mass movements investigated are glacier flow, rockglacier creep and landslide, at high mountain sites in Europe.

## **III.2. The least squares matching algorithm and its significance in mass movement analysis**

### **III.2.1. The least squares matching algorithm**

The LSM algorithm works based on the L2-norm theorem to determine the best matching position by adjusting the geometry and radiometry of the matching templates so that the sum of squares of the gray-value differences (SSD) between the two templates is minimized [12,17,18]. Assume a discrete two dimensional function  $F(x, y)$  represents intensity data of a subset of an image taken over a certain area at a time  $t_1$ .  $G(x', y')$  represents intensity data of a subset of another image taken over the same area at some other time  $t_2$ . In principle, if the two subsets (templates) match, the two functions will be equal. However, due to the likely presence of noises in both images, random noise ( $e$ ) is added (Equation (III-1)). In an ideal situation  $e$  or its expectation equals zero. In the displacement measurement of Earth surface mass movements, the two images are often taken with long temporal base lines. Consequently, systematic radiometric changes can exist due to various factors such as changes in surface condition, illumination, noise, imaging condition and geometric distortions. It is often assumed that the systematic radiometric differences can be accounted for by gain ( $\lambda$ ) and offset ( $\eta$ ) parameters as in Equation (III-2).

$$F(x, y) = G(x', y') + e \quad \text{(III-1)}$$

$$F(x, y) = G(x', y')\lambda + \eta + e \quad \text{(III-2)}$$

A moving slope mass, here represented by an image template, may also change geometrically. A geometric transformation model, characterized by parameters  $p_1$  to  $p_n$ , relates the pixels of the reference template to those of the search template, for each dimension as shown for the affine model in Equations (III-3) and (III-4). The relationship between the two intensity data will consequently incorporate the parameters of the model (Equation (III-5)). This relationship can be linearized using Taylor-series expansion and rewritten in matrix form as in Equation (III-6). Here,  $v$  is the residual,  $A$  is the differential quotations computed from the gray-value gradients,  $l$  is the difference between the gray-values of the matching templates, and  $dp$  is element of the adjustments ( $dp_1, \dots, dp_n, d\lambda, d\eta$ ) to the initial parameter values which assume the same size, shape and orientation. The solution for  $dp$  is then computed using Equation (III-7). The process is iterated until the computed  $dp$  converges close to zero. LSM is an unbiased minimum variance estimator with the variance

computed as in Equation (III-8) where  $RC$  is the total number of observations (pixels in the template) and  $n$  is the number of model parameters. Further details of the LSM algorithm are given in [17,19,20].

$$x' = p_1 + p_2x + p_3y \quad (III-3)$$

$$y' = p_4 + p_5x + p_6y \quad (III-4)$$

$$e = F(x, y) - G \left( f_x(p_1, p_2, p_3, x, y), f_y(p_4, p_5, p_6, x, y) \right) \lambda + \eta \quad (III-5)$$

$$v = A * dp - l \quad (III-6)$$

$$dp = (A' \pi A)^{-1} A' l \quad (III-7)$$

$$\sigma_0^2 = \frac{v' \pi v}{(RC - n)} \quad (III-8)$$

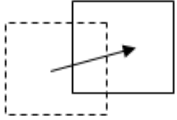
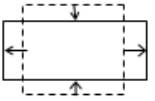
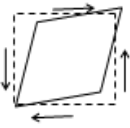
### III.2.2. The least squares matching in mass movement analysis

LSM, as a precise matching algorithm, is expected to produce precise velocity for each pixel of the template. This gives the advantage that velocity gradients, i.e. strain rates, can be computed at sub-template level, even if computed after the matching. Additionally, the spatial transformation parameters ( $p_i$ ) are measures of the geometric deformation of the masses between the acquisition times of the two images. The specific meanings of each of the spatial transformation parameter in mass movements are presented in Table III-1 together with a sketch of the geometric changes represented. The spatial transformation parameters can be exploited to automatically compute strain rates simultaneous with the matching as outlined below.

Figure III-1 reduces the reality of Earth surface mass movements to the square template depicted, which has unit sizes in both dimensions (denoted as  $l_{xo}$  and  $l_{yo}$  respectively). The unit lengths can also be thought of as diameters ( $2r$ ) of a circle as shown in the figure. After deformation, the template moves to a new location, attains new sizes ( $l_{xi}$  and  $l_{yi}$ ) and gets rotated and/or sheared by angles  $\gamma_1$  and  $\gamma_2$  to a new shape. The circle now becomes an ellipse with maximum extension and compression shown orthogonal to each other (dashed axes of the ellipse). The orientation of the ellipse is not necessarily along the movement direction due to shearing and rotation. Notice that the central pixel itself is also deformed and displaced from the center. The Euclidian distance between  $B$  and  $B'$  (parallel to the longitudinal direction) is the horizontal displacement magnitude while  $\omega$  is the angular displacement direction measured clockwise from the north. The change in size can be quantified using extension ratios ( $S_x$  and  $S_y$ ) as in Equations (III-9) and (III-10).  $S_x$  and  $S_y$  are the same as the scaling factors  $p_2$  and  $p_6$  of Table III-1. The corresponding normal strains ( $\epsilon_x$  and  $\epsilon_y$ ) and their relations with the scaling factors are given in Equations (III-11) and (III-12), adapted from [21,22]. Scaling factors greater than 1 (i.e.  $\epsilon_x$  and  $\epsilon_y$  values greater than 0) imply extension, where as scaling factors less than 1 (i.e.  $\epsilon_x$  and  $\epsilon_y$  values less than 0) imply compression.



Table III-1 Parameters of the spatial transformation models related to mass movement processes

Transformation parameters of Equations (III-3) and (III-4)	Deformation type quantified	Visual example	Significance in mass movement
$p_1$ and $p_4$	Translation		Quantifies shift, creep, slip, and slide. Change in position disregarding shape and size.
$p_2$ and $p_6$	Scaling		Measures change in length due to compressive/extending motion. Measures normal strain (elongation).
$p_3$ and $p_5$	Shearing (and/or rotation)		The slippage of orthogonal masses in relation to one another (and/or rigid rotation of the mass). Measures shear strain and/or rotation angle.

The tangent of the shearing angle or the angle in radians (as the angles are often very small) for each direction is the same as the shearing factors ( $p_3$  and  $p_5$ ) of the transformation models. Shear results in both shearing and rotation. Thus shear strain ( $\gamma_{xy}$ ) and rotation angle ( $\phi_{xy}$ ) are derived from the shearing angles as given in Equations (III-13) and (III-14) respectively [23]. Strain is better expressed in terms of strain rate ( $\dot{\epsilon}_i$ ) which is simply strain per unit time (Equation (III-15)). The strain rates in this study are expressed in the time unit that is covered by the dataset in order to avoid extrapolating for time periods not supported by data.

$$S_x = \frac{l_{xi}}{l_{xo}} \quad (III-9)$$

$$S_y = \frac{l_{yi}}{l_{yo}} \quad (III-10)$$

$$\epsilon_x = \frac{l_{xi} - l_{xo}}{l_{xo}} = S_x - 1 \quad (III-11)$$

$$\epsilon_y = \frac{l_{yi} - l_{yo}}{l_{yo}} = S_y - 1 \quad (III-12)$$

$$\gamma_{xy} = \frac{1}{2} (\gamma_1 + \gamma_2) \quad (III-13)$$

$$\phi_{xy} = \frac{1}{2} (\gamma_1 - \gamma_2) \quad (III-14)$$

$$\dot{\epsilon}_i = \frac{\epsilon_i}{t_2 - t_1} \quad (III-15)$$

Horizontal length of the ground surface plane changes when there is compression or extension. As masses such as ice are incompressible, horizontal compression is usually balanced by vertical extension or vice versa [24], making the total sum of the horizontal and vertical strain rates equal to zero. Compressive/extending motion is well discussed for glaciers [23,25,26] and rockglaciers [24,27,28]. In all cases, longitudinal (i.e. along the flow direction) and transverse (i.e. across flow direction) extension and compression are mentioned to lead to such processes as the formation of crevasses, calving and surface micro topography. Shearing may lead to cracking of the masses and eventually collapses. Here, the radiometric parameters are not used further than estimation of the matching position although it can potentially be used in estimation of surface albedo changes.

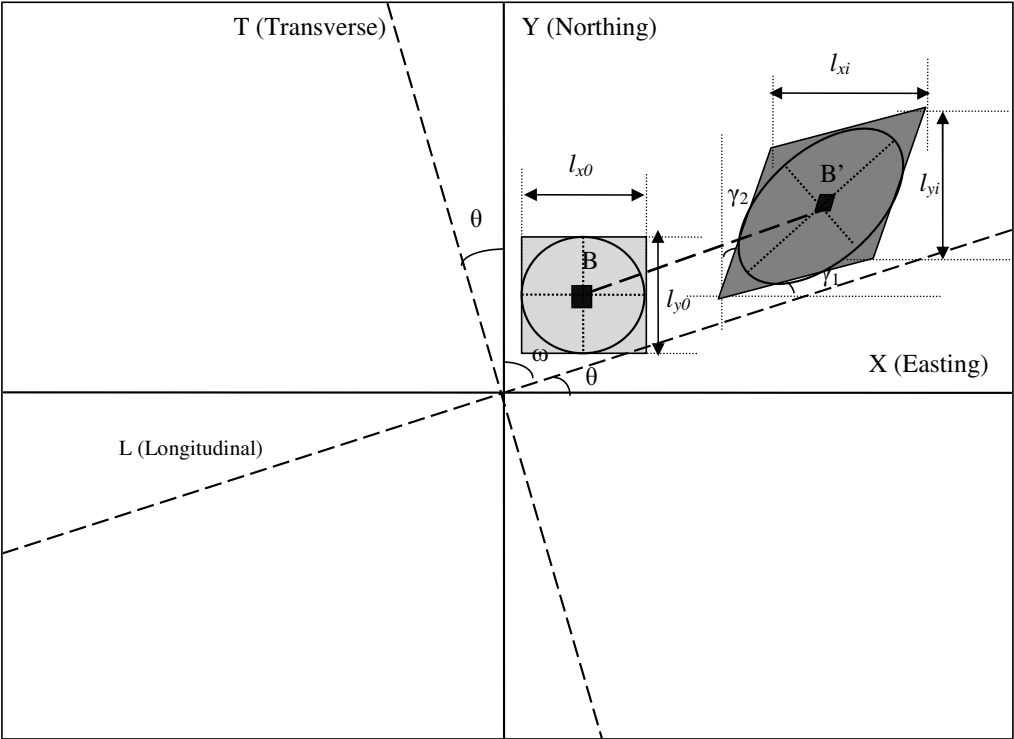


Figure III-1. Deformation of a template and transformation of its parameters from easting-northing to longitudinal-transverse axis.

## III.3. Methods

### III.3.1. Image datasets

In this study, the computations were conducted on three real mass movement image pairs and two pairs of simulated deformed images. The first bi-temporal images (Figure III-2) were taken over a rockglacier in the Muragl valley of the Upper Engadine area in the Swiss Alps (approx. 9.92°E, 46.50°N). The orthoimages used in the present study were based on aerial images taken on 7 September 1981 and 23 August 1994 with 13 years of temporal baseline and 0.2 m of spatial resolution. The Muragl rockglacier has been under investigation for decades using technologies such as photogrammetry, geodesy and geophysics to understand its mechanics [29,30].



Figure III-2. A section of the aerial photographic image (400m x 600m) over part of the Muragl rockglacier taken on 7 September 1981

The second image pair is a section from panchromatic aerial images over the Nigardsbreen glacier in Southern Norway (approx. 61.68°N, 7.20°E). The images were acquired on 19 and 29 August 2001 within the EU Glaciorisk project (Figure III-3). The images were orthorectified using photogrammetric stereo pairs and automatic DEM extraction of the two dates. The ground resolution of the orthoimages is 0.3 m. Surface changes within the very short time period of 10 days were very small, besides glacier flow. Additional details on the images and on their glaciological analysis can be found in [31].

The third bi-temporal images (Figure III-4) are panchromatic images taken by the high spatial resolution QuickBird satellite over the La Clapière landslide (approx. 44.25°N, 6.94°E,) in the French Alps near the town of Saint-Etienne-de-Tinée. The first image was taken on 6 September 2003 with mean in-track view angle of  $-0.5^\circ$  and mean off-nadir view angle of  $9^\circ$ ; whereas, the second image is taken on 27 September 2010 with mean in-track view angle of  $-0.4^\circ$  and mean off-nadir view angle of  $4.2^\circ$ . The ground pixel size of the images is 0.6 m. The images were orthorectified in PCI-Geomatica using the SRTM DEM

and GCPs collected from stable area based on the French 3D web service ([www.geoportail.fr](http://www.geoportail.fr)). As the orthorectification based on this base-map could not result in accurate co-registration, subsequent co-registration using polynomial transformation model was performed using precise GCPs collected from outside the landslide area. Finally, a mean co-registration error of about 1.2 m (2 pixels) is recorded from the horizontal shifts outside the landslide area. The La Clapière landslide has been investigated over the years using different techniques [3,32-34].

A simulated image pair was created by analytically deforming a section of the Nigardsbreen aerial photographic image by using the affine geometric model. Gaussian noise of mean zero and variance ( $\sigma_n^2$ ) 0.01 was added. Another simulated image pair was created by using the same deformation model but adding a higher level of noise,  $\sigma_n^2$  of 0.1. The two simulated deformation image pairs are used for the evaluation of the algorithm as the actual displacements and transformation parameter values are precisely known for these images, in contrast to the real mass movement images.

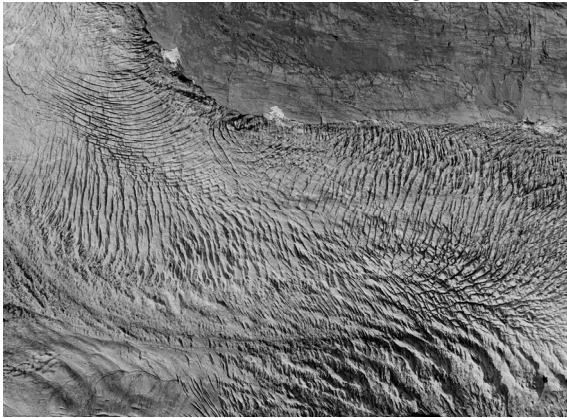


Figure III-3. A section of the aerial photographic image (1233m x 1233m) over part of the Nigardsbreen taken on 19 August 2001



Figure III-4. A section of the QuickBird panchromatic satellite image (1600m x 2430m) over the La Clapière landslide taken on 06 September 2003

### **III.3.2. Image matching**

#### **III.3.2.1. Estimation of initial parameters**

Considering older images as reference and newer images as search images, the images are first matched using the NCC algorithm to estimate the initial parameters for the least squares adjustment. Initially, the matching templates are assumed to have the same geometry (except position). Therefore, for each dimension a unit geometric and radiometric scaling factor is used keeping the other parameters at zero. The least squares iteration starts by using these initial values. Template sizes of 51 by 51 pixels are used for the matching. Smaller template sizes were not used to suppress noises and avoid ambiguity. As LSM is applied in a later step, the presence of displacement gradient in such large templates is not of concern. In fact, as the images are of high resolution, the templates are not large in ground size, i.e. 10.2 m, 15.3 m and 30.6 m for the rockglacier, glacier and landslide images respectively. The search distance is decided based on the expected maximum displacement in each of the image pairs.

#### **III.3.2.2. Least squares iteration**

LSM is implemented using the affine transformation model following the procedures explained in Section III.2.1. The gradients are computed from the matching template, not from the reference template.. Intensity values at sub-pixel positions are interpolated using the cubic convolution [35] as it is the closest to the sinc interpolation, which is the most accurate in image interpolation [36]. The limit for the convergence of the parameters except the translation of the gray-values is set to  $10^{-4}$  for the glacier and the rockglacier but  $10^{-3}$  for the landslide due to the presence of more noise resulting from the vegetation cover and orthoprojection errors. The maximum number of iterations is set to 30 for cases where the parameters do not converge faster. In all cases, when the number of iteration reaches 30 the values of each adjustment should be less than  $10^{-1}$ . After the convergence the cross-correlation coefficient between the two matching templates should be greater than that of the initial. The SSD between the two templates should now be below that of the initial. Otherwise, the template is considered incorrectly converging and excluded from the analysis.

### **III.3.3. Computation of displacement and deformation**

#### **III.3.3.1. Horizontal surface displacement**

After the parameters have converged, the horizontal surface displacement of each pixel is computed separately as Euclidian distance between the pixels' positions in the reference and the matching templates. Velocity is then computed as the displacement divided by the

temporal baseline of the image pair. The movement direction is computed as the arctangent of the ratio of the displacements of the easting and northing directions in angles from the north. For later comparison, the displacements for each mass movement are also registered for the NCC. The mean and standard deviation of the velocities are computed. The standard deviation is computed as the square root of the sum of square differences between individual values and the mean divided by the total number of observations.

### III.3.3.2. Surface strain and rotation rates

The transformation parameters are computed for the X (easting) and Y (northing) directions of the image. However, strains of Earth surface masses make plausible meaning when computed along (longitudinal) and across (transverse) the displacement direction. Therefore, the parameters computed for the easting and northing of the images are transformed to the longitudinal (L) and transverse (T) parameters (Figure III-1). First, however, the coefficients of the spatial transformation models are converted to strain parameters as explained in Section 0. As the parameters are measures of components of the strain tensor, we use strain transformation Equations [21-23]. The strain parameters are thus transformed to the axis along the displacement direction (L), i.e.  $\theta$  degrees from the X-axis, and across the displacement direction (T), i.e.  $\theta$  degrees from the Y-axis.  $\varepsilon_x$ ,  $\varepsilon_y$  and  $\gamma_{xy}$  are then used to compute  $\varepsilon_L$  (longitudinal strain),  $\varepsilon_T$  (transverse strain) and  $\gamma_{TL}$  (shear strain) as in Equations (III-16) to (III-18) respectively. The computations are included in the MATLAB code that is used for the matching to automatically compute the strain rates and rotation angles in addition to the displacement. For the glacier and rockglacier, the negative values of the sums of the longitudinal and transverse strain rates are computed to estimate the vertical strain rate (Equation (III-19)) as both masses are assumed to be incompressible. All of the results are then mapped for visualization and interpretation.

$$\varepsilon_L = \varepsilon_x \cos^2 \theta + \varepsilon_y \sin^2 \theta + \gamma_{xy} \sin \theta \cos \theta \quad (\text{III-16})$$

$$\varepsilon_T = \varepsilon_x \sin^2 \theta + \varepsilon_y \cos^2 \theta - \gamma_{xy} \sin \theta \cos \theta \quad (\text{III-17})$$

$$\gamma_{TL} = -2(\varepsilon_x - \varepsilon_y) \sin \theta \cos \theta + \gamma_{xy} (\cos^{-1} \theta - \sin^{-1} \theta) \quad (\text{III-18})$$

$$\varepsilon_v = -(\varepsilon_L + \varepsilon_T) \quad (\text{III-19})$$

### III.3.4. Performance evaluation

The precision of the LSM algorithm in matching and computation of displacement and strains are evaluated using error propagation principles [17,37]. The precision of the estimated parameters can be expressed by the covariance matrix (Equation (III-20)). However for the precision of the matching, [17] suggests the use of the standard deviation of the shift parameters alone ( $K_{p1}$  and  $K_{p4}$ ) as they determine how precise the matching position is

(Equation (III-21)). Precision measures based on the covariance matrix are however known to be optimistic due to the high data redundancy ([15,17]).

$$K_{xx} = \sigma_0^2 Q_{xx} = \sigma_0^2 (A' \pi A)^{-1} \quad (\text{III-20})$$

$$K_{pi} = \hat{\sigma}_{pi} = \sigma_0 (Q_{pi})^{1/2} \quad (\text{III-21})$$

Accuracy (validity) assessment of the measurements such as displacement and strain rates is conducted on stable grounds and simulated deformation images. The stable grounds are expected to have zero values for the displacement, strain rates and rotation. Simulated deformed images have known displacement and parameter values. The mean absolute deviation (MAD) between the actual and the computed values is used for the evaluation. Stable grounds are not good representation for the mass movements as one source of error, i.e. deformation, does not exist on the stable grounds at least in principle. Thus, to compare the performance of the algorithm over the moving masses to that of the NCC, the SNR of reconstructing the reference image from the search image is computed as detailed in [38], assuming that accurate matching leads to accurate reconstruction. The SNR is computed as the ratio between the correlation coefficient ( $\rho$ ) and one minus  $\rho$ . The relative gain of the SNR is used as a measure of relative performance.

## III.4. Results

### III.4.1. Horizontal surface displacements

The horizontal surface velocity statistics of the three mass movements investigated is presented in Table III-2 to give an overview of the mean, standard deviation (variation of the magnitudes) and the maximum values of the horizontal surface velocities of the mass movements. The velocities of the rockglacier and the landslide are in the range of (tens of) centimeters per year while that of the glacier is in the range of centimeters per day or meters per year ( $\text{ma}^{-1}$ ). In the table, we use velocity units that are relevant for the time period covered by the image pairs. For example, we use  $\text{md}^{-1}$  as opposed to  $\text{ma}^{-1}$  for the velocity of the Nigardsbreen as the data cover only 10 days from late summer. The data on maximum velocity especially that of the landslide, needs to be read with caution. Experience shows that in image matching, ambiguous (noise-based) matches often lead to large displacement estimates. Even when they are filtered manually and systematically, some of such false matches would still remain. Mismatches often occur in fast moving areas where surface destruction is likely. Although such outliers may not have considerable influence on the mean, they may inflate the maximum values.

Table III-2 Overview statistics for horizontal surface velocity for the three mass movements

Mass movement	Muragl rockglacier ( $\text{ma}^{-1}$ )	Nigardsbreen glacier ( $\text{md}^{-1}$ )	La Clapière landslide ( $\text{ma}^{-1}$ )
Mean	0.18	0.57	0.4
Standard deviation	0.09	0.32	0.32
Maximum	0.5	1.1	2.75

The velocity magnitude map of the Muragl rockglacier computed using the LSM is presented in Figure III-5A with the velocity vectors overlaid. The tongue-like shape of the rockglacier also manifests in its velocity distribution creating a similar pattern. The mean velocity of the rockglacier is computed to be  $0.18 \text{ ma}^{-1}$  with the maximum reaching up to  $0.50 \text{ ma}^{-1}$ . There is a high speed area in the middle of the rockglacier that causes considerable velocity gradients. Upstream of this area velocity increases significantly while velocity decreases downstream along the creep direction. The smooth transitions in the velocity field instead of stepwise ones are ascribed to the capability of the LSM to detect and estimate intra-template displacement variation unlike the constant displacement assumed for each template by the NCC-based matching. The open gaps in the figure indicate templates that failed to converge during the LSM iteration. Figure III-5B presents the spatial variation of velocity on the Nigardsbreen glacier computed using the LSM with the velocity vectors overlaid. The glacier velocity is high in the center decreasing towards the boundaries. The velocity vectors show harmonious flow lines with a coherent field of flow directions. The velocity magnitude map of the La Clapière landslide is presented in Figure III-5C together with the velocity vectors. The upper part of the landslide moves faster than the lower. The recently detached part on the upper left part is also moving with high velocity. The reliability of matches in this area is, however, questionable as it is close to the head scarp of the landslide where significant surface changes are likely to lead to mismatching. The velocity vectors show that the major part of the landslide moves towards the south-west with its lower part moving slightly to the south-east direction.



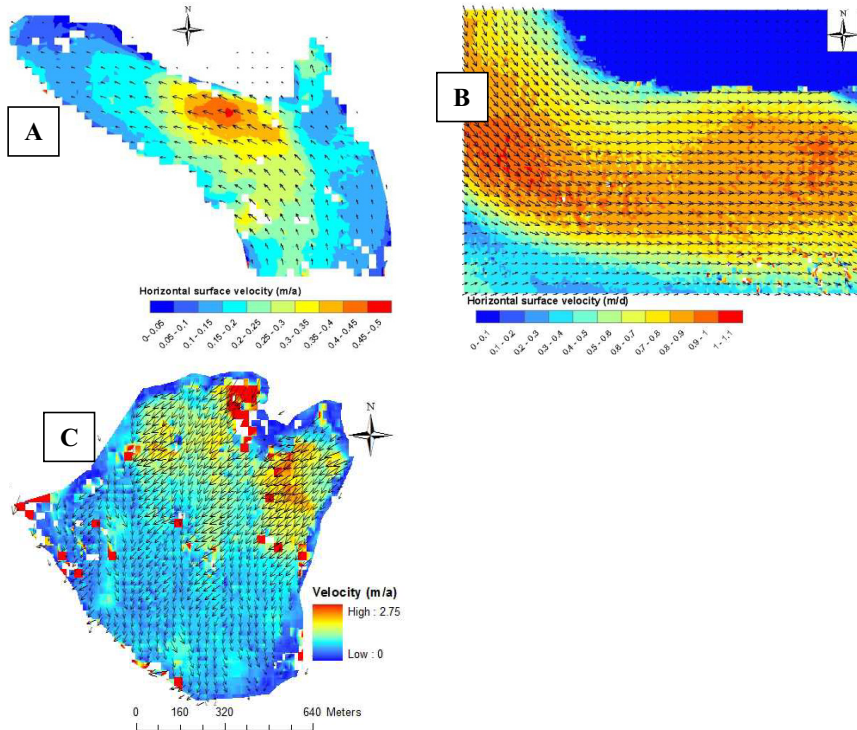


Figure III-5. Velocity ( $\text{ma}^{-1}$ ) maps and vectors of the Muragl rockglacier (A) the Nigardsbreen glacier (B) and the La Clapière landslide (C) computed using the LSM

### III.4.2. Precision and validity of the displacement data

Table III-3 presents the precision of the shift parameters of the three mass movements averaged over all the templates. The highest precision is recorded for the Muragl rockglacier image while the lowest is recorded for the La Clapière landslide. The mean precision ranges between about  $1/20^{\text{th}}$  of a pixel (Muragl) to  $1/6^{\text{th}}$  of a pixel (La Clapière). These show the precisions of the LSM in locating the matching positions under different radiometric and geometric distortions. After observing their histograms, templates with precision of the shift parameters over 0.2 were removed from the analyses. The accuracy (validity) is however dependent on the precision of the orthorectification and co-registration of the images, deformation of the templates, and noise. Stable grounds and simulated deformation images are used to evaluate the validity of the LSM and the NCC algorithms.

Table III-4 presents the mean absolute deviation (MAD) between the measured displacement and the expected displacement for the simulated and the stable grounds of real mass movement images. For the simulated image with low noise variance, about 90% reduction in MAD by the LSM compared to that of the NCC is obtained. However, when  $\sigma_n^2$  is raised to 0.1, the reduction in the MAD by the LSM from that of the NCC is only 52%.

When the noise level ( $\sigma_n^2$ ) increased ten-fold, the error in the estimated displacement increases five-fold for the LSM and only 10% for the NCC. We do not investigate further at this point how far this trend is a general one for LSM applied to noisy images. However, the finding supports the widely known general robustness of NCC algorithm with regard to noise. The reduction in the MAD of displacement error on the stable grounds of the real mass movements is also presented. As the table shows the MAD is the lowest for the glacier (due to precise orthorectification and co-registration of the images) and the highest for the landslide. The percentage of the error (MAD) of the NCC reduced by the use of LSM is the highest in the Muragl rockglacier case followed by the glacier and the landslide respectively.

Table III-3 Mean precision of the shift parameters for the three bi-temporal mass movement image pairs

Image pair	Mean precision of the shift parameters	
	X-shift ( $p_1$ )	Y-shift ( $p_4$ )
Muragl rockglacier creep	0.07	0.06
Nigardsbreen glacier flow	0.11	0.12
La Clapière landslide	0.13	0.15

Table III-4 The MAD of the errors of displacement on the simulated deformation images and the stable grounds of the real mass movement images

Image pair	MAD (in pixels)		Percent reduction by LSM
	NCC	LSM	
Simulated ( $\sigma_n^2=0.01$ )	0.38	0.04	90
Simulated ( $\sigma_n^2=0.1$ )	0.42	0.2	52
Muragl rockglacier creep	2.25	1.4	37
Nigardsbreen glacier flow	0.47	0.34	27
La Clapière landslide	2.5	2.01	19

As stated above, the SNR of reconstructing the reference image of  $t_1$  from the deformed image of  $t_2$  is also computed over the mass movements. For the analytically deformed image pairs, the relative gain in the SNR of the LSM in relation to that of the NCC is close to 100% (double) in the case where the noise standard deviation is 0.01 and 47% where it is 0.1. For the real mass movement images, around 25% gain in SNR of matching is obtained by using the LSM compared to that of the NCC. The LSM algorithm again makes the best improvement on the Muragl rockglacier. The expectation is that this improvement in the SNR of the image reconstruction translates to improvements in the accuracy of the estimated displacements (velocities). For the analytically deformed images, the gain in the SNR is comparable to the reduction in MAD of the estimated velocities. The improvements in the SNR for the real mass movements are also comparable to the reductions in the MAD of the velocities of their stable ground except for the La Clapière landslide. The general trend of agreement between the SNR gain and the reduction in MAD of displacement shows some important points. (1) The LSM performs clearly better than the NCC. (2) The SNR gain of image reconstruction is directly related to the accuracy of the displacement estimation. (3)

Increased noise level reduces the performance of the LSM strongly indicating that the LSM is sensitive to noise, more than NCC is.

### III.4.3. Surface strain and rotation rates

#### III.4.3.1. The Muragl rockglacier

The deformation parameters investigated in this study are the longitudinal strain rate ( $\dot{\epsilon}_L$ ), the transverse strain rate ( $\dot{\epsilon}_T$ ), the shear strain rate ( $\dot{\epsilon}_{LT}$ ) and the rotation rate ( $\phi$ ). The results for the Muragl rockglacier are presented in Figure III-6 and Figure III-7. Summary statistics for the computed deformation parameters are given in Table III-5. The statistics of the  $\dot{\epsilon}_L$  data shows that 96% of the creeping rockglacier has  $\dot{\epsilon}_L$  between  $-0.0034 \text{ a}^{-1}$  and  $0.0037 \text{ a}^{-1}$  with a mean of  $0.00012 \text{ a}^{-1}$ . Regions of extending deformation (the hollow circles of Figure III-6A) are regions where the velocity increased considerably over short distance. Areas of compressive movement (black circles in the figure) are characterized by decreasing speed along the creep direction. One region stands out for its high compression in the longitudinal direction. This region is located immediately downstream of the high velocity region shown in the velocity map (Figure III-5A). The rest of the rockglacier is characterized by steady creep with very limited velocity gradients.

The  $\dot{\epsilon}_T$  map (Figure III-6B) shows that the rockglacier is compressed where velocity decreases across the flow direction and extended where velocity increases across the flow direction obeying a similar rule as  $\dot{\epsilon}_L$ . The figure shows that the rockglacier is mainly extended in the transverse direction. The extension is more pronounced in areas where longitudinal compression is recorded. In contrast to the  $\dot{\epsilon}_L$ , the upper (northern) side of the tongue-like shape of the rockglacier is mainly compressed in transverse direction, while the lower boundaries are mainly extended.

Table III-5 Summary statistics of the computed deformation parameters of the Muragl rockglacier

Deformation parameter	Mean	Standard deviation	Minimum	Maximum
Longitudinal strain rate ( $\text{ma}^{-1}$ )	0.00012	0.0018	-0.0077	0.0085
Transverse strain rate ( $\text{a}^{-1}$ )	0.00039	0.0016	-0.0061	0.0077
Shear strain rate ( $\text{a}^{-1}$ )	0.0015	0.0016	0	0.01
Rotation rate ( $\text{degrees a}^{-1}$ )	0.068	0.066	0	0.44

The horizontal compression and extension are compensated for by the vertical extension and compression respectively as the rockglacier can roughly be assumed to be incompressible due to its ice content. This means the negative sum of the horizontal strain rates presented in Figure III-7 is assumed to be equal to the vertical strain rate. The upstream part of the rockglacier and its margin at the tip of the tongue-like shape are dominated by

vertical compression, which would in practice lead to dynamic thinning of the body. This is indicative of net material drainage from that zone into the lower one. The downstream part of the rockglacier is dominated by vertical extension (hollow circles of the figure) or horizontal compression indicating net influx of material, and expected dynamic thickening. However, erosion of materials, vertical compression, at the tip of the tongue-shaped rockglacier is clearly marked by the dark circles of Figure III-7.

The  $\dot{\epsilon}_{LT}$  of the Muragl rockglacier (Figure III-6C) demonstrates high shear strain rate associated with the boundaries of significant change in velocity (speed or direction) as can be observed from the dark regions of the figure. The significant change in flow direction and speed seems to have created such significant shearing. The mean  $\dot{\epsilon}_{LT}$  is  $0.0015 \text{ a}^{-1}$  which means 1.5 mm of shearing in a 1 m horizontal distance over one year period. However, this can in places reach up to 1cm (Figure III-6C and Table III-5).

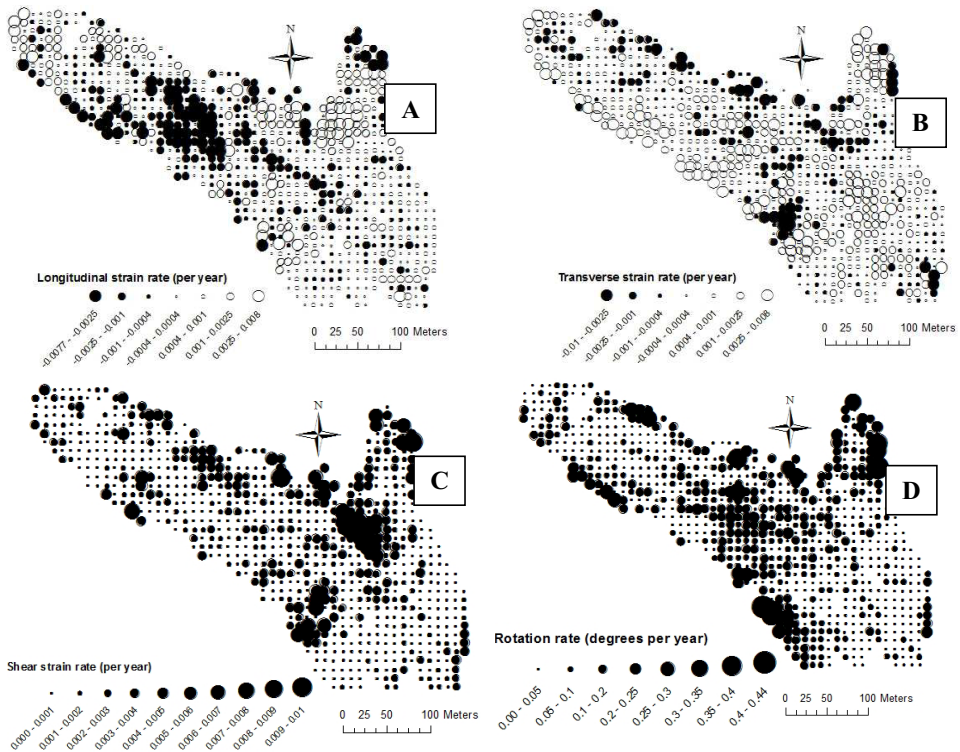


Figure III-6. The  $\dot{\epsilon}_L$  (A),  $\dot{\epsilon}_T$  (B),  $\dot{\epsilon}_{LT}$  (C) and the rotation rate (D) for the Muragl rockglacier

Figure III-6D presents the spatial variation of the rotation rate for the rockglacier. The high rotation areas are the inflection zones where the rockglacier flow direction changes from the northward to the north-westward. The maximum rotation rate registered is  $0.44 \text{ degrees a}^{-1}$  with the mean rotation rate close to  $0.07 \text{ degrees a}^{-1}$ . The strain, shear and rotation values obtained are representative for the size of matching windows used, here  $51 \times 51$  pixels. The

values may change slightly with template size as the spatial transformation parameters are for the whole template.

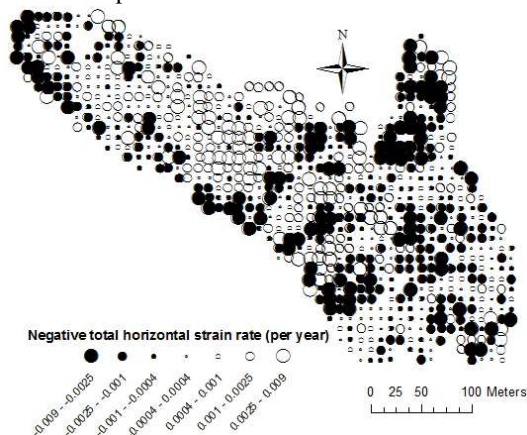


Figure III-7. The negative sum of the horizontal strain rates (assumed to be equal to the vertical strain rate for an incompressible medium) for the Muragl rockglacier.

#### III.4.3.2. The Nigardsbreen glacier

Summary statistics of the computed deformation parameters for the Nigardsbreen glacier (maps not shown here) are given in Table III-6. The statistics here include stable ground which has deformation parameter values close to zero. Recalling that ice is not compressible, the negative of the sum of the longitudinal and the transverse strain rates is computed for the Nigardsbreen and presented in Figure III-8. A major part of the glacier section registered total horizontal compression (vertical extension), i.e. dynamic thickening of the glacier. The stable ground is unstrained and thus has vertical strain rates close to zero. The boundaries with the stable ground are compressed in transverse direction which is not compensated with longitudinal extension. Therefore, it is vertically extended or thickens dynamically; so are all the areas shown in hollow circles. The areas covered by the dark circles are areas where the glacier has shown horizontal extension. As stated above, vertically extended areas indicate mass gain while vertically compressed areas mass loss.

Table III-6 Summary statistics of the computed deformation parameters of the Nigardsbreen glacier section

Deformation parameter	Mean	Standard deviation	Minimum	Maximum
Longitudinal strain rate (d-1)	-0.0003	0.0024	-0.01	0.012
Transverse strain rate (d-1)	-0.00067	0.002	-0.01	0.007
Shear strain rate (d-1)	0.0017	0.002	0	0.019
Rotation rate (degrees d-1)	0.072	0.076	0	0.54

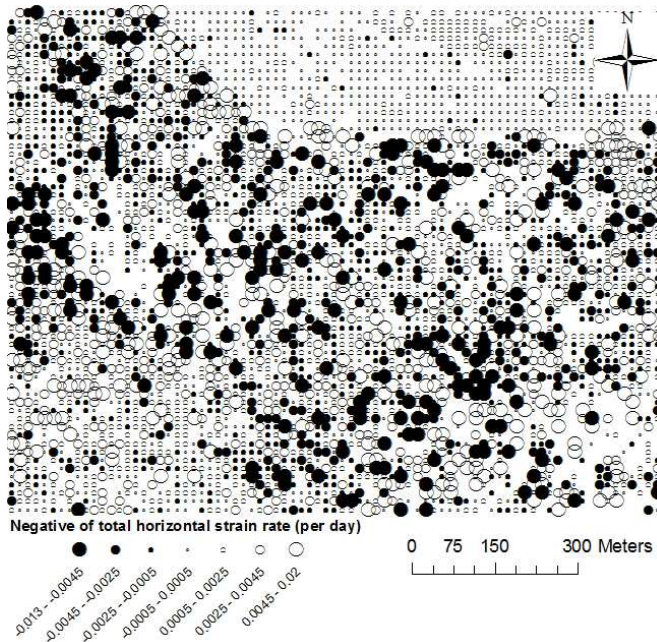


Figure III-8. The negative sum of the horizontal strain rates (assumed to be equal to the vertical strain rate) of the Nigardsbreen glacier.

### III.4.3.3. The La Clapière landslide

The computed  $\dot{\epsilon}_L$ ,  $\dot{\epsilon}_T$ ,  $\dot{\epsilon}_{LT}$ , and rotation rate for the La Clapière landslide are presented in Figure III-9A to D respectively. Summary statistics of the deformation parameters for the landslide are presented in Table III-7. Recall that the maps have poor orthorectification quality and the ground undergoes considerable surface changes in seven years due to the vegetation cover. Therefore, the deformations quantified are not necessarily the ground deformation alone. Nonetheless, longitudinally the landslide is mainly extended with few zones of compression (Figure III-9A). As expected, the lower part of the landslide is longitudinally compressed. There are few interesting regions where significant transverse compression is observed (Figure III-9B). These areas are where the masses converge from two directions leading to compression or net influx of masses. There are three channel-like compression regions as can be observed from the maps of the  $\dot{\epsilon}_T$ . These patterns however do not have corresponding ground structure. The mass is a porous medium that can change density under stress. Therefore, the principle that holds for glacier and roughly for rockglaciers that compression in one dimension leads to extension in the other dimension does not necessarily hold for such porous landslides. Computing the negative sum of the horizontal strain rates does thus not produce a meaningful parameter.

When it comes to the surface shear strain rate (Figure III-9C), it is only the north-west and western part of the landslide that is highly sheared. The northwestern part of the landslide cracked from the stable ground recently and seems to be actively shearing. The same regions show high rotation rate (Figure III-9D). The major part of the landslide seems to be extended both longitudinally and transverse with limited shearing and rotation. Apart from the northern part, the high rotation areas are the foot of the landslide where the materials rotate towards south east after reaching the foot.

Table III-7 Summary statistics of the computed deformation parameters of the La Clapière landslide

Deformation parameter	Mean	Standard deviation	Minimum	Maximum
Longitudinal strain rate ( $a^{-1}$ )	-0.0009	0.005	-0.028	0.017
Transverse strain rate ( $a^{-1}$ )	-0.0007	0.005	-0.01	0.017
Shear strain rate ( $a^{-1}$ )	0.005	0.005	0	0.03
Rotation rate (degrees $a^{-1}$ )	0.15	0.13	0	0.7

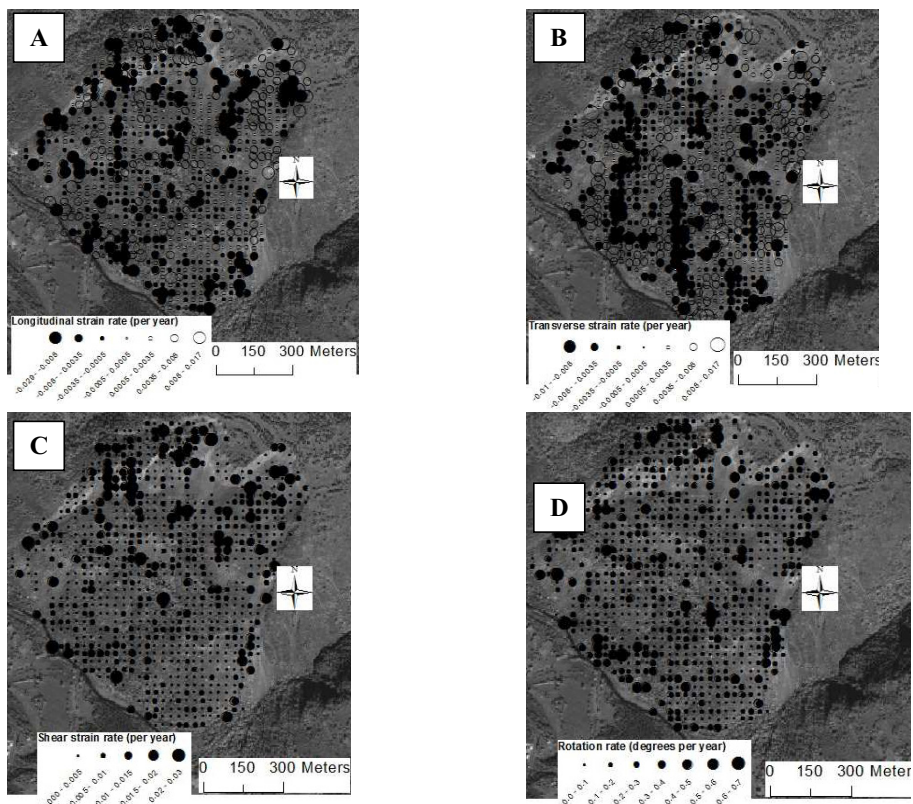


Figure III-9. The  $\dot{\epsilon}_L$  (A),  $\dot{\epsilon}_T$  (B),  $\dot{\epsilon}_{LT}$  (C) and the rotation rate (D) of the La Clapière landslide

### III.4.4. Precision and validity of the deformation data

Error propagation using the covariance matrix of the geometric parameters of the affine transformation model ( $Kp_i$ ) shows high precision in the order of  $10^{-3}$  (Table III-8). The parameters are related directly to the strains as shown in the bracket. The mean absolute value of the estimated parameters is given in the parenthesis for overview of the relative magnitude of the precisions. The uncertainty is therefore less than 10% of the estimated parameter values, i.e. at least one decimal point lower. The scaling parameters are relatively more precise than the shearing parameters.

The MAD of the strain rates on the stable grounds are in the order of  $10^{-4}$  for the glacier and rock glacier and  $10^{-3}$  for the landslide (Table III-9). This means the values estimated for each deformation parameter in reality lies within the estimated value  $\pm$  the MAD. The error values for rotation are somewhat higher in all cases. This might be an indication of a slight rotation of one of the images against the other. The error magnitudes are however below (at least 1 level of significance) the estimated values of the deformation (rotation and strain rates) except that of the La Clapière landslide for which the computed strain rates are not significantly outside the error margin. These MAD values can be optimistic as they are computed on non-deformed area, i.e. stable ground.

Table III-8. Precision of the geometric (shape and size) parameters of the spatial transformation model for the three mass movement types

Mass movement type	Precision of the parameters			
	$Kp_2$ ( $p_2=1+\epsilon_x$ )	$Kp_3$ ( $P_3=\gamma_1$ )	$Kp_5$ ( $P_5=\gamma_2$ )	$Kp_6$ ( $P_6=1+\epsilon_y$ )
Muragl rockglacier creep	0.002 (0.997)	0.002 (0.021)	0.002 (0.022)	0.002 (0.998)
Nigardsbreen glacier flow	0.003 (0.997)	0.003 (0.013)	0.003 (0.021)	0.003 (0.999)
La Clapière landslide	0.003 (1.001)	0.003 (0.038)	0.003 (0.044)	0.003 (0.098)

Table III-9. The standard deviation of the errors of the computed rotation and strain rates as computed on the stable grounds of the mass movement images

Deformation parameters	MAD		
	Nigardsbreen glacier ( $d^{-1}$ )	Muragl rockglacier ( $a^{-1}$ )	La Clapière landslide ( $a^{-1}$ )
$\dot{\epsilon}_L$	0.0001	0.0005	0.006
$\dot{\epsilon}_T$	0.0001	0.0006	0.002
$\dot{\epsilon}_{LT}$	0.0002	0.001	0.005
$\phi_{TL}$	0.008	0.05	0.1



## III.5. Discussion

### III.5.1. Computed displacements and deformations

Although no formal quantitative comparison is conducted, the velocities obtained for the mass movements using the LSM are in agreement with those obtained in other studies using similar and other methods. For example, similar velocities are registered for the same section of the Nigardsbreen glacier during the same period [31]. The average and maximum velocities of the Muragl rockglacier are similar to what is reported in [29] which is validated using different approaches, including ground measurements. The surface velocity data in that study ([29]) agrees well with that of borehole data [39]. The limited surface change during the 13 years period contributes to the success of optical image matching on this rockglacier, and rockglaciers in general. The spatial pattern of the La Clapière landslide velocity variation is in agreement with that computed by other studies, particularly [3]. The velocity magnitudes show a slight slowdown from earlier records (e.g. [32,40]). The decreased magnitudes are in agreement with the general observation of the slowdown of the landslide since the year 2000 (<http://gravitaire.oca.eu/spip.php?rubrique15>). Errors in the orthorectification and the presence of vegetation on the surface leading to radiometric noises imply the presence of blunders in the image matching.

Realistic values of longitudinal, transverse and shear strain rates together with rotation rate are also obtained. The technique computes strain rates at higher resolution than the conventional technique of computing from velocity gradient after the matching. When computing strain rates of a template from the velocity gradients, two neighboring templates are used for each orthogonal dimension. Therefore, the computed negative total sum of strain rate is in a way averaged over neighboring templates. Additionally, such strain rates are simply measures of velocity changes between the central pixels of the neighboring templates especially when the NCC is used for the matching. Thus it can appear smoothed even before filtering. Changes in the size and shape of the masses are not directly computed as is done when using the LSM algorithm.

The spatial patterns of the strain rates and elevation changes of the Muragl rockglacier, previously computed from velocity gradients by [7], agree with those of the present study. The negative total of the horizontal strain rates of the present study (Figure III-7) agrees with figure 3 of [7]. Notice that the symbols in the present study and that study ([7]) are inverse of each other and scaled differently. Areas of vertical compression (horizontal extension) in the present study correspond with negative elevation changes (figure 2 of [7]) indicating loss of mass from those areas. For the Nigardsbreen glacier, the negative sum of the horizontal strain rates shows that the glacier is dominantly extended vertically, which is in agreement with the thickening of the glacier as reported in [31]. High shear strain rate is registered at the margins of flow, especially where the moving glacier borders with stable ground. The deformation

maps of the La Clapière landslide require cautious interpretation as more sources of error can influence the reliability compared to the other two mass movement types as discussed in the following section. Specifically propagated orthorectification error and surface changes such as vegetation cover contribute to major blunders in the strain rate data. Computation of strain rates on its stable ground shows that the computed strain rates are not outside the error margin.

### **III.5.2. On the precision of the algorithm and sources of error**

The results of the study show that the LSM computes horizontal displacements in Earth surface mass movements with significantly higher precision (level of detail of measurement) and accuracy (truthiness of the estimated values) compared to the NCC. The mean precision of the LSM algorithm in locating the matching position is found to be better than 1/6th of a pixel; whereas, the matching precision of NCC is generally +0.5 pixel. In addition to the precision of matching, the accuracy of the computed displacements is also higher when computed using LSM than using NCC as evaluated on test images and stable grounds of the bi-temporal mass movement images. The better performance of the LSM is in agreement with theoretical claims and earlier findings in photogrammetry on image pairs of shorter temporal baselines [19,20,41].

When computing deformation and displacement of mass movements from repeat images using a precise algorithm such as LSM, the sources of error are basically related to either the image (noise, orthorectification and co-registration) or the ground itself (deformation and temporal surface changes). Both major error sources can technically be grouped into three, i.e. geometric errors, radiometric errors and propagated sensor or processing errors. The possible sources that cause geometric error are: (1) the formation of crevasses or micro-topography, (2) the boundary effect where the velocity gradient between the moving body and the stable ground is so large that it creates outlying deformation parameter values. (3) Vegetation cover can also create geometric change that is not actually ground deformation in addition to its contribution to intensity noise. Signal- (in fact the SNR-) related causes include the presence of shadows, surface changes, illumination differences, presence of dirt, vegetation cover, etc that can lead to false and outlying convergence parameter values in the least squares iteration. Propagated errors can be attributed to the sensor or image preprocessing, such as orthorectification and co-registration. If the images are not perfectly orthorectified and co-registered, the geometric adjustment includes the mass deformation, sensor projective distortion and change of geometry between the two images.

Due to the high resolution of strain computation, the maps of the strain rates look noisy when visually observed, necessitating the application of noise filters. In the case of the strain rate maps, it might well be that high-resolution deformations actually are somewhat noisy due to real local deformation of the masses or due to the error sources mentioned above. Filtering would lead to smoothing the whole result. In so doing it affects both the realistic

values and the blunders. The use of larger template sizes also leads to more smoothed strain rate map. Recall that the criteria for the right template size in the NCC is the presence of adequate SNR and constant displacement within the template. In the LSM, one of the criteria is no more constant displacement but rather constant displacement gradient, at least for the affine model. Thus for very large templates, as the parameters of the transformation model are forced to be constant within the template, the computed strain rates visually look like as if they are filtered. Such smoothed or filtered strain rate map may be sufficient or even wanted for some geoscientific applications. However, the detailed variability may be needed for other current and future applications, and provide new insights in to the mechanics of mass movements.

A better approach than filtering or the use of much larger template sizes would therefore be restricting the least squares iteration process more. Pixel-based constraining such as data snooping or template-based constraining such as raising convergence precision can be used [17,20]. This would affect only the highly noisy (and maybe the highly deformed) templates leaving the well-converging templates unaffected. Simple test on the Muragl rockglacier shows that increasing the demanded precision of the parameter adjustment during the LSM iteration discarded more templates especially in the shadow areas resulting in more data-void areas. However, the strong spatial variability is not smoothed implying that they are real strain rate variation.

## **III.6. Conclusions and outlook**

This study explored the possibility of automatically and precisely computing displacement, strain rates and rotation of Earth surface mass movements from repeat optical images simultaneously. The performance of least squares matching (LSM) with an affine geometric transformation model is evaluated in relation to that of the most widely used algorithm for such purposes, i.e. the normalized cross-correlation (NCC). Aerial and satellite images over glacier flow, rockglacier creep and land sliding are used in the study covering three different types of mass movements and two different types of imaging systems.

The results of the study clarified that the LSM estimates the displacement of Earth surface masses with better precision and accuracy than the conventional NCC. Around 25% improvement in the SNR gain of image matching over that of the NCC is registered in real images reaching up to double in the case of the analytically deformed images. The improvements in the SNR gain lead to comparable improvements in the accuracy of the estimated displacement. Up to 35% reduction in the MAD of displacement by the LSM from that of the NCC is observed on the stable grounds of the mass movement images reaching up to 90% in the case of the simulated deformation. The exact magnitude obviously varies depending on the case of application. The improvements are dependent on the level of noise in the image.

The study has also demonstrated the capability of the LSM in deriving surface strain rates and rotation rate simultaneously with the image matching process. This has the potential of replacing earlier approaches based on post-processing from displacement gradients. Additionally, the spatial density of deformation parameters measured and, thus, the unprecedented level of detail of deformation fields obtained might allow for new insights in to the mechanics of the masses observed. The strain rate data obtained through such processes are found to be realistic when compared with data from different sources and when logically evaluated. The spatial transformation parameters from which the strain rates are derived are computed with precision less than 10% of the measured values in all cases. However, evaluation of the accuracy (validity) of the rotation and strain rates on the stable grounds of the mass movement images shows that the accuracy is dependent on the mass movement type, i.e. image and ground characteristics. The MAD is as low as  $10^{-4}$  for the rockglacier and the glacier (one decimal point below the computed average strain rates). For the landslide, the computed strain rates are not outside the error margin.

The capability of deriving surface strains from images through the LSM algorithm advances the application of image matching in mass movement analysis. Once strain is reliably computed from repeat images automatically through image matching, the stress exerted on the masses can also be computed using the stress-strain relationship for the specific type of mass under investigation. This is very important in early warning of geohazards and in understanding terrain kinematics, and hopefully dynamics, in high mountain areas. Validation of the computed strain under different conditions and possibility of extending to the computation of stress requires further research, though.

The algorithm is computationally expensive as it involves iteration for each template. The ever improving computer processor speeds coupled with smarter computational approaches can deal with this limitation. Simple tests indicate that the algorithm is very sensitive to noises in the images. More work is thus needed to define the sensitivity and applicability range of the LSM approach for repeat images of lower resolution, of more strongly deforming masses, and with longer temporal baselines.

## **Acknowledgments**

The orthoimages of the Muragl rockglacier are based on aerial photos acquired by the Swisstopo/flight service (BA057212, BA081844). The Nigardsbreen aerial images are courtesy of EU Glaciorisk. This study is funded by the Research Council of Norway (NFR) through the CORRIA project (no. 185906/V30) and contributes to the NFR International Centre for Geohazards (SFF-ICG 146035/420), the ESA Glaciers\_CCI project, and the Nordic excellence center SVALI. The QuickBird images are courtesy of DigitalGlobe. We would like to thank Dr. Kimberly Casey for proofreading the manuscript.

### III.7. References

1. Kääb, A.; Haerberli, W.; Gudmundsson, G.H., Analysing the creep of mountain permafrost using high precision aerial photogrammetry: 25 years of monitoring Gruben rock glacier, Swiss Alps. *Permafrost and Periglacial Processes* 1997, 8, 409-426.
2. Bindenschadler, R.A.; Scambos, T.A., Satellite-image-derived velocity field of an Antarctic ice stream. *Science* 1991, 252, 242-246.
3. Delacourt, C.; Allemand, P.; Casson, B.; Vadon, H., Velocity field of the "La Clapière" landslide measured by the correlation of aerial and Quickbird satellite images. *Geophys. Res. Lett.* 2004, 31, 15-19.
4. Rolstad, C.; Amlien, J.; Ove Hagen, J.; Lundén, B., Visible and near-infrared digital images for determination of ice velocities and surface elevation during a surge on Osbornebreen, a tidewater glacier in Svalbard. *Annals of Glaciology* 1996, 24, 255-261.
5. Berthier, E.; Vadon, H.; Baratoux, D.; Arnaud, Y.; Vincent, C.; Feigl, K.L.; Remy, F.; Legresy, B., Surface motion of mountain glaciers derived from satellite optical imagery. *Remote Sensing of Environment* 2005, 95, 14-28.
6. Zitová, B.; Flusser, J., Image registration methods: A survey. *Image and Vision Computing* 2003, 21, 977-1000.
7. Kääb, A.; Kaufmann, V.; Ladstadter, R.; Eiken, T., Rock glacier dynamics: Implications from high-resolution measurements of surface velocity fields. *Permafrost*, Vols 1 and 2 2003, 501-506.
8. Kääb, A., Remote sensing of mountain glaciers and permafrost creep. *Geographisches Institut der Universität Zürich: Zürich*, 2005; p 264.
9. Brown, L.G., A survey of image registration techniques. *ACM Comput. Surv.* 1992, 24, 325-376.
10. Lewis, J.P., Fast normalized cross-correlation. *Vision Interface* 1995, 120-123.
11. DeBella-Gilo, M.; Kääb, A., Sub-pixel precision image matching for measuring surface displacements on mass movements using normalized cross-correlation. *Remote Sensing of Environment* 2011, 115, 130-142.
12. Förstner, W. In *On the geometric precision of digital image correlation*, Proceedings of the ISPRS Symposium on Mathematical Models, Accuracy Aspects and Quality Control, Finland, 1982; International Archives of Photogrammetry: Finland, 1982; pp 176-189.
13. Schenk, T., *Digital photogrammetry*. TerraScience: Laurelville, Ohio, 1999; p 428.
14. Whillans, I.M.; Tseng, Y.H., Automatic tracking of crevasses on satellite images. *Cold Regions Science and Technology* 1995, 23, 201-214.
15. Maas, H.G.; Casassa, G.; Schneider, D.; Schwalbe, E.; Wendt, A., Photogrammetric determination of spatio-temporal velocity fields at glacier San Rafael in the northern Patagonian icefield. *The Cryosphere Discuss.* 2010, 4, 2415-2432.

16. Kaufmann, V.; Ladstädter, R. Quantitative analysis of rock glacier creep by means of digital photogrammetry using multi-temporal aerial photographs: Two case studies in the Austrian Alps, Eighth international conference on permafrost, Zurich, Switzerland, 2003. In: Phillips, M.; Springman, S.M.; Arenson, L.U., Eds. Taylor & Francis Zurich, Switzerland, 2003; pp 525-530.
17. Gruen, A., Least squares matching: A fundamental measurement algorithm. Close range photogrammetry and machine vision. In: Atkinson, K.B., Ed. Whittles Publ.: Caithness, Scotland, 1996; pp 217–255.
18. Bethmann, F.; Luhmann, T. Least-squares matching with advanced geometric transformation models, Remote Sensing and Spatial Information Sciences Symposium, Newcastle upon Tyne, UK, 2010; In: International Archives of Photogrammetry, Commission V, WG V/4: Newcastle upon Tyne, UK, 2010; pp 86-91.
19. Gruen, A.W.; Baltsavias, E.P., High-precision image matching for digital terrain model generation. *Photogrammetria* 1987, 42, 97-112.
20. Rosenholm, D., Least squares matching method: Some experimental results. *The Photogrammetric Record* 1987, 12, 493-512.
21. Young, W.C.; Budynas, R.G.; Roark, R.J., *Formulas for stress and strain*. McGraw-Hill: New York, 2002; p 852.
22. Middleton, G.V.; Wilcock, P.R., *Mechanics in the Earth and environmental sciences*. Cambridge University Press: Cambridge, 1994; p 459.
23. Hooke, R.L., *Principles of glacier mechanics*. Cambridge University Press: Cambridge, 2005; p 429
24. Haeberli, W.; Hallet, B.; Arenson, L.; Elconin, R.; Humlun, O.; Kääh, A.; Kaufmann, V.; Ladanyi, B.; Matsuoka, N.; Springman, S., Vonder Muhll, D., Permafrost creep and rock glacier dynamics. *Permafrost and Periglacial Processes* 2006, 17, 189-214.
25. Nye, J.F., The mechanics of glacier flow. *Journal of Glaciology* 1952, 2.
26. Nye, J.F., A method of determining the strain-rate tensor at the surface of a glacier. *Journal of Glaciology* 1959, 3, 409.
27. Kääh, A.; Reichmuth, T., Advance mechanisms of rock glaciers. *Permafrost and Periglacial Processes* 2005, 16, 187-193.
28. Kneisel, C.; Kääh, A., Mountain permafrost dynamics within a recently exposed glacier forefield inferred by a combined geomorphological, geophysical and photogrammetrical approach. *Earth Surface Processes and Landforms* 2007, 32, 1797-1810.
29. Kääh, A.; Vollmer, M., Surface geometry, thickness changes and flow fields on creeping mountain permafrost: Automatic extraction by digital image analysis. *Permafrost and Periglacial Processes* 2000, 11, 315-326.
30. Kääh, A., Monitoring high-mountain terrain deformation from repeated air- and spaceborne optical data: Examples using digital aerial imagery and aster data. *ISPRS Journal of Photogrammetry and Remote Sensing* 2002, 57, 39-52.

31. Wangenstein, B.; Tønsberg, O.M.; Kääh, A.; Eiken, T.; Hagen, J.O., Surface elevation change and high resolution surface velocities for advancing outlets of Jostedalsbreen. *Geografiska Annaler: Series A, Physical Geography* 2006, 88, 55-74.
32. Casson, B.; Delacourt, C.; Baratoux, D.; Allemand, P., Seventeen years of the "La Clapière" landslide evolution analysed from ortho-rectified aerial photographs. *Engineering Geology* 2003, 68, 123-139.
33. Lebourg, T.; Binet, S.; Tric, E.; Jomard, H.; El Bedoui, S., Geophysical survey to estimate the 3D sliding surface and the 4D evolution of the water pressure on part of a deep seated landslide. *Terra Nova* 2005, 17, 399-406.
34. Chemenda, A.I.; Bois, T.; Bouissou, S.; Tric, E., Numerical modelling of the gravity-induced destabilization of a slope: The example of the La Clapière landslide, Southern France. *Geomorphology* 2009, 109, 86-93.
35. Keys, R.G., Cubic convolution interpolation for digital image processing. *IEEE Transactions on Acoustics, Speech and Signal Processing* 1981, 29, 1153-1160.
36. Dodgson, N.A. *Image resampling*; University of Cambridge Computer Laboratory: London, 1992; p 264.
37. Förstner, W., Reliability analysis of parameter estimation in linear models with applications to mensuration problems in computer vision. *Computer Vision, Graphics, and Image Processing* 1987, 40, 273-310.
38. Debella-Gilo, M.; Kääh, A., Locally adaptive template sizes for matching repeat images of earth surface mass movements. *ISPRS Journal of Photogrammetry and Remote Sensing* 2011, accepted.
39. Arenson, L.; Hoelzle, M.; Springman, S., Borehole deformation measurements and internal structure of some rock glaciers in Switzerland. *Permafrost and Periglacial Processes* 2002, 13, 117-135.
40. Guglielmi, Y.; Cappa, F.; Binet, S., Coupling between hydrogeology and deformation of mountainous rock slopes: Insights from La Clapière area (Southern Alps, France). *Comptes Rendus Geosciences* 2005, 337, 1154-1163.
41. Ackermann, F., Digital image correlation: Performance and potential application in photogrammetry. *The Photogrammetric Record* 1984, 11, 429-439.





# Appendix

## Publications of M. Debella-Gilo

### Peer-reviewed journal articles

Debella-Gilo, M. and A. Kääb (2011). "Sub-pixel precision image matching for measuring surface displacements on mass movements using normalized cross-correlation." Remote Sensing of Environment **115**(1): 130-142.

Debella-Gilo, M. and A. Kääb (2011). "Locally adaptive template sizes for matching repeat images of Earth surface mass movements." ISPRS Journal of Photogrammetry and Remote Sensing. *Revision submitted*.

Debella-Gilo, M. and A. Kääb (2011). "Surface displacement and deformation on mass movements using least squares matching of repeat images." Remote sensing *Revision submitted*.

Bryn, A. and M. Debella-Gilo (2011). "GIS-based Prognosis of Potential Forest Regeneration Affecting Tourism Locations and Cultural Landscapes in South Norway." Scandinavian Journal of Hospitality and Tourism **11**(2): 166-189.

Debella-Gilo, M. and B. Etzelmüller (2009). "Spatial prediction of soil classes using digital terrain analysis and multinomial logistic regression modeling integrated in GIS: Examples from Vestfold County, Norway." CATENA **77**(1): 8-18.

### Peer-reviewed proceedings papers

Debella-Gilo, M. and A. Kääb (2011). Monitoring slow-moving landslides using spatially adaptive least squares image matching. The Second World Landslide Forum. Rome, Italy, *Accepted*.

## Extended abstracts

- Haug, T., M. Debella-Gilo, J. Karstensen and A. Kääb(2010). Performance and application of different image matching algorithms for investigating glacier and ice-shelf flow, permafrost creep and landslides. Geosciences and Remote Sensing Symposium (IGARSS), 2010 IEEE International.
- Debella-Gilo, M. and A. Kääb (2010). Sub-pixel precision image matching for displacement measurement of mass movements using normalized cross-correlation. *International Archives of Photogrammetry, Remote Sensing and Spatial Information Sciences* 2010; Volume XXXVIII. Suppl. 7B s. 181-186
- Debella-Gilo, M. and A. Kääb (2011). Locally adaptive template sizes for matching repeat images of Earth surface mass movements. Geosciences and Remote Sensing Symposium (IGARSS), 2011 IEEE International.
- Debella-Gilo, M., B. Eitzelmüller and O. Klakegg (2007). Digital Soil Mapping Using Digital Terrain Analysis and Statistical Modeling Integrated into GIS: Examples from Vestfold County of Norway. 11th Scandinavian Research Conference on Geographical Information Science, Ås, Norway, Department of Mathematical Sciences and Technology, UMB.
- Debella-Gilo, M. and A. Kääb (2010). "Sub-pixel precision algorithms for normalized cross-correlation based image matching of mass movements." Geophysical Research Abstracts **12**(EGU2010-520-1).

## Poster presentations

- Debella-Gilo, M. and A. Kääb (2011). "Spatially adaptive least squares image matching for monitoring slow-moving landslides." Geophysical Research Abstracts **13**(EGU2011-6261-1,).
- Debella-Gilo, M. and A. Kääb (2010). Sub-pixel Precision Image Matching for Displacement Measurement of Mass Movements Using Normalized Cross-Correlation. ESA Summer School on Earth Systems Modeling and Monitoring; 2010-08-01 - 2010-08-13